ABSTRACT

Experimental and Numerical Study on Flow Control Using Obliquely Aligned Elements

Gilberto Narvaez III, M.S.

Mentor: Stephen T. McClain, Ph.D.

The use of micro-electromechanical system devices (MEMS) have been studied extensively in literature for control of flow separation and transitioning to turbulent flow. However, there is limited information about how obliquely aligned roughness elements affect the boundary layer development and induce turbulence. The purpose of this study was to measure the transverse flow and turbulent intensities produced by an array of 0°, 5°, 10°, and 15° obliquely-aligned elliptical control elements in turbulent flow at 2, 5, and 10 m/s on a flat plate. The resulting boundary-layer measurements demonstrate the ability of the control elements to produce tailored secondary flows. Since the test coupon was of finite span, results demonstrate that controlled vortices can also be generated using the arrays. Additionally, CFD simulations were performed and compared to the experimental results using the realizable k-ε turbulence model in ANSYS FLUENT 12.0 with solutions converging to residuals less than $1\text{x}10^{-6}$ for flow and turbulence quantities.

Experimental and Numerical Study on Flow Control
Using Obliquely Aligned Elements

by

Gilberto Narvaez III, B.S.

A Thesis

Approved by the Department of Mechanical Engineering

William Jordan, Ph.D., Chairperson

Submitted to the Graduate Faculty of
Baylor University in Partial Fulfillment of the
Requirements for the Degree
of
Master of Science

Approved by the Thesis Committee

Stephen T. McClain, Ph.D., Chairperson

Kenneth W. Van Treuren, Ph.D.

John M. Davis, Ph.D.

Accepted by the Graduate School
May 2010

J. Larry Lyon, Ph.D., Dean

Page bearing signatures is kept on file in the Graduate School.

TABLE OF CONTENTS

LIST OF FIGURES

LIST OF TABLES

LIST OF ABBREVIATIONS

h	heat transfer coefficient
k	yaw coefficient
s	span of test coupon = 20.32 cm
u	velocity in the direction in the primary flow
v	velocity in the direction normal to the flat plate
w	velocity in the direction transverse to the primary flow
x	axis in the direction in the primary flow
x_c	ratio of location on the plate to the plate length
y	axis in the direction normal to the flat plate
z	axis in the direction transverse to the primary flow
A/D	analog-digital conversion
AOA	angle of attack
CFD	computational fluid dynamics
CTA	constant temperature anemometry
D_f	skin friction drag
D_i	induced drag
DAQ	data acquisition
E	voltage
FO	frustum orientation
I	coordinate grid index in direction of primary flow
J	coordinate grid index in direction normal to flat plate

K	coordinate grid index in direction transverse to primary flow
LabVIEW	Laboratory Virtual Instrumentation Engineering Workbench
LDA	laser-doppler anemometry
MEMS	micro-electro mechanical systems
NI	*National Instruments*
PIV	particle image velocimetry
Q	heat (energy)
Re	Reynolds number
RMS	root mean squared
S_{wet}	wetted surface
T_o	ambient temperature
T_w	wire temperature
Tu_u	x-component of turbulence intensity
Tu_w	z-component of turbulence intensity
U_∞	freestream velocity
UEI	*United Electronic Industries*
V_{vec}	velocity vector
$V_{eff\text{-}cal}$	effective velocity in calibration measurement
$V_{eff\text{-}exp}$	effective velocity in experimental measurement
V_{meas}	measured velocities with reference to wire-coordinate system (component)
VG	vortex generator
VMX	*Velmex*
$(\,')$	fluctuation component of velocity

$(\bar{\cdot})$	mean component of velocity

Greek Symbols

α	flow angle
β_{cal}	angle of the probe orientation in the calibration procedure
β_{cor}	corrected probe angle
β_{exp}	angle of the probe orientation in the experiment
β_{o}	probe angle oriented with the flow
Δ	interval size
δ	boundary layer height
ρ	density
μ	fluid viscosity
τ	shear stress
τ_{Re}	Normalized Reynolds Stress
$(\partial u/\partial y)$	velocity gradient

ACKNOWLEDGMENTS

After many late nights (and early mornings), trials of patience, and life on the first floor of the Rogers Building at Baylor, it is rewarding to see these fruits of labor and the hopes of more to come in the hands of others. However, this time could not have been possible without the assistance and encouragement of several people.

I would first like to extend my gratitude and appreciation to my advisor and mentor Dr. Stephen McClain, whose guidance, patience, and aid were vital to the success of this project. I would also like to thank Dr. Kenneth Van Treuren for his counsel and presenting me the prospect of continued studies at Baylor. Additionally, I would also like to thank Dr. Carolyn Skurla who provided me the first research opportunity that fueled my interest in graduate work, and Dr. Walter Bradley whose encouragement motivated me to continue with my studies.

I would also like to thank Steven Mart for his help with LabVIEW programming, editing, and test set-up, Mr. Ashley Orr for his aid in construction with this project, and both Mr. Pat Hynan and Mr. Dan Hromadka for computer and software technical assistance. Furthermore, I extend my thanks to Darrian Campbell, Kevin Coffman, and Shawn McGrath for previous construction of test apparatus to continue this project.

I must give my most sincere thanks to my parents for their financial and emotional support to make the journey to study here at Baylor. I am very grateful of theirs, my extended family's, and friends' love and prayers that have helped shaped me into the person I am today who ventures forward with faith, hope, and love.

DEDICATION

To my family and *abuelita*, whose love, prayers, and encouragement constantly remind me that *todo lo puedo en Cristo que me fortalece.*

CHAPTER ONE

Introduction

Boundary layer separation over a surface is an important phenomenon that has great implications on the aerodynamic performance of aircraft. The ability to control flow fields to improve performance and reduce drag is also important and driven by potential savings in fuel expenditures or expansion of the flight envelope.

Drag reduction may be achieved by preventing or delaying laminar-to-turbulent transition from occurring over the surface or by inducing turbulence to create a secondary flow motion that alters the flow field. Vortex Generators (VGs) represent a traditional solution to this challenge by inducing turbulence, and much research has been dedicated to studying their application in ducts, airfoils, rotorcraft blades, and gas-turbine blades for both flow and heat transfer purposes [1-6]. Additionally, winglets, used commercially on airliners, provide another method of decreasing drag by reducing wingtip vortices that produce induced drag [7, 8]. Both of these approaches are considered to be passive since the structures remain fixed in geometry. However, because of their geometry, these devices carry a skin friction drag penalty associated with the surface that is exposed to the flow.

The emergence of micro-electro mechanical systems (MEMS) has impacted the study of flow control and gained much attention in recent literature. The various types of MEMS include piezoelectric actuators, synthetic jets, plasma actuators, and bubble type actuators which are either used to create fluctuations at very particular frequencies in the flow to delay or promote transition without the undesirable drag effects associated with passive flow control devices.

While the research for flow control of separation on various surfaces with MEMS is extensive [1, 2, 9-13], there is still a lack of information about the development and control of spanwise flow over surfaces. By elongating and orienting surface features at an oblique angle to the freestream direction, it may be possible to control the magnitude and direction of the transverse flow. If the oblique angle of the elements are not too large to cause separation from the surfaces, the flow at the trailing edge of the control elements should leave tangentially and smoothly from the trailing edge.

This type of MEMS device is motivated by the natural flow control qualities that birds exhibit with their wings. During maneuvering, small fine feathers project form the main wings to either direct air in favorable paths or promote turbulence for better flow over the wing. Shown in Figure 1, the primary, secondary, and tertiary feathers respond to flow conditions and channel flow over the wing, and the alular feathers act as high-lift devices at the leading edge, generating vortices over the wing at take-off and landings [14-16].

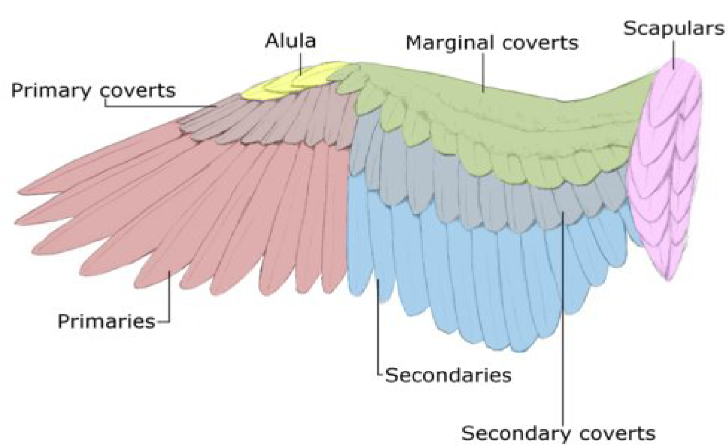

Figure 1: Bird Feathers

Although the construction of a MEMS device is not in the scope of this investigation, the ultimate goal of studying the flow field and turbulence quantities produced from aligned roughness elements would be to design a novel MEMS device. This device would not only decrease drag created from separation and skin friction, but also tailor flow in the spanwise direction to potentially reduce the wingtip vortices occurring at the ends of the wing when activated.

Many studies for flow control are completed using different experimental approaches including constant temperature anemometry (CTA) [1,10] for obtaining velocity fluctuations of high resolution, and particle image velocimetry (PIV) [2,13], laser doppler velocimetry (LDV) [6] or oil surfaces for flow visualization [2,17-19, 24, 25]. Another approach for investigating these flow qualities is to use computational fluid dynamics (CFD). Emerging with computer development in the early 1960s, CFD is a field of study dedicated to a numerical solution of the equations of fluid flow by applying conservation laws with boundary and initial conditions in mathematical discretized form to evaluate flow field variables on a discretized grid [17]. Both experimental and CFD approaches can be applied to complement each other in evaluating properties such as lift and drag and to determine details about the flow field. Thus, it is common practice to use experimental data to validate CFD solutions by matching experimental measurements to computational quantities. This allows for the ability to use CFD software with some confidence, reducing the costs and time involved in the design cycle.

The purpose of this investigation is to measure the flow qualities and turbulent intensities produced by arrays of 0°, 5°, 10°, and 15° obliquely-aligned, truncated elliptical cones (frustums) from upstream turbulent flow at 2, 5, and 10 m/s on a flat plate. Additionally, CFD simulations using the k-ε turbulence model are executed and compared to a limited amount of experimental results. The results will enable a study of aligned frustums' ability to produce a controlled secondary flow and the ability of commercially available CFD software to predict the experimental results.

CHAPTER TWO

Background

This chapter gives information regarding aerodynamics in terms of boundary layer development and drag, past studies regarding flow control, and fundamental principles of the experimental method.

Aerodynamics

A fluid can exert drag forces on to an airfoil that is immersed in flow by shear and pressure forces. Displayed in Figure 2, the shear stresses are applied parallel to the body while pressure is applied perpendicularly. A pressure difference between the top and bottom surfaces can be created by increasing the angle of the airfoil with respect to the chord line called the angle of attack (AOA). This acceleration moves the stagnation point from the front of the airfoil down to the lower surface, and forcing the flow to accelerate over the top surface. This produces a low pressure region on the top surface while the bottom surface contains a higher pressure region, creating a net upward force, or lift. Although pressure contributes to the drag force, a considerable amount is attributed to the shear stresses caused by the resistance of the fluid against the body creating friction [7].

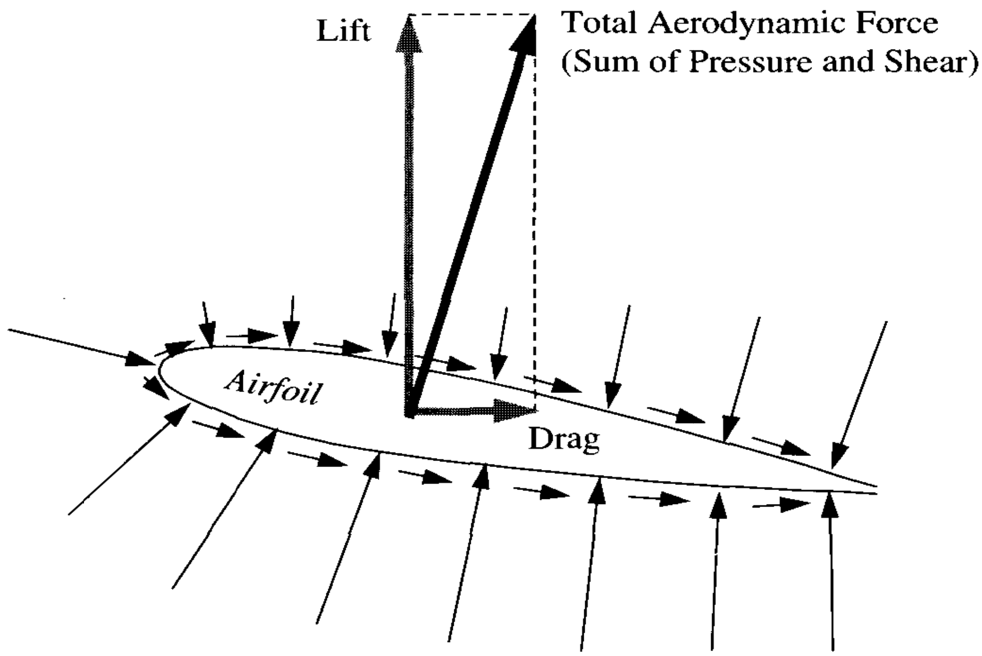

Figure 2: Forces on Airfoil [7]

Boundary Layers

The interaction of the fluid with a flat surface is modeled in Figure 3. The boundary layer is developed resulting in flow velocities which are less than the freestream velocity due to the fluid friction. Shown in Figure 3, the boundary layer on a flat plate may either be laminar, turbulent, or in transition depending on the Reynolds number, *Re*, which is defined by

$$Re = \rho U_\infty x_c / \mu \tag{1}$$

where U_∞ is the freestream velocity, x_c is the location on the plate, ρ is the fluid density, and μ is the fluid viscosity. The height at which the distance from the surface to a location where the streamwise velocity component is 99% of the freestream velocity is known as the boundary layer height δ.

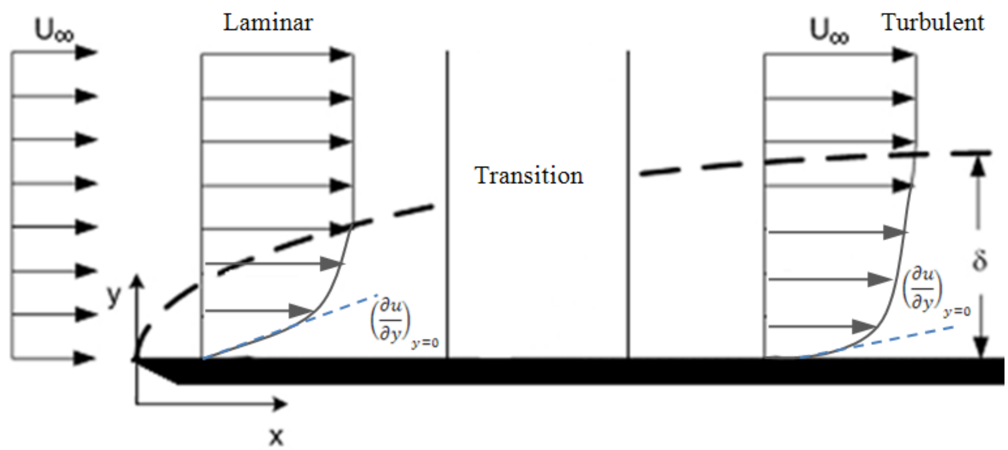

Figure 3: Boundary Layer Flow Profiles over a Flat Plate

The boundary layer profiles from Figure 3 show that the turbulent flow has a greater boundary layer height and a thicker profile that indicates there is more shear stress, τ, at the surface. The shear stress is defined as

$$\tau = \mu \left(\frac{\partial u}{\partial y}\right)_{y=0} \tag{2}$$

where $(\partial u/\partial y)$ is the velocity gradient at the surface. The increased shear occurs because of the difference in how mass, momentum and energy are transported. In laminar flow, the fluid particles travel in an organized behavior along streamlines in the flow. Eventually, the flow decomposes and transitions into a turbulent flow. Turbulent flow is characterized by fluctuations or spinning regions in the fluid called eddies that transport mass, momentum and energy much faster than diffusion. To account for these fluctuations, the instantaneous velocity at a point in space is described in Eq. (3)

$$u = \bar{u} + u' \tag{3}$$

where $\bar{u}$ is the mean value and u' is the fluctuating velocity. Then, the total shear stress in turbulent flow can be described by

$$\tau_{total} = \tau_{lam} + \tau_{turb} \tag{4}$$

where τ_{lam} is the laminar component described in Eq. (2) and τ_{turb} is the turbulent component known as the Reynolds stresses, shown in Eq. (5), is much greater than the laminar component within the viscous core of the boundary layer

$$\tau_{turb} = -\rho\overline{u'v'} \tag{5}$$

where $\overline{u'v'}$ is the time average product of fluctuating velocity components u' and v'.

Drag

For a two dimensional flow over an infinite airfoil, drag contributions come from the skin friction and pressure forces, which may be enhanced by flow separation. As mentioned earlier, the viscous effects in the boundary layer contribute to the shear stresses that define the skin friction drag. This type of drag contributes about 50% of total drag on a commercial airliner and may be minimized by reducing the surface exposed to the flow, S_{wet}, shown in Eq. (6)

$$D_f = \int_0^{S_{wet}} \tau_{total}\, dS \tag{6}$$

Another method for reducing the skin-friction drag would be to delay the transition to turbulence, which increases the laminar component and decreases the turbulent component of the shear stress [7].

Pressure drag caused by separation, shown in Figure 4, can occur if the angle of attack on an airfoil is too high. As the angle increases, the pressure difference between the top and bottom surfaces decreases as flow separation from the trailing edge begins to move upstream. When the flow is completely separated, a drastic decrease in lift occurs resulting in a stalled condition. The separation can be delayed by inducing turbulence to re-energize the flow because of a larger velocity gradient at the surface shown in the boundary layer model.

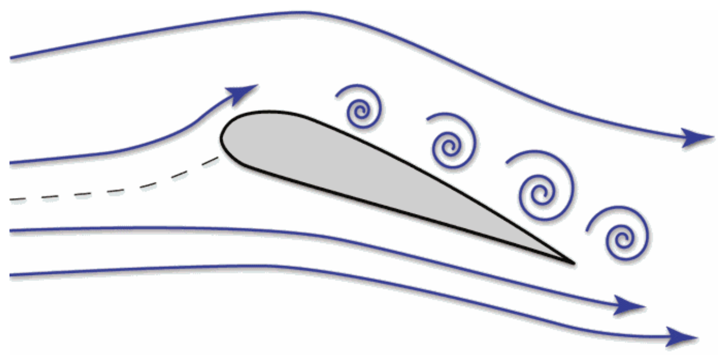

Figure 4: Flow Separation over an Airfoil

For a three-dimensional flow over a wing with a finite span, an additional component of drag must be taken into consideration. As the wing moves through the air, the pressure imbalance between the top and bottom surfaces are still present, yet at the wing tips, the high pressure air from the bottom surface migrates to the top surface. The circular motion creates a vortex structure around the wing tips, resulting in a downward component on the wing called a downwash, shown in Figure 5.

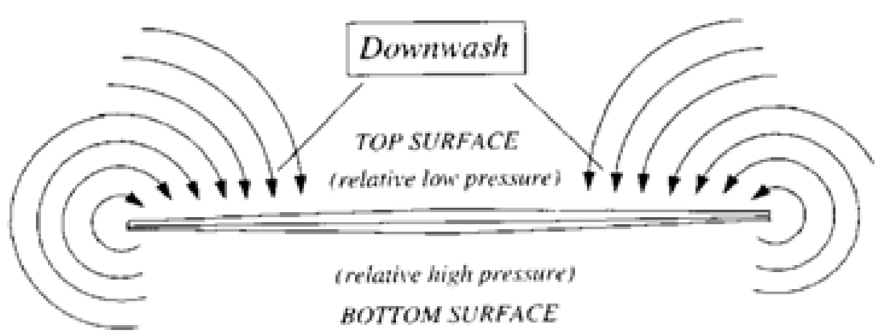

Figure 5: Front View of Downwash Effect on Wing [7]

Downwash changes the effective AOA by slanting the lift vector back slightly. The tilting results in induced drag or drag due to lift, displayed in Figure 6. Additionally, a spanwise flow on the wing occurs due to the pressure imbalance at the wingtips caused by wingtip vortices.

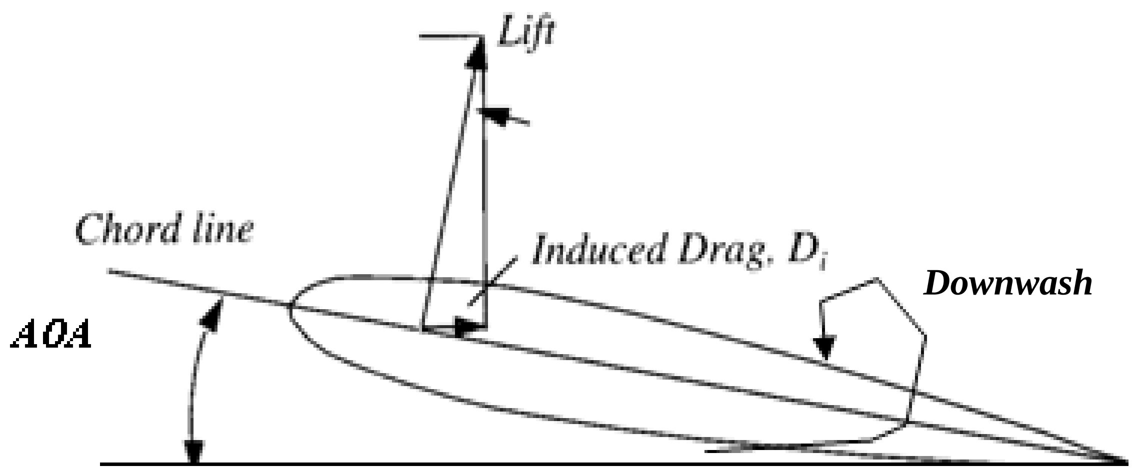

Figure 6: Induced Drag on Wing Profile [7]

The taper ratio and sweep angle of a wing also influences the amount of induced drag and strength of downwash [18, 19]. Most aircraft have a change in the chord length from the fuselage to the wingtip. With a smaller chord length at the tip, a stronger downwash effect is created that adds more load and may result in tip stall. This effect is amplified with a swept wing as the spanwise flow towards the tip results in boundary layer thickening that may cause earlier flow separation and tip stall at high angles of attack [20]. The tip stall also causes the wing's center of lift to move closer to the leading edge with the flow separation causing a loss in lift on the trailing edge and, consequently, a loss in aileron effectiveness. In particular, these negative results can have disastrous implications at the low speeds required for take-off and landing, prompting the desire to reduce the transverse flow across the airfoil.

Flow Control

The need for flow control is evident in the discussion of drag and the desire to improve aircraft performance. The following presents an overview of flow control and related studies regarding flow control and MEMS devices.

For maintaining laminar flow, one approach is to drill numerous tiny holes along the surface of the wing to create a suction that could pull the air inside wing keeping the boundary layer attached [7]. Using the same holes, air from the jet compressor of the aircraft could be used to create synthetic jets on the surface to delay separation by inducing turbulent flow [7, 21]. However, this method of tooling holes requires rigorous engineering to account for the manufacturing and operational issues that may arise. Additionally, more research is required concerning the changing operational environment that may affect the pores such as icing or insect debris [22].

An alternative method for laminar flow control involves using spanwise distributed roughness [22, 23]. Regarding vortex generators, Lin et al. [24] used static pressure measurements, surface oil visualization, and a small force balance to investigate small submerged vortex generators in a spanwise array. With a height about 10% of the boundary layer thickness, the submerged vortex generators performed as well as a conventional vane-type vortex generator with a height an order of magnitude higher, leading to the possibility of micro-vortex generators and MEMS.

With similar experimental techniques as Lin et al., Selby et al. [25] conducted a parametric study of jet vortex generators for a low-speed two-dimensional turbulent flow separation control, with variations in the orifice diameter, jet orientation, jet speed, longitudinal hole location and pattern. The study revealed that jets oriented to produce co-rotating vortices have less variability in spanwise pressure distributions than jets oriented to produce counter-rotating vortices. Furthermore, this effect is non-linearly reinforced with a second row of jets.

Although over a decade since its publication, Lofdahl and Gad-el-Hak [9] is one of the most complete reviews of MEMS and focuses on the different features of both passive and active flow control. Since then, several research groups have investigated the use of piezoelectric actuators and jets that oscillate for flow control [26-32].

In application to an airfoil, Zhang et al. [1] used Piezo-ceramic actuators to suppress boundary layer separation on a NACA 0015 airfoil and were able to extend the stall angle of attack by 2° if the perturbation frequency was at least 10 times larger than the dominant frequency of vortex shedding. In this study, PIV provided flow field measurements and two single hot wire probes, upstream and downstream, were used as signals for capturing boundary layer separation.

Gilarraz et al. [2] investigated flow separation control for a NACA 0015 using synthetic jet actuators and increased the stall angle by 6°. The jets augmented the lift in cases where massive separation occurs with larger frequencies of actuation. For this investigation, flow visualization oils were used on the airfoil and surface pressure measurements were collected from pressure taps along the airfoil.

Similar to air jets, Tung et al. [33] created a MEMS-based micro-balloon system. This system distinguishes itself from synthetic jets by using jet flow to inflate a sealed, pre-shaped perturbation on the surface independent from the environment conditions. The life cycle testing of 11,000 inflations and deflations at transonic speeds demonstrated that this system is feasible and survived realistic conditions. This type of MEMS-based system would be the most applicable to the goal of this project.

Constant Temperature Anemometry

Constant Temperature Anemometry (CTA) has the ability to measure velocity fluctuations, mean velocity, turbulence intensity and other higher order turbulence moments. The CTA system, when coupled with a traverse mechanism, can be used to map the boundary layer flow field. The components required to make anemometry measurements are shown in Figure 7.

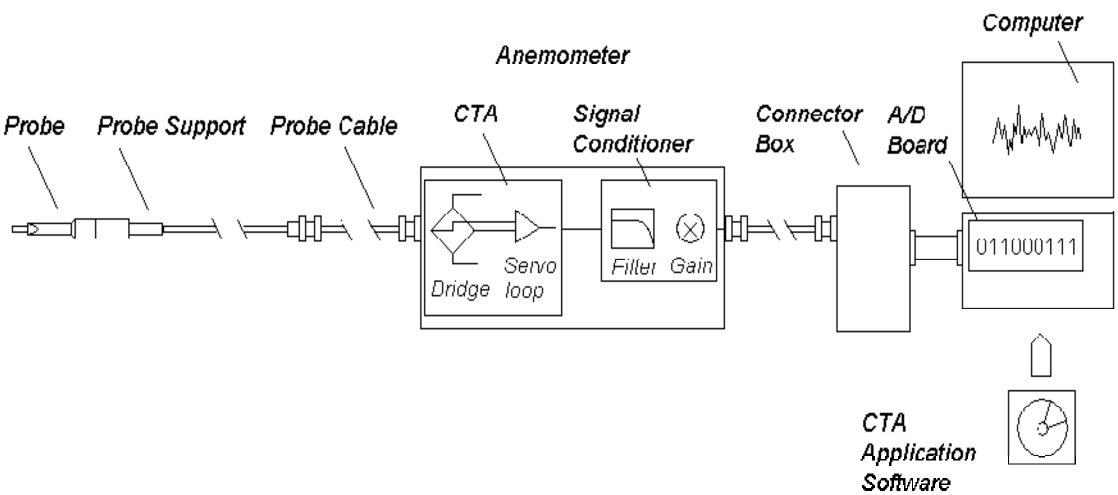

Figure 7: CTA Measuring Chain Components [34]

A CTA system operates on the basis of convective heat transfer, Q, from a heated cylinder (wire) in a fluid and is a function of velocity, u, the wire over-temperature T_w-T_o and the physical properties of the fluid. The fundamental relation between Q and u for a wire placed normal to the flow is given by King's Law in Eq. (7)

$$E^2 = Q = (T_w - T_o)A_w h = A + BU^n \tag{7}$$

where E is the bridge voltage, A_w is the wire surface area, h is the heat transfer coefficient of the material, and A, B, and n are arbitrary calibration constants. The hot-wire probe, displayed in Figure 8, is usually composed of tungsten wire that is spot-welded to two needle-shaped stainless steel prongs. Common configurations for the probe are shown below with 1, 2, or 3 wires to measure the desired velocity components. For probes containing 2 or 3 wires, directional calibration is also required to extract the velocity components.

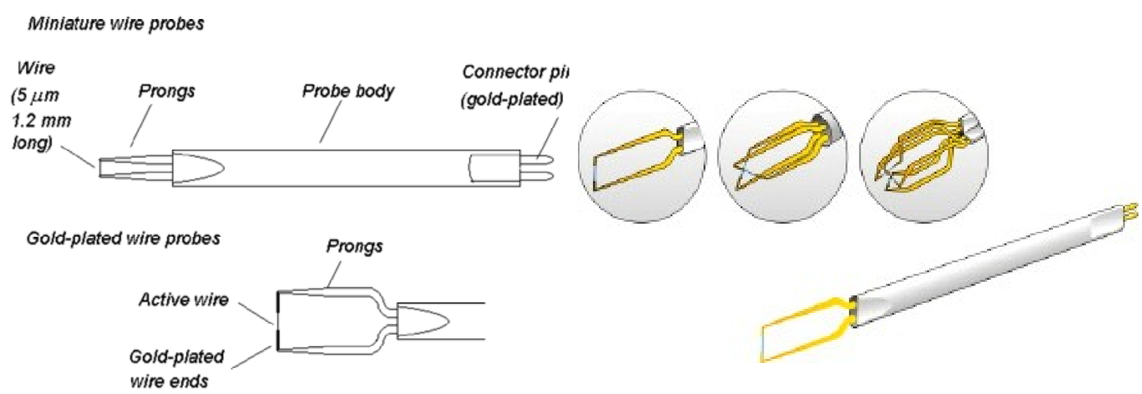

Figure 8: Hot-Wire Probe Components and Configurations [34]

The operating principle for CTA is explained with the Wheatstone bridge and Servo amplifier configuration shown in Figure 9. The hot-wire probe is connected to one arm of the Wheatstone bridge opposite to the variable resistor which is used to define the operating resistance and the hot-wire temperature.

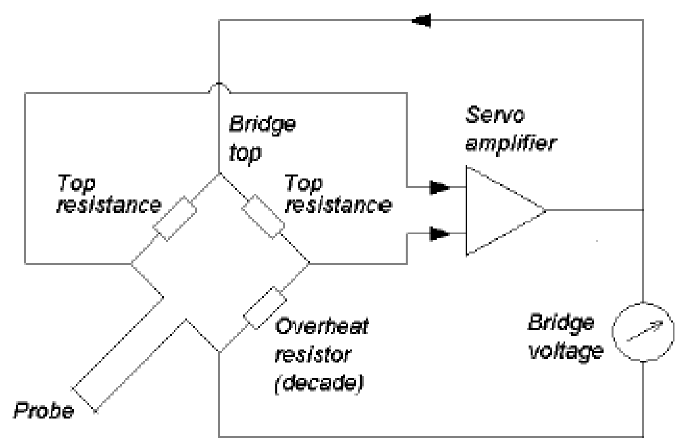

Figure 9: Constant Temperature Anemometer

If the bridge is balanced, no voltage difference exists across the diagonal. If the flow velocity increases, the wire resistance will increase and prompts the servo amplifier to increase the probe current until the wire is heated to the operating temperature and the bridge balance is restored. The bridge voltage squared, E^2, then represents the heat loss from the wire Q and this voltage can be correlated to the velocity using either King's law or a polynomial curve fit.

CHAPTER THREE

Experimental Method

This chapter describes the testing facility, test coupons, instrumentation, and overall set-up including data acquisition. Furthermore, the velocity and directional calibration of the hot-wire probes are described as well as the testing procedure used with the *LabVIEW* program. How voltages from the hot-wire probes were translated and reduced to meaningful quantities is presented. An uncertainty analysis of the measurements is also discussed.

Apparatus & Set-up

The experiment was performed in the Baylor University Subsonic Wind Tunnel (Model 406) which is manufactured by Engineering Laboratory Design, Inc., displayed in Figure 10. The wind tunnel test section has a cross-section of 60.96 cm x 60.96 cm and uses a 40 HP electric motor that drives a constant pitch fan. The variable speed motor can produce a flow ranging from a low velocity of 0.1 m/s to an upper tunnel velocity greater than 50 m/s. Tunnel velocity variation over the test section is less than +/- 1 %. An inlet contraction ratio of 6.25:1, a precision honeycomb inlet, and three graduated, high-porosity screens provide a clean inlet turbulence intensity of approximately 0.2%.

To investigate flow characteristics of the control elements, a 91.44 cm x 60.69 cm x 1.905 cm flat plate was constructed using Plexiglas with a 20.32 cm x 20.32 cm x 0.635 cm section milled out of the plate. The section was removed so that test coupons with different arrays of control elements could be installed onto the test plate at a distance of 0.6 m from the leading edge of the flat plate. At the bottom of this section, five countersunk holes were drilled in order to fasten the test coupon along the surface to the flat plate. The flat plate was raised 29.845 cm from the wind tunnel test section floor by four support rods.

Figure 10: Baylor University Subsonic Wind Tunnel

Five test coupons were created from ABS plastic using a Dimension SST-768 3-D Rapid Prototype Printer. Four of the test coupons were created with arrays of elliptical frustums with a ratio of major axis to minor axis of 5.0 and with a vertical taper angle of 20°. The length of the elements along their major axis was 3.048 cm. The elements were placed in three staggered rows of nine roughness elements that were 0.635 cm tall, equally distributed laterally, and spaced every 3.937 cm in the flow direction. The height of the control elements was chosen so that the elements would be approximately 20% of the smooth-surface laminar boundary-layer thickness for a nominal flow velocity of 3.2 m/s at a location 0.6 m from the knife edge of the plate. These coupons were assigned an individual angle of alignment for the frustums of 15°, 10°, 5°, and 0° from the streamwise axis. The fifth coupon was created without any elements to be used as a baseline control. A sample test coupon and its placement in the flat plate are shown in Figure 11.

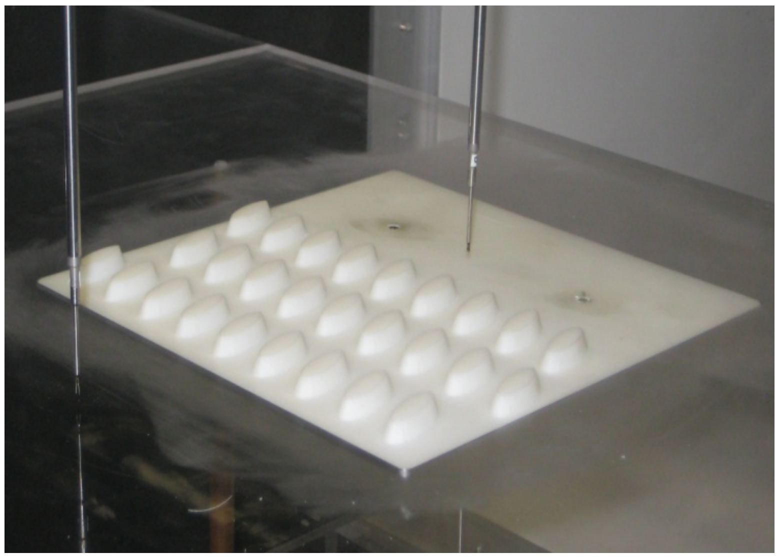

Figure 11: Test Coupon on Flat Plate with Hot-Wire Probes

A traversing system was constructed to position hot-wire, X-array probes upstream and downstream of the flow control elements. The X-array probes are aligned to measure the freestream direction component and the transverse component boundary-layer velocity profiles. The upstream traversing system includes a *Velmex BiSlide* assembly for the measurements with a TSI 1247A Miniature Cross Flow X- probe attached by a 45.72 cm probe support located 4.254 cm upstream of the first array of elements at centerline and 57.658 cm from the leading edge of the flat plate. A *Velmex* (*VMX) BiSlide*/*Unslide* assembly was used for two-dimensional traversing downstream measurements with another TSI 1247A Miniature Cross Flow X-wire probe located approximately 2.908 cm downstream of the last array of elements and 76.708 cm from the leading edge of the flat plate. Both of these positioning systems were connected to a *VMX* Stepping Controller interfaced with a *Dell Optiplex GX260* computer through an RS-232 serial connection.

The X-wire probes were powered by the IFA 300 Constant Temperature Anemometer system. The Thermal Pro software on a second personal computer, a Dell Optiplex GX1, was used to assign the channels to the probes and function as a signal conditioner to input the gain and offset of measurements. A Omega Cold Junction Compensator with a Type T thermocouple was used to measure the freestream temperature, a Siemens QFM3101 Relative Humidity Sensor measured the relative humidity in the laboratory, a Oakton Thermometer/Barometer was used to measure the laboratory atmospheric pressure, and a 15.24 cm Pitot-static probe was connected to a Omega PCL-2A Pressure Transducer to measure the freestream velocity in the wind tunnel. Figure 12 shows the traversing system used for the boundary layer measurements and the position of the other instrumentation.

The Dell Optiplex GX260 computer with *National Instruments (NI) LabVIEW* 7.1 software was used for all traverse control, instrumentation and data acquisition. Various *LabVIEW* virtual instruments (VIs) were created for traverse stage control, data acquisition, and data storage for the experimental measurements. The stepper motor controller for the positioning system and pressure transducer were individually linked to the computer via RS-232 serial port communication. The computer contained two DAQ cards: a *PCI-6052 E Multifunction* DAQ card and a *United Electronic Industries (UEI) PD2-MFS-4-300/16 PowerDAQ* card. The relative humidity and freestream temperature were measured using a *PCI-6052 E Multifunction* DAQ card with an *NI BNC 2110* Shielded Connector Block. To obtain simultaneous sampling from the hot-wire anemometry system, the *UEI PowerDAQ* was employed. Barometric pressure measurements from the analog Oakton barometer were manually recorded at the beginning of a test case and entered into the data acquisition VI. Figure 13 presents the experimental apparatus and instrumentation.

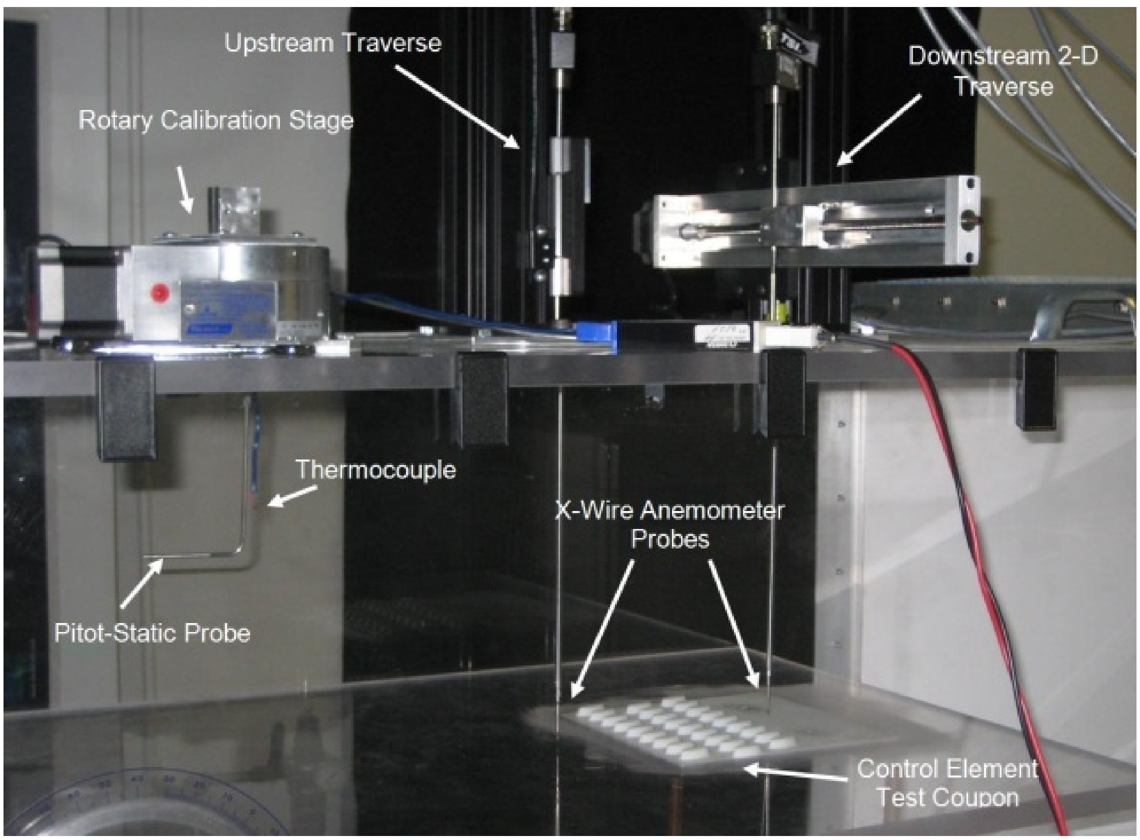

Figure 12: Measurement System Installed in Baylor University Subsonic Wind Tunnel

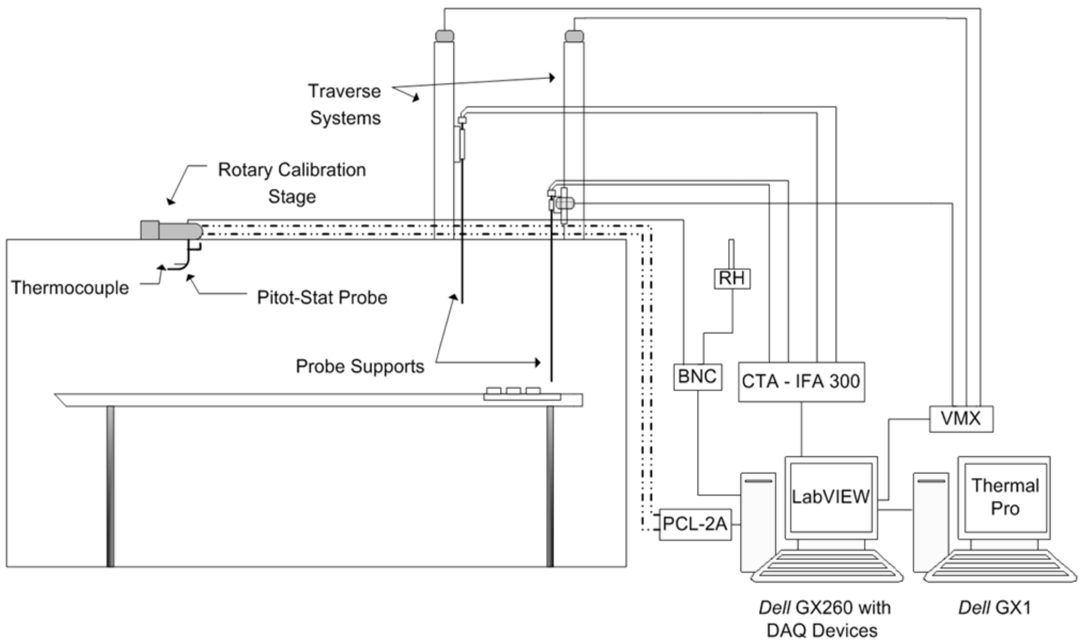

Figure 13: Schematic of Wind Tunnel Measurement and Control System

Calibration

The velocity and directional calibration of the X-wire probes were performed simultaneously. The X-wire probe was mounted on the *Velmex* B487TS motorized rotary table at the same height where the Pitot-static tube was located and 30.48 cm away in the z-direction. Using the *Thermal Pro* software, the manufacture's probe resistance and cable resistance for the X-wire probe were specified with both gain and offset to maximize the resolution on a 0-5V scale. A virtual instrument in *LABVIEW* was created to automate the movement of the rotary table and measure the voltage of the probe in 5° intervals over a range of $\pm$20°. This process was repeated for the velocities ranging from 0-20 m/s at 2 m/s intervals for both X-wire probes.

To give accurate linearization results, the acquired voltages were re-scaled back to their raw voltages by dividing the gain and subtracting the offset. Since the various measurement angles and at different velocities were measured, the velocity calibration can be more accurate by using the whole range of effective velocities for curve-fitting with the voltage measurements. In this case, the effective velocities are dependent on the yaw coefficients (directional sensitivity coefficients) which are determined empirically; the optimal velocity calibration is dependent on the directional calibration of the probe, shown in Figure 14.

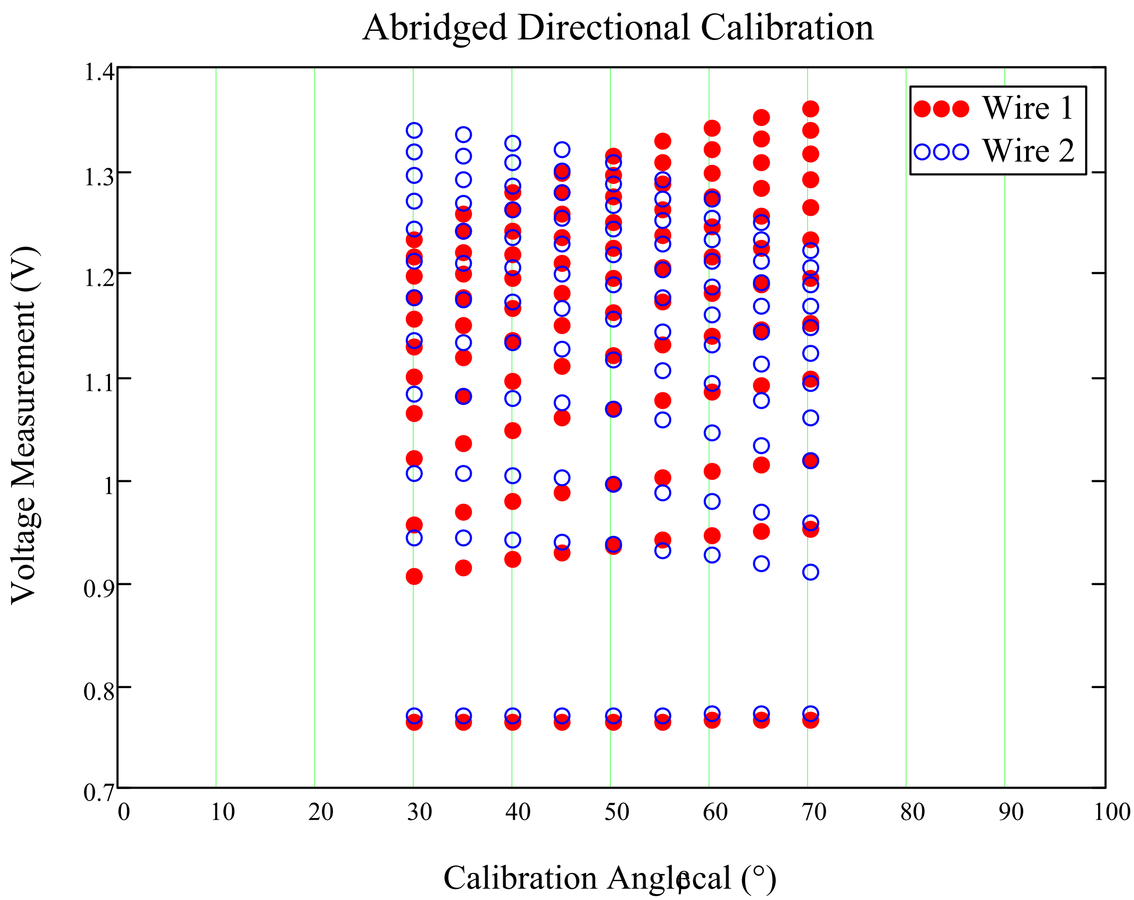

Figure 14: Abridged Directional Calibration Plot

To determine the effective velocities, a coordinate system is set with respect to the wires with velocity measurements from the Pitot-static tube and the relationship between them is defined by

$$V_{eff-cal,1} = \sqrt{V_{meas,x}{}^2 + k_1{}^2 V_{meas,z}{}^2} \tag{8}$$

$$V_{eff-cal,2} = \sqrt{V_{meas,x}{}^2 + k_2{}^2 V_{meas,z}{}^2} \quad (9)$$

where $V_{eff\text{-}cal,1}$ *and* $V_{eff\text{-}cal,2}$ are the effective velocities in calibration for wires 1 and 2 of the probe, $V_{meas,x}$ and $V_{meas,z}$ are the velocities with reference to the wire-coordinate system, and k_1 and k_2 are the yaw coefficients for wires, respectively. Then, the yaw coefficients are empirically found in order to match the effective velocity with the probe voltages with a curve fit. The linearization of the voltages and velocities is defined by a 9th order polynomial to estimate the calibration data, shown in Figure 15. Pearson's R correlation for wires 1 and 2 are 99.9998% and 99.9920%, respectively.

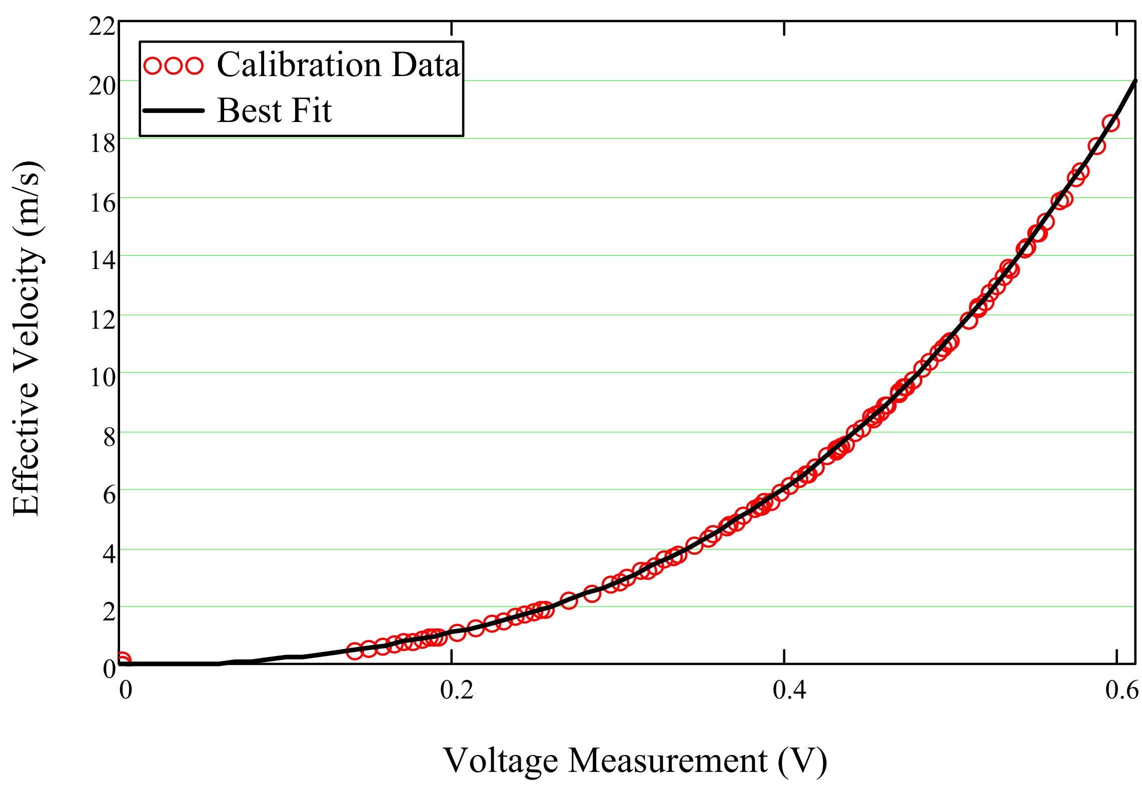

Figure 15: Directional Calibration Plot

Test Procedure

For each coupon tested, the wind tunnel was set to the desired velocity by adjusting the fan frequency of the wind tunnel. At each measurement station, the flow, atmospheric conditions and hot-wire probe voltages were sampled, then the probe was moved and paused for approximately 3 seconds before taking another sample. The upstream probe measurement started at the height of 0.404 cm from the flat plat to avoid damage to the X-wire probe. The probe traversed 15.24 cm in the y-direction measuring the flow at 101 stations with a geometric expansion factor of 1.07. After the upstream measurements concluded, the probe remained 15.24 cm above the flat plate. The downstream probe then traversed in the y and z-directions. At each z-station, the downstream probe traversed in the same manner as the upstream probe, with the same starting height, distance traveled, geometric spacing interval, and number of data points in the y-direction. The profile measurement process was repeated for every 1.27 cm spanwise across the test coupon to create a 20.32 cm x 15.24 cm boundary layer measurement plane. With all measurements concluded, the probes were returned to the origin positions and the *LabVIEW* session concluded. The test procedure was then repeated for the additional velocities tested.

For every point in the calibration and experimental tests, the data acquisition system measured 200,000 samples at a rate of 200,000 samples per second for the relative humidity, free stream temperature, and each channel of the hot-wire anemometry system. A summary file was created containing the averaged values and random uncertainties of each measurement point throughout the experiment. The measurement files contained the following data (random uncertainties for measurements are identified with an asterisk): measurement reference number, date, time, X-wire probe positions: upstream, downstream y-axis and z-axis, time elapsed, atmospheric pressure, relative humidity*, free stream temperature*, dynamic pressure*, and X-wire probes voltages*.

In addition to the summary file, the 200,000 raw voltage samples from the anemometer probes at each measurement station were documented into the appropriate velocity profile folder with a file name indicating the data point. A detailed discussion of the *LabVIEW* automation and DAQ is described in Appendix A.

Data Reduction

The measurements from the lab equipment for each test case were saved on a summary file, and individual files were created for the probe voltage measurements and their respective uncertainties. The measurements of temperature, pressure, and density were used to relate the calibration data to the experiment. The probe measurements were rescaled to negate the offset and gain and used the linearization curve-fit described in the calibration section to obtain the effective velocities by the following equations.

$$V_{eff-exp,1} = \sqrt{\frac{{V_{exp,1}}^2-(k_1\, V_{exp,2})^2}{1-{k_1}^2\, {k_2}^2}} \tag{10}$$

$$V_{eff-exp,2} = \sqrt{\frac{{V_{exp,2}}^2-(k_2\, V_{exp,1})^2}{1-{k_1}^2\, {k_2}^2}} \tag{11}$$

Additionally, the velocities were decomposed into intermediate *u* and *w* velocities by the following equations:

$$u_{int} = \frac{1}{\sqrt{2}}(\, V_{1,eff-exp} + V_{2,eff-exp}) \tag{12}$$

$$w_{int} = \frac{1}{\sqrt{2}}(\, V_{1,eff-exp} - V_{2,eff-exp}) \tag{13}$$

These components are considered intermediate measurements because an angle correction is needed to account for the difference probe orientation with respect to the flow, where β_o is the probe angle oriented with the flow. The necessary correction is done by obtaining the velocity vector from the effective velocities and the intermediate angle with the following equations.

$$V_{vec} = \sqrt{u_{int}^2 + w_{int}^2} \tag{14}$$

$$\beta_{exp} = \sin^{-1}\left(\frac{w_{int}}{[u_{int}^2 + w_{int}^2]^{\frac{1}{2}}}\right) \tag{15}$$

where β_{exp} is the angle of the probe orientation in the experiment. This angle is added to the angle measured in calibration in order to reach a *w* velocity that is approximately zero in the freestream measurements and would then give the "true" velocity components of *u* and *w* given by:

$$u = V_{vec}\cos(\beta_{cor}) \tag{16}$$

$$w = V_{vec}\sin(\beta_{cor}) \tag{17}$$

where β_{cor} is the corrected angle defined in Eq. (18)

$$\beta_{cor} = \beta_{exp} - \beta_0 \tag{18}$$

These "true" velocities are found for all 200,000 samples and the mean velocities for a single point measurement are reported in the results and are described by

$$\bar{u} = \frac{1}{N}\sum_{i=1}^{N} u_i \tag{19}$$

$$\bar{w} = \frac{1}{N}\sum_{i=1}^{N} w_i \tag{20}$$

where u_i and w_i the individual measurement velocity and *N* is the number of samples. The flow angle of the measurements was calculated in the following equation:

$$\alpha = \sin^{-1}\left(\frac{\bar{w}}{[\bar{u}^2 + \bar{w}^2]^{\frac{1}{2}}}\right) \tag{21}$$

The instantaneous velocity fluctuation and mean velocity fluctuation are displayed, respectively,

$$u'_i = u_i - \bar{u} \tag{22}$$

$$w'_i = w_i - \bar{w} \tag{23}$$

$$u_{rms} = \sqrt{\frac{1}{N-1}\sum_{i=1}^{N}(u'_i)^2} \tag{24}$$

$$w_{rms} = \sqrt{\frac{1}{N-1}\sum_{i=1}^{N}(w'_i)^2} \tag{25}$$

With these quantities the turbulence intensities for both u and w were found by the equations

$$Tu_u = \frac{u_{rms}}{U_\infty} \tag{26}$$

$$Tu_w = \frac{w_{rms}}{U_\infty} \tag{27}$$

Finally, the Reynolds normalized shear stress in the lateral direction is defined by the shear force per unit area due to the eddy motion of the fluid particles and is described by the equation

$$\tau_{Re} = \left[\frac{1}{N}\sum_{i=1}^{N}(u'_i)(w'_i)\right]/{U_\infty}^2 \tag{28}$$

Uncertainty Analysis

With the DANTEC guide as a map for investigating uncertainty for the velocity measurements [34], the Kline and McClintock method was used to calculate the uncertainty using the multiple sample technique [35,36] to incorporate calibration and data acquisition errors into the experimental readings. The random uncertainties for all instrument readings throughout the uncertainty analysis were executed with a Student's t value for 95% confidence by a *LabVIEW* VI. The fixed and random uncertainties from the calibration file are based on instruments measuring the laboratory environment and pressure transducer for dynamic pressure. The uncertainty from the linearization process is described by the standard deviation of the curve fitting errors in the calibration points. For data acquisition, the sensitivity factor is given by the slope of the inverse calibration curve while the resolution of the A/D board serves as the instrumental uncertainty and contributes less than 0.01% uncertainty for a velocity measurement of 10 m/s. These uncertainties are set as either fixed or random uncertainties appropriately for the voltage inputs in order to be propagated throughout the experimental measurements. For the experimental velocity uncertainties, the probe positioning is normally negligible [34]. The angle correction procedure described earlier ensures the correct orientation of the probe with respect to the flow. Additionally, the temperature variations and changing densities, which incorporate humidity, were also considered for the experimental velocities.

The reported values for the velocity measurements are, with 95% confidence, believed to lie approximately within ±1.6%, better than the DANTEC estimated value of relative uncertainty [34]. As predicted from [34], the calibrator and linearization uncertainties were major contributors accounting for approximately 60.8% and 90.1% of the uncertainty velocities for wires 1 and 2, respectively. The uncertainty measurements for the calculated flow angle is ±0.92°. A detailed example for uncertainty analysis and calculation of a velocity and flow angle measurement can be found in Appendix B.

CHAPTER FOUR

Numerical Method

The computational model was created using *SolidWorks* for the control elements surface and *GAMBIT 6.3* for defining the wind tunnel, assigning nodes, and meshing volumes in the numeric study. The numerical code used to obtain predictions from the experimental settings was *ANSYS FLUENT 12.0*, a commercially available CFD software package capable of modeling fluid flow and heat transfer for a variety of applications using finite volume discretization. Within the CFD program, the freestream velocity, U_∞, was set at 10 m/s with turbulent conditions to simulate the steady-state flow of the computational mesh systems of approximately 1.13×10^6 nodes. Additionally, a grid independence study was conducted for the 15° roughness elements orientation for coarse, medium, and fine computational mesh systems consisting of approximately 4.27×10^5, 7.70×10^5, and 1.13×10^6 nodes, respectively.

Meshed Grid

To conserve computational space and computer memory, the model is limited to the top portion of the wind tunnel test section area to the top of the flat plate and defined by the Cartesian dimensions 85.09 cm x 30.48 cm x 60.96 cm (x, y, z). The computational domain is separated into four different regions with connecting faces and mesh types as shown in Figure 16. The four regions are identified as 1) the inviscid entry region, 2) the upstream region, 3) the control element region, and 4) the downstream region. The roughness elements file used to create the flow control plate for the experimental study was lengthened to dimensions 27.94 cm x 0.635 cm x 60.96 cm to create a symmetrical model to be imported into GAMBIT and used for the both the control element and downstream regions. Due to the complex geometry and meshing scheme of the control element region, this region was meshed first, followed by the downstream region, upstream region, and inviscid entry region.

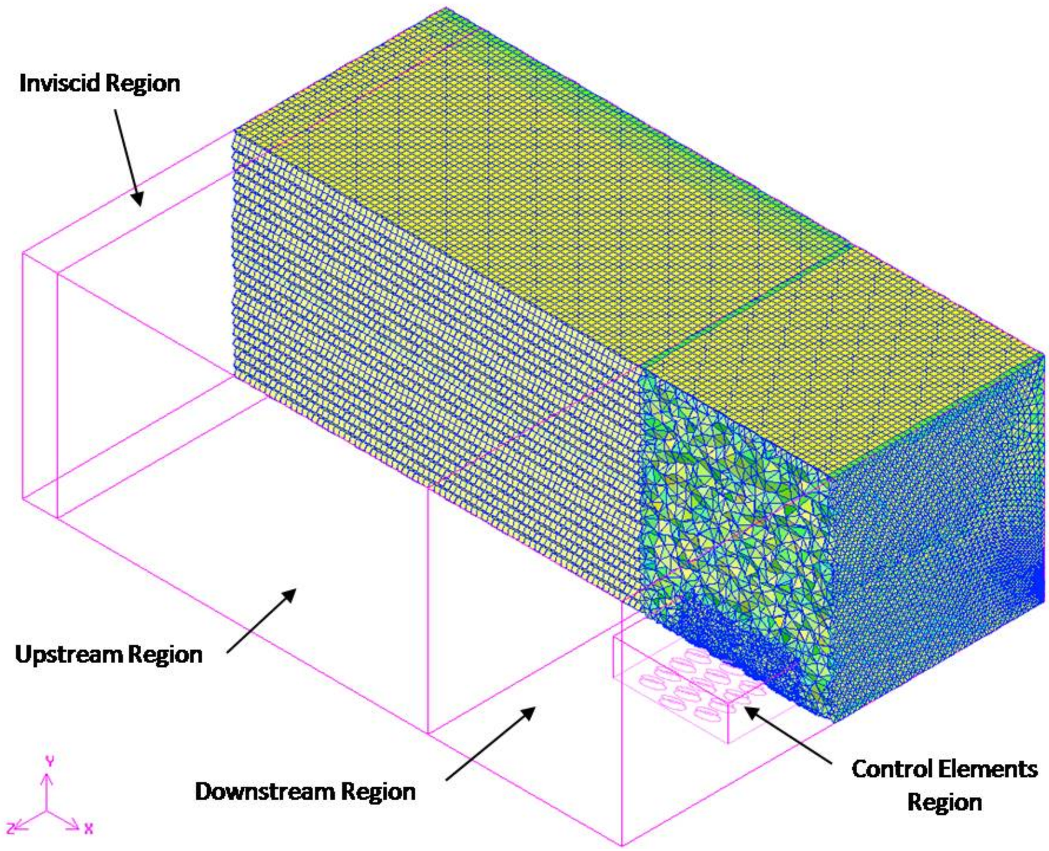

Figure 16: Coarse Grid Wind Tunnel Centerline Slice

The control element region contained the roughness elements in a 16.51 cm x 5.08 cm x 20.32 cm box volume containing approximately 2.55 x 10^5 nodes with the global origin centered in z approximately 2.159 cm upstream from the first row of roughness elements. The outer edges of the top and bottom planes of the region were defined by (43 x 53) and (65 x 80) grid points in (*I, K*), respectively, with uniform node interval sizes Δx, Δz = 0.381 cm and 0.254 cm, respectively. Additionally, the bottom plane includes a number of nodes for each roughness element in the (*I, K)*. The top and bottom edges of each element have 48 nodes each, respectively, and the vertical edges have 8 nodes. For the vertical edges of the box volume, there were 27 nodes (Δy = 0.1905 cm) with a geometric spacing distribution of 1.07 towards the bottom of the plate to cluster the nodes on the surface for the boundary layer development. Due to the node distribution from the elements, the mesh system was specified by a *Tetrahedral/Hybrid* type pattern, in which there is a hybrid of tetrahedral, pyramidal, and wedge elements (*T-Grid*) with the faces meshed with an irregular triangular scheme (*Tri-Pave*), displayed in Figure 17.

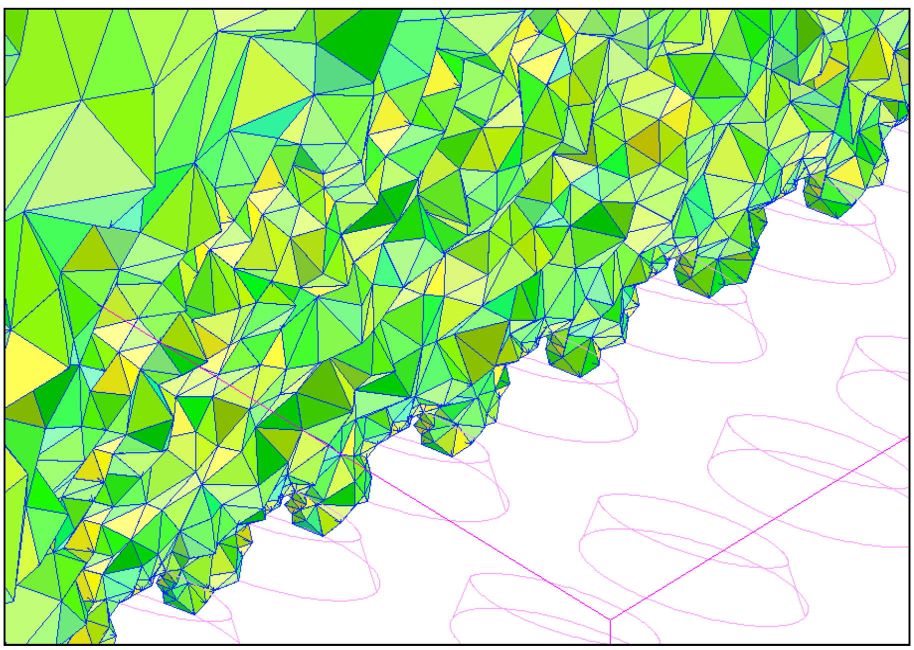

Figure 17: Tetrahedral Hybrid elements in Control Elements Region

The downstream region includes a 27.94 cm x 30.48 cm x 60.96 cm box volume containing 1.25 x 10^5 nodes with the local origin offset 6.35 cm upstream from the global origin, located 1.78435 cm from the first row of frustums. This region contains the volume surrounding the outside of the control element region and extends to the end of the flat plate model. The top and bottom plane edges were defined by 49 x 107 grid points in *(I, K)* with uniform node interval size Δx, Δz = 0.5715 cm, and the vertical edges contained 69 *J* grid points (Δy = 0.4445 cm) with a geometric spacing distribution equal to 1.05. With exception to the top plane face that is meshed as a Cartesian coordinate plane, the downstream region faces were meshed with *Tri-Pave* scheme and contained the *Tetrahedral/Hybrid* type elements similar to the control element region.

The upstream region included approximately 7.07 x 10^5 grid points enclosed in a 58.42 cm x 30.48 cm x 60.96 cm box volume located between the inviscid and downstream regions and represented the majority of the flat plate. The node assignment and spacing were the identical to the downstream region and contained (93 x 69 x 107) grid points *(I, J, K)* on the outer edges. Due to the location of the region, the mesh was defined by a *Cooper* type pattern, using the *Tri-Paved* meshed faces in the *J, K* planes from the Inviscid and Downstream regions as "source faces" and *Quad-Mapped* plane faces in *I, J* to create hexahedral and wedge elements (*Hex/Wedge*) throughout the volume.

The Inviscid Region represented the steady flow of uninterrupted freestream velocity and contained approximately 4.00 x 10^4 grid points inside a 5.08 cm x 30.48 cm x 60.96 cm box volume. The node assignment and spacing are the identical to the Downstream region with (107 x 69 x 9) grid points in *(I, J, K)* on the outer edges and also used the *Cooper* type meshing scheme with the inlet and interior face assigned as the "source faces" with the *Quad-Mapped* plane faces to create the mesh. A summary of the mesh and node edge assignments for the grid are shown in Table 1.

Table 1: Mesh and Edge Node Assignments for Fine Mesh

Region	*Mesh Type*	*Mesh Elements*	*Edges*	*Ratio*	*Interval Size (Δ) cm*	*Edge Nodes*
Control Elements	T-Grid	Tet/Hybrid	Top - *I* Top - *K*	1.00	0.3810	53 43
			Bottom - *I* Bottom - *K*	1.00	0.2540	80 65
			Vertical	1.07	0.1905	27
			Roughness - *I, K* Roughness - *J*	1.00	N/A	3 8
Downstream	T-Grid	Tet/Hybrid	Top, Bottom - *I* Top, Bottom - *K*	1.00	0.5715	107 49
			Vertical	1.05	0.4445	69
Upstream	Cooper	Hex/Wedge	Top, Bottom - *K*	1.00	0.5715	93
Inviscid	Cooper	Hex/Wedge	Top, Bottom - *I* Top, Bottom - *K*	1.00	0.5715	107 9
			Vertical	1.05	0.4445	69

Boundary Conditions

The *velocity inlet* boundary condition was assigned to the left face (-x direction) of the Inviscid region and U_∞ = 10 m/s with atmospheric conditions, turbulence intensity Tu = 0.2%, and an estimated turbulence length scale l = 2.032 cm. Although only the turbulence intensity from the wind tunnel is known, the FLUENT software recommends an estimated turbulence length scale can be found from the following equation:

$$l = 0.4\delta \tag{29}$$

where δ is the boundary layer thickness. The other faces of the Inviscid Region, with the exception of the right face (+x direction), were specified as *symmetric* to ensure U_∞ is initialized without no-slip effects from the walls. *Interior* boundary types were specified for other faces that connect the different regions in the model. *Wall* type boundaries were used to enforce the no-slip condition on the walls of the wind tunnel test section (top and side faces), the flat plate, and roughness elements (bottom faces) located throughout the upstream, downstream, and control element region. The pressure outlet boundary condition was assigned at the right face (+*x* direction) of the downstream Region to simulate the atmospheric pressure at the flow outlet of the test section area in the wind tunnel. A summary of the assigned boundary conditions is shown in Figure 18.

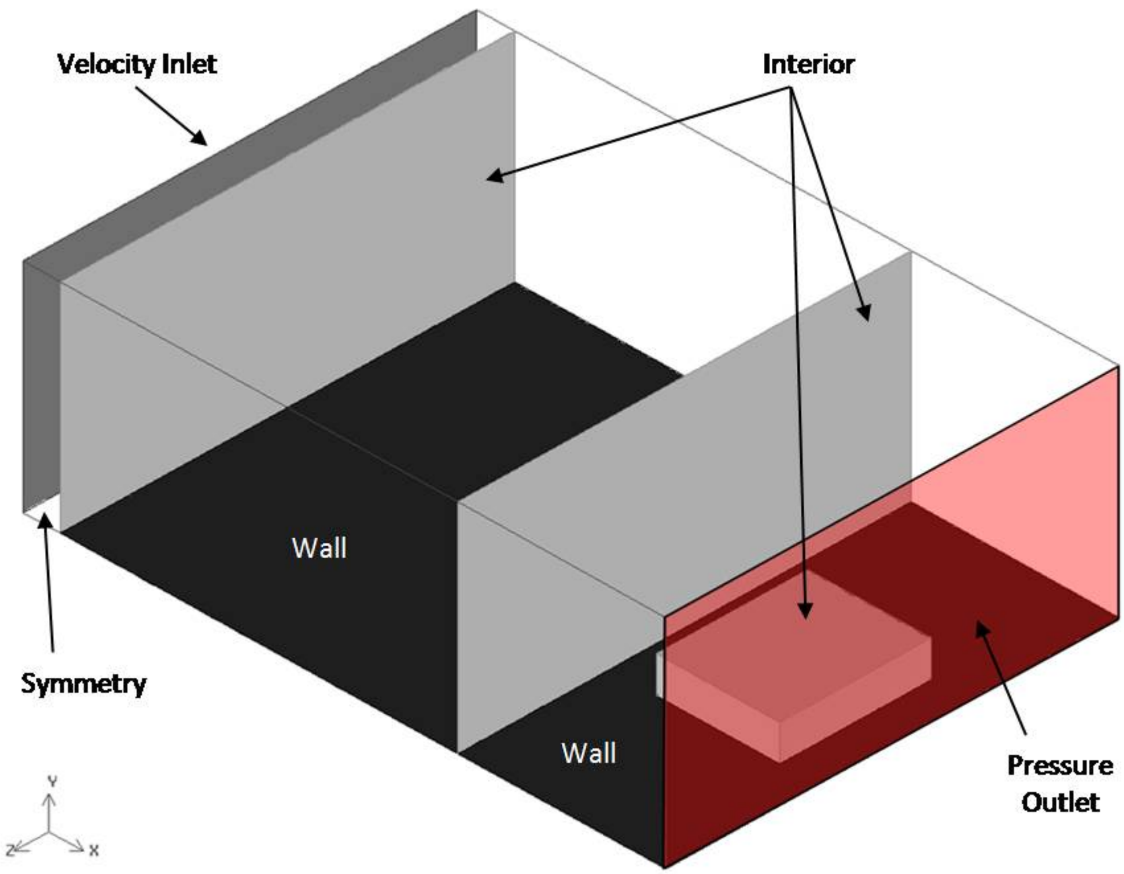

Figure 18: Model with Boundary Conditions

Solution Procedure

The simulations were conducted using finite volume discretization in a progressive method of modeling starting from inviscid flow with first-order upwind discretization to the turbulence model with second-order upwind discretization with double precision accuracy for the momentum, turbulent kinetic energy, and turbulent dissipation rate governing equations. Although the first-order upwind discretization may yield better convergence than the second order scheme, the results may be less accurate due to the meshed model containing a combination of both quad/hexagonal and triangular/tetrahedral elements. Thus, it is recommended to start with the first-order scheme and switch the second-order scheme after some iterations [37]. For the first 300 iterations, the inviscid, laminar, and turbulence model were used in sequential order for 100 iterations with first-order accuracy for each block of iterations. For the remaining iterations, the second-order upwind scheme was used.

The turbulence model is characterized by the Reynolds's Averaged Navier-Stokes (RANS) realizable k-ε model (RKE) for turbulence flow with standard wall equations in the FLUENT software package. The RKE model is an improvement over the standard k-ε model at simulating turbulent flow physics by satisfying the constraints of positive values for the normal stresses and Schwarz inequality for shear stresses. This results in more accurate predictions for the spreading rate of both planar and round jets and better simulation of flows involving rotation, boundary layers under strong adverse pressure gradients, separation, and recirculation [28].

The semi-implicit method for pressure-linked equations (SIMPLE) algorithm was used for pressure-velocity coupling with relaxation parameters of 0.3 for pressure, 0.7 for momentum, and 0.8 for turbulent kinetic energy. The finite volume (spatial) discretization was used with the least squares cell based method and second-order upwinding with double precision accuracy for the momentum, turbulent kinetic energy, and turbulent dissipation rate governing equations.

Computations

Simulations were performed on the following workstation: Hewlett-Packard/Compaq – Convertible Minitower dc7900 with INTEL ® CORE ™ 2-Quad Processor, Processor Speed 2.66 GHz and total memory – 3.49 GB. The computations were conducted with parallel processing, in which the mesh was decomposed into 4 subzones and distributed into the 4 processors of the parallel computing platform where Single Shared Memory (SHM) is used and the memory is shared between the processors on the single machine. The zones were portioned with the METIS software package that incorporates a multi-level approach in which the mesh is converted into a graph (where the element becomes a vertex on the graph) and partitioned the vertices and edges on the fine mesh are united to form a coarse mesh. The coarse mesh is partitioned and separated back to the original mesh. During the coarsening and uncoarsening, algorithms are applied to permit high-quality partions. Internode communication among the processors was established through the HP message passing interface (HP-MPI), which transferred information between the subzones [37].

Grid Independence & Convergence

Grid independence was explored by creating coarse and medium meshes of 4.27×10^5 and 7.70×10^5 nodes for the 15° orientation in GAMBIT. This was achieved by increasing the interval sizes of element control region by a factor of 0.125 and 0.250, respectively, for the outside edges in *I, J,* and *K*. The number of nodes on the top, bottom, and vertical edges of roughness elements was decreased to 96, 96, and 6, respectively, for the medium mesh and 48, 48, and 4, respectively, for the coarse mesh. Similarly, the interval sizes of the other regions were increased by a factor of 1.25 and 1.75, respectively, for all edges of the mesh. A summary of the node edge assignments for the coarse and medium grids are shown in Tables 2 and 3, respectively.

Table 2: Edge Node Assignments for Coarse Mesh

Region	*Edges*	*Ratio*	*Interval Size (Δ) cm*	*Edge Nodes*
Control Element	Top - *I* Top - *K*	1.00	0.508	40 33
	Bottom - *I* Bottom - *K*	1.00	0.381	53 43
	Vertical	1.07	0.254	20
	Roughness - *I, K* Roughness - *J*	1.00	N/A	1 4
Downstream	Top, Bottom - *I* Top, Bottom - *K*	1.00	0.762	80 37
	Vertical	1.05	0.635	48
Upstream	Top, Bottom - *K*	1.00	0.762	70
Inviscid	Top, Bottom - *I* Top, Bottom - *K*			80 7
	Vertical	1.05	0.635	48

Table 3: Edge Node Assignments for Medium Mesh

Region	*Edges*	*Ratio*	*Interval Size (Δ) cm*	*Edge Nodes*
Control Element	Top - *I* Top - *K*	1.00	0.44450	46 37
	Bottom - *I* Bottom - *K*	1.00	0.31750	64 52
	Vertical	1.07	0.20955	24
	Roughness - *I, K* Roughness - *J*	1.00	N/A	2 6
Downstream	Top, Bottom - *I* Top, Bottom - *K*	1.00	0.63500	96 44
	Vertical	1.05	0.50800	64
Upstream	Top, Bottom - *K*	1.00	0.63500	84
Inviscid	Top, Bottom - *I* Top, Bottom - *K*	1.00	0.63500	96 8
	Vertical	1.05	0.50800	64

The convergence criteria were based on the residuals of *u, v,* and *w* velocities, the turbulent kinetic energy, and the turbulent dissipation variables to reach to 1.0×10^{-6}. For some of the cases, the residuals plots display oscillating values before reaching residual values of 1.0×10^{-6}. For these cases, further iterations no longer yielded smaller residuals or improved the solution.

CHAPTER FIVE

Results & Discussion

The following section describes the experimental and numerical results and comparisons, the grid independence study, and an extended study of the experimental data regarding turbulence qualities and off-speed comparisons of the test coupons.

Experimental and Numerical Comparison

The comparison of experimental and numerical results was completed for the *u* and *w* velocities and flow angle at the freestream velocity of 10 m/s. It should also be noted that the frustums are aligned to the left side of the measurement plane (z/s = 0), as shown in Figure 19. Thus, for *w* velocity and the flow angle, a negative value indicates this is in the direction of the frustums' alignment.

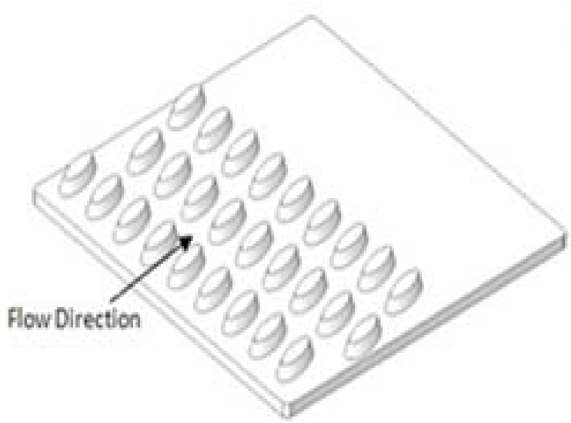

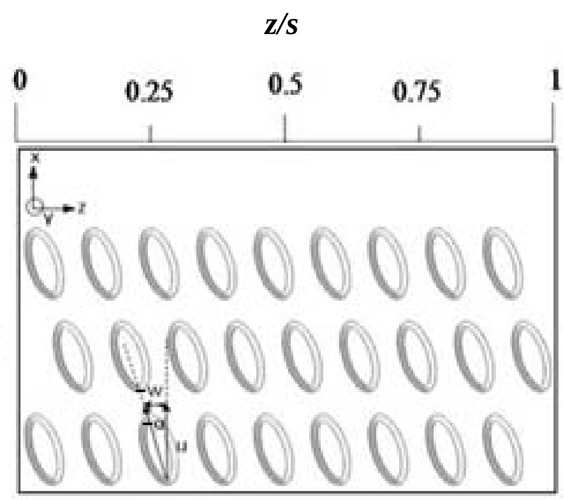

Figure 19: Test Coupon Orientation

u-Velocity

Figure 20 presents the velocity profiles of the test coupon with 15° aligned frustums in intervals of z/s = 0.25 for both numerical and experimental results. The *u* velocities demonstrate the difference in boundary layer height between the experimental and numerical study. The CFD results appear to display similar turbulent boundary layer profiles yet with a boundary layer height of approximately 1.8 cm across the span of the plate compared to the experimental boundary layer of roughly 5 cm. Furthermore, the simulated boundary layer at z/s = 1 demonstrates a more turbulent developed profile since the flow only comes into contact with one element and is not redirected as the rest of the test span for both sets of results. However, in the experimental results, the velocity profiles begin to coincide with each other at about the 2 cm height, while in the CFD simulations, the boundary layer heights vary between the rest of the plate and location z/s =1. Additionally, for the CFD profile at z/s = 0, the curve makes a sharp turn towards the other profiles at the approximate height of 0.2 cm.

The contour plots of the normalized *u* velocity (u/U_∞) for the experimental and numerical results in the downstream measurement plane are displayed in Figure 21. Additionally, the frustum heights are indicated by the dashed line and the experimental data was only taken above 0.404 cm. The experimental results demonstrate nearly uniform velocities across the span of the plate except at z/s = 1. The CFD results, however, appear to capture the effects of the aligned elements with the variation of velocities along the span as it propagates up to the boundary layer height. In both sets of data, the contours demonstrate that the directed flow does not disturb the right end of the test plate where the boundary layer development is shorter.

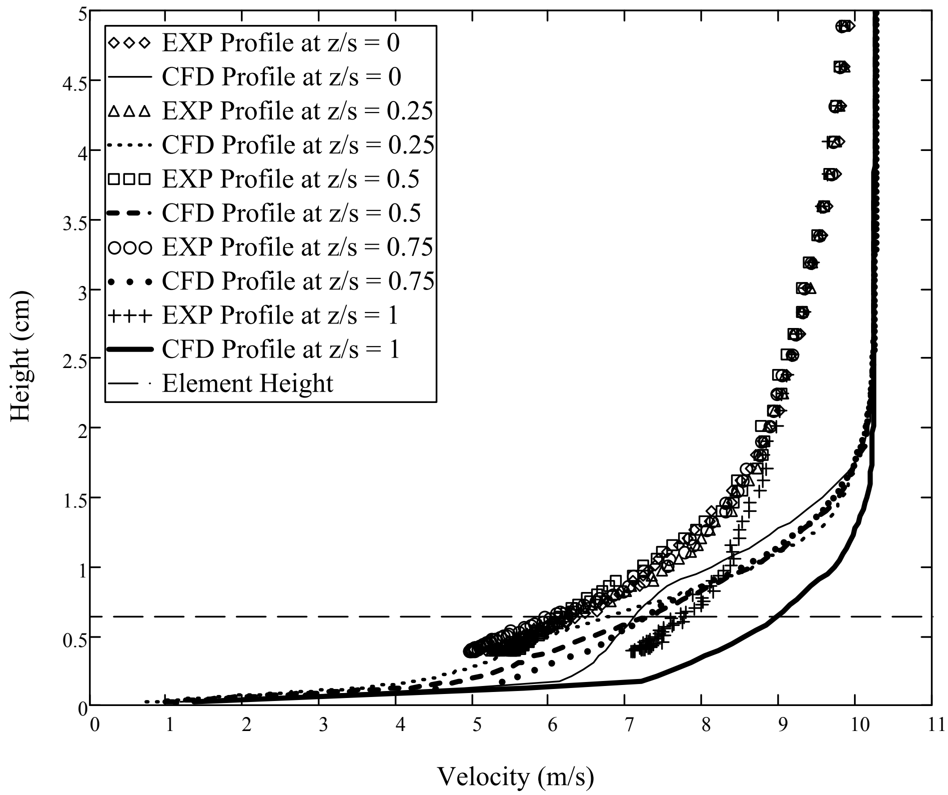

Figure 20: *u* Velocity Profiles for 15° Aligned Frustums

The trend of differences between the experimental and computational boundary layer heights and the decreasing boundary layer height at z/s = 1 can be seen in the other angle oriented test coupons in Figures. 22-24 for profile plots and Figures 25-27 for contour plots. Throughout the profile plots, the CFD results display changes in the curve for profiles below the element height as shown in Figures 22 and 23 for z/s = 0.75 and 0 for the 10° and 5° alignment, respectively.

In the CFD contour plots, the velocity differences across the span of the test plate characterized by fluctuations that indicate the flow paths created by the gaps between the arrays of elements. For the 0° orientation, it should be noted that the flow at the ends appear to show a smaller velocity gradient in Figure 27 since the flow created is not controlled or redirected as the middle span of the test plate.

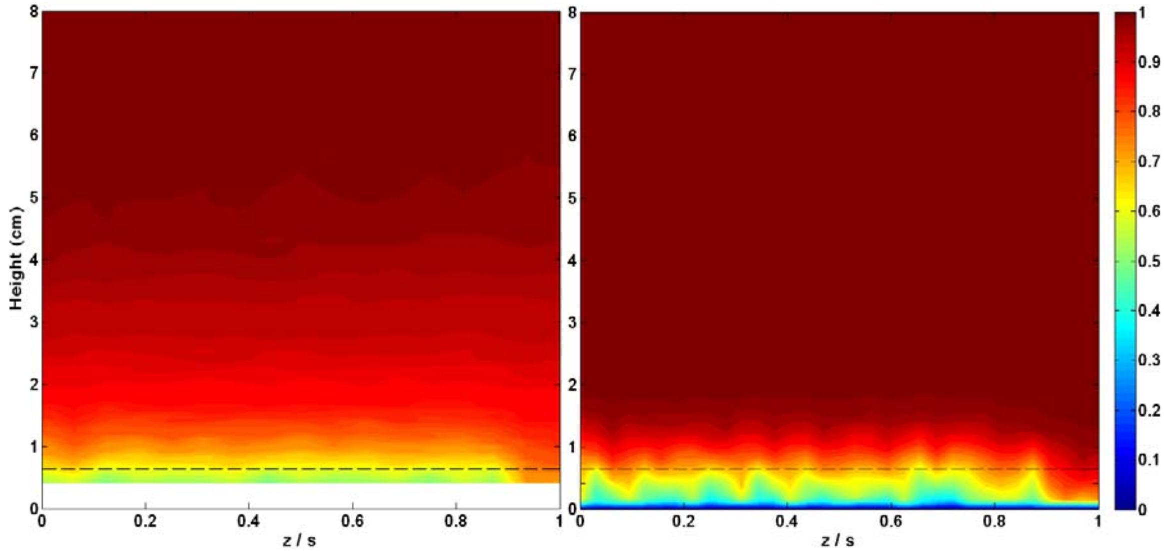

Figure 21: Normalized *u* Velocity Contour Plots for 15° Alignment: Experimental (left), Numerical (right)

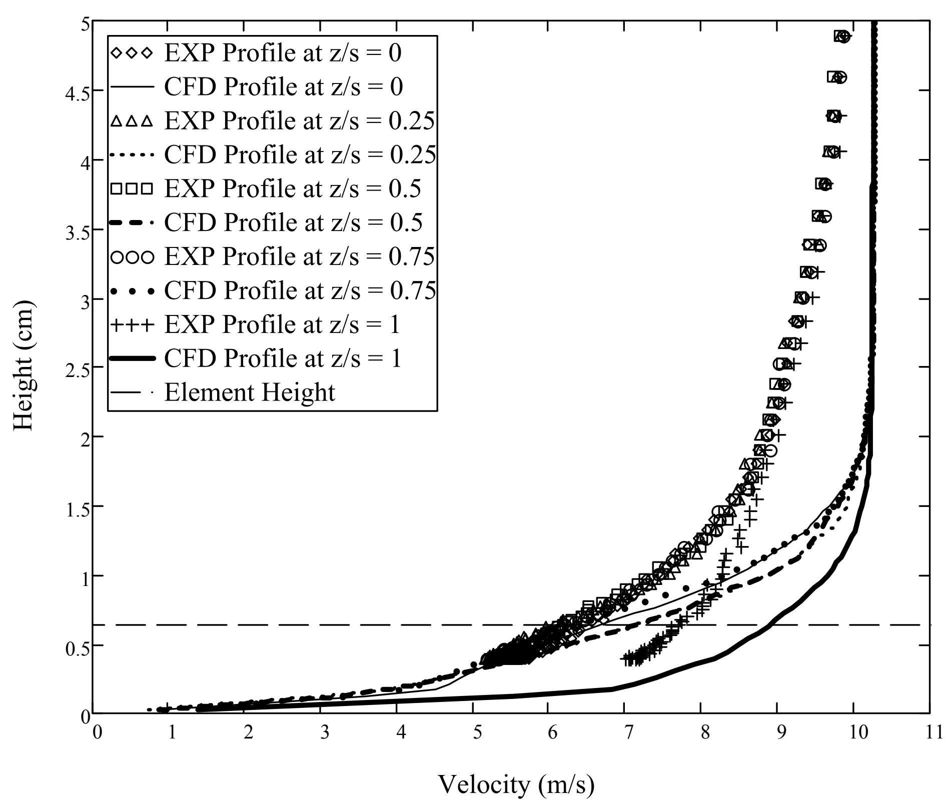

Figure 22: *u* Velocity Profile for 10°Aligned Frustums

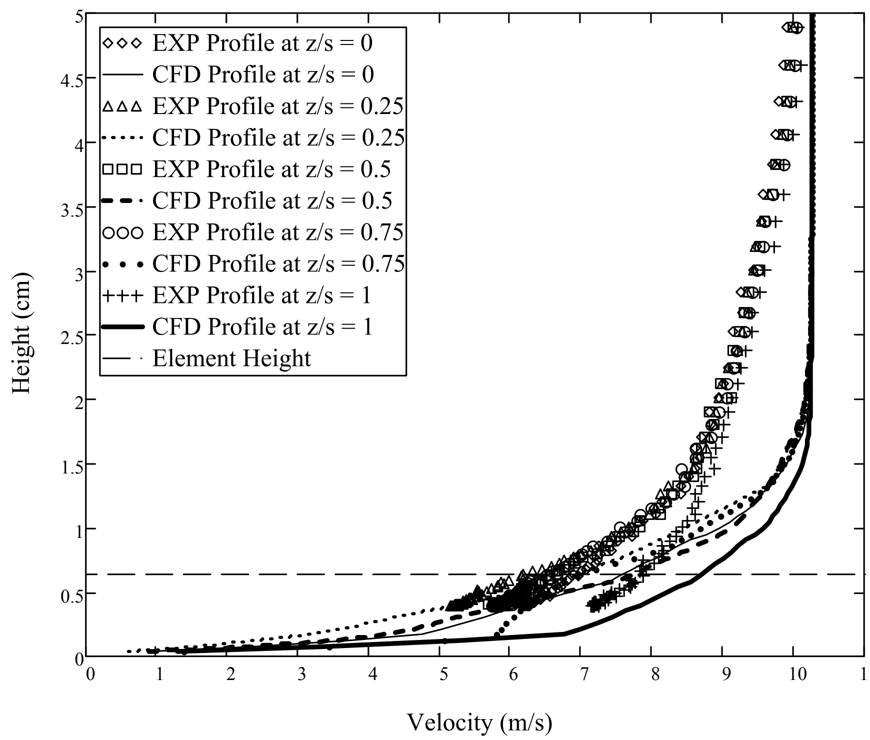

Figure 23: *u* Velocity Profile for 5°Aligned Frustums

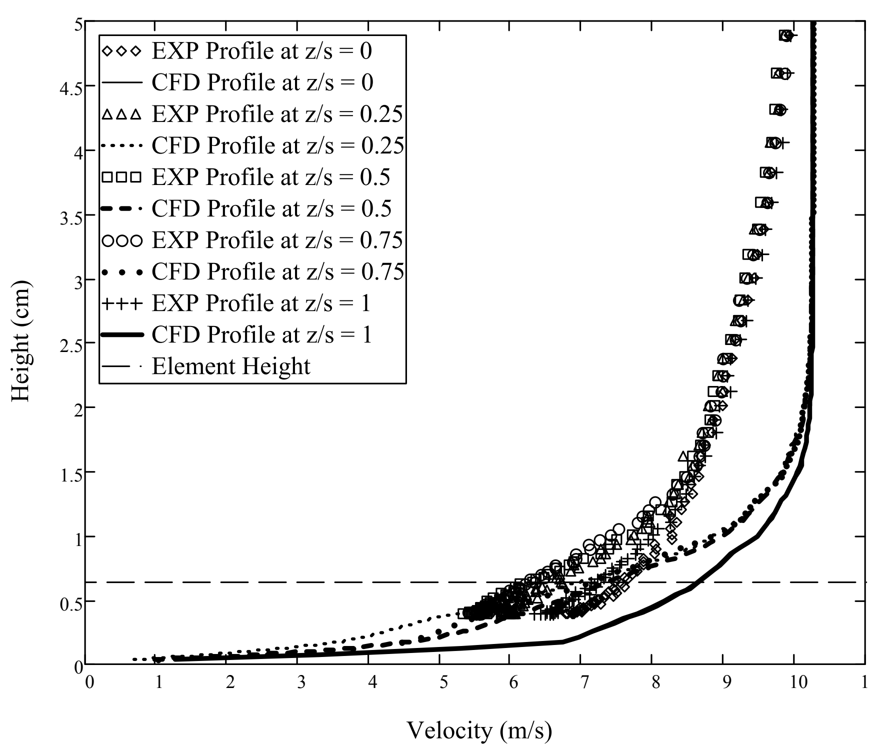

Figure 24: *u* Velocity Profiles for 0 ° Aligned Frustu

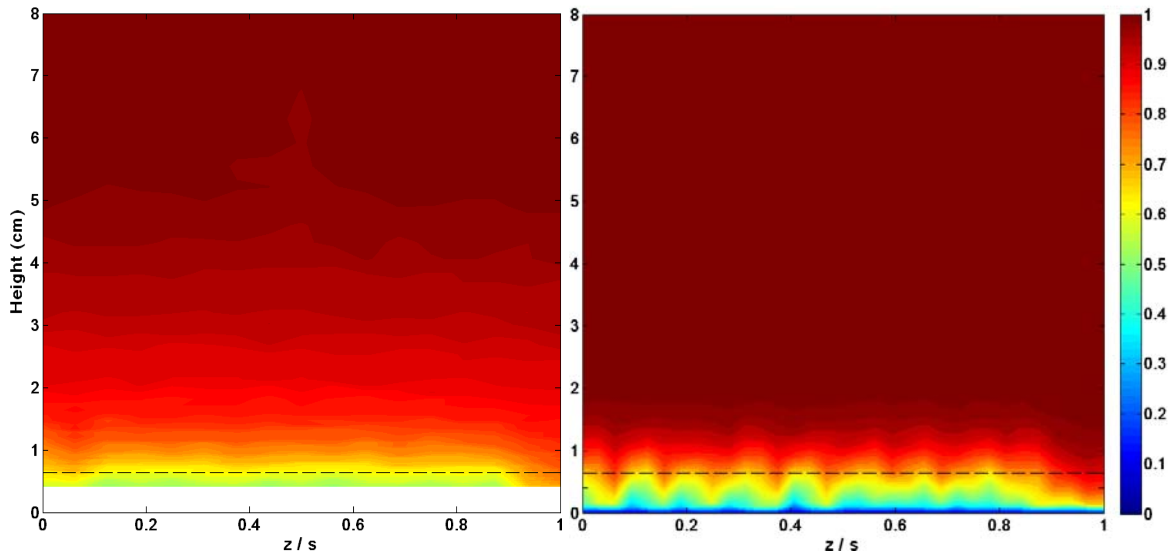

Figure 25: Normalized u Velocity Contour Plots for 10° Alignment: Experimental (left), Numerical (right)

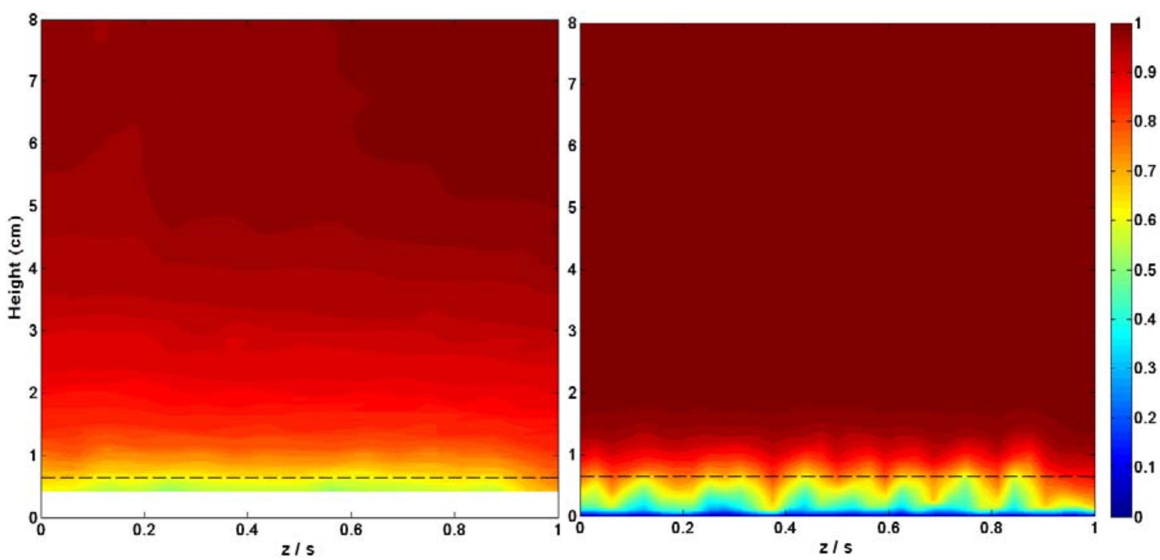

Figure 26: Normalized u Velocity Contour Plots for 5° Alignment: Experimental (left), Numerical (right)

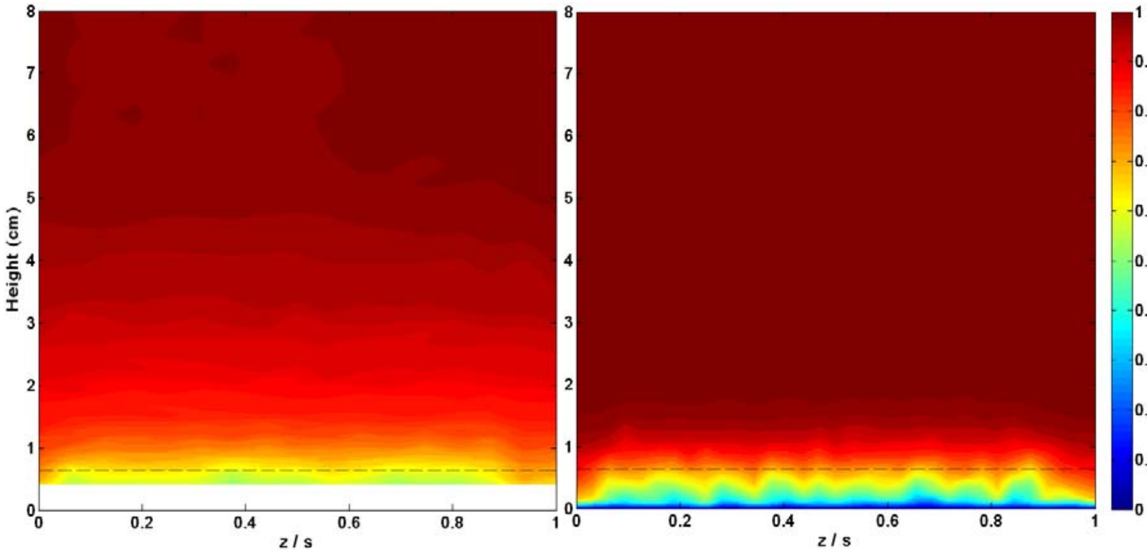

Figure 27: Normalized *u* Velocity Contour Plots for 0° Alignment: Experimental (left), Numerical (right)

Overall, the figures demonstrate that the viscous effects throughout the grid are not captured by the CFD model as shown with a lower boundary layer height in all the models. The profile centerlines of normalized *u* velocity for the experimental and computational results of all test coupons, including the baseline (No Elements), are shown in Figure 28.

The experimental and computational *u* velocities develop with the same shape despite the offset between them discussed earlier. There are slight differences in the boundary layer development among the test coupons starting from the height 0.5 cm to 1.5 cm. In the experimental results, the effect of the elements compared to the baseline results demonstrates that the flow is directed by the indication of lower velocities up to the height of 1.5 cm. Furthermore, with larger angle alignment, more flow is directed in the transverse direction and results in slower *u* velocities to the height 1.25 cm. The variation of velocities along the test span for the experimental results may not have been completely captured since measurements intervals were 1.27 cm or z/s = 0.0625.

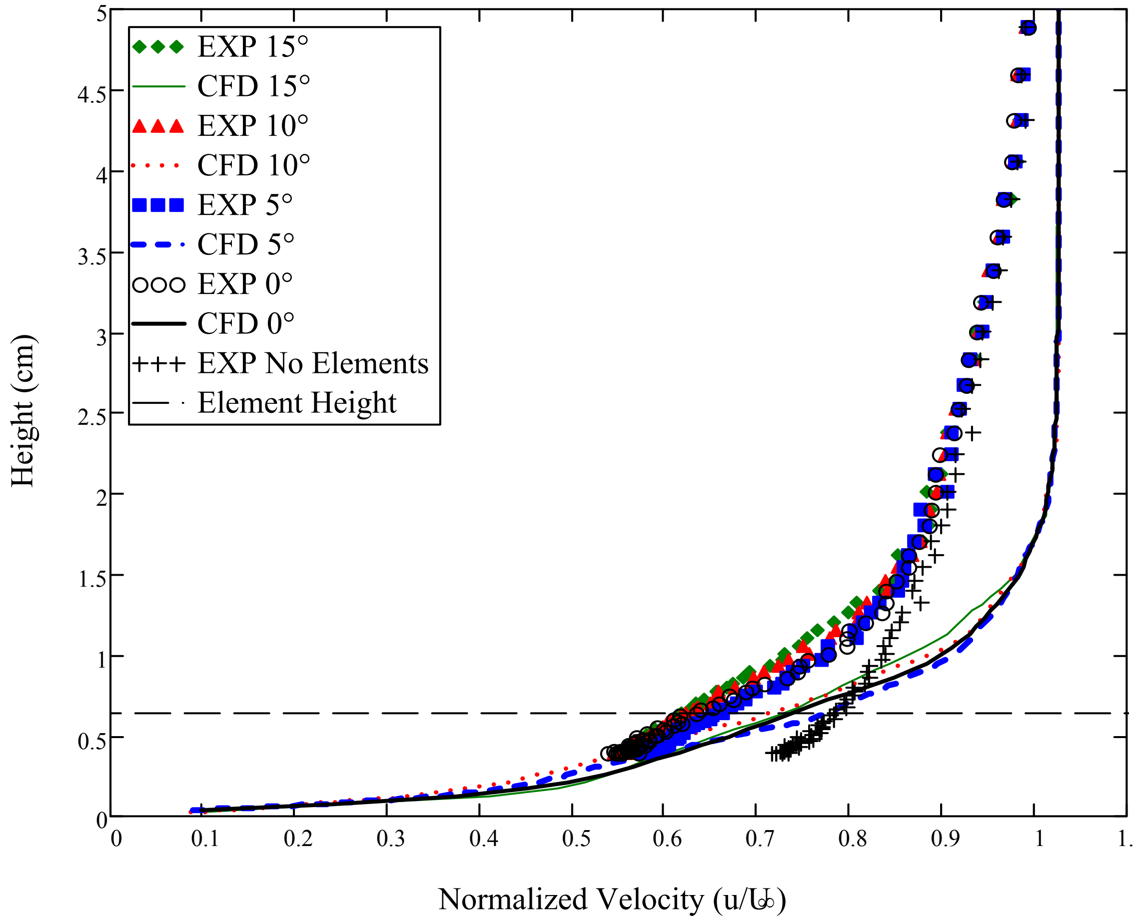

Figure 28: Overall Centerline Normalized u Velocity Profiles at $U_\infty = 10$ m/s

w-Velocity

The contour plots of the normalized w velocity (w/U_∞) are displayed within Figure 29 and demonstrate the edge effects of the aligned frustums. At z/s = 0 in the experimental results, there is a change in direction and magnitude of flow above a height of 1 cm due to the recirculation of flow back to the freestream. The simulations show similar contours yet with less strength in the magnitude of flow.

Throughout the span, the traverse boundary layers of both studies are similar with some fluctuations along the test plate corresponding to the elements. Towards the right end of the test coupon (z/s = 1), the velocity slows down from the absence of the directed flow, but the velocity does reach w = 0 m/s at approximately 7 cm and 6 cm for the experimental and numerical results, respectively.

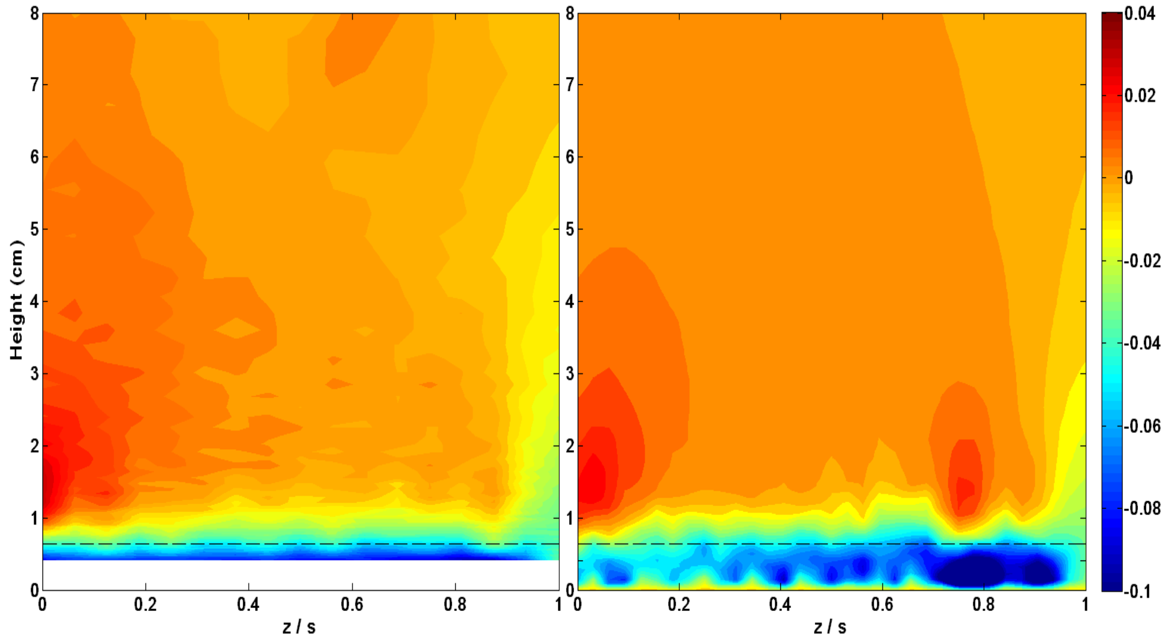

Figure 29: Normalized w Velocity Contour Plots for 15° Alignment: Experimental (left), Numerical (right)

The w velocity profiles in Figure 30 better demonstrate the differences between the experimental and computational results. Overall, the velocity profiles compare well to each other with the ends of the plate showing the largest differential velocities between sets of results. Specifically, at z/s = 0, a flow reversal occurs as the directed flow begins to realign back with the freestream flow at the approximate height of 1.25 cm with a differential velocity equal to 0.1 m/s for both experimental and computational results.

At z/s = 1, the difference in velocities is about the same throughout the profile, but the CFD results realign back with the freestream flow at a lower boundary layer height. Throughout the center of the span, values from both sets agree reasonably well.

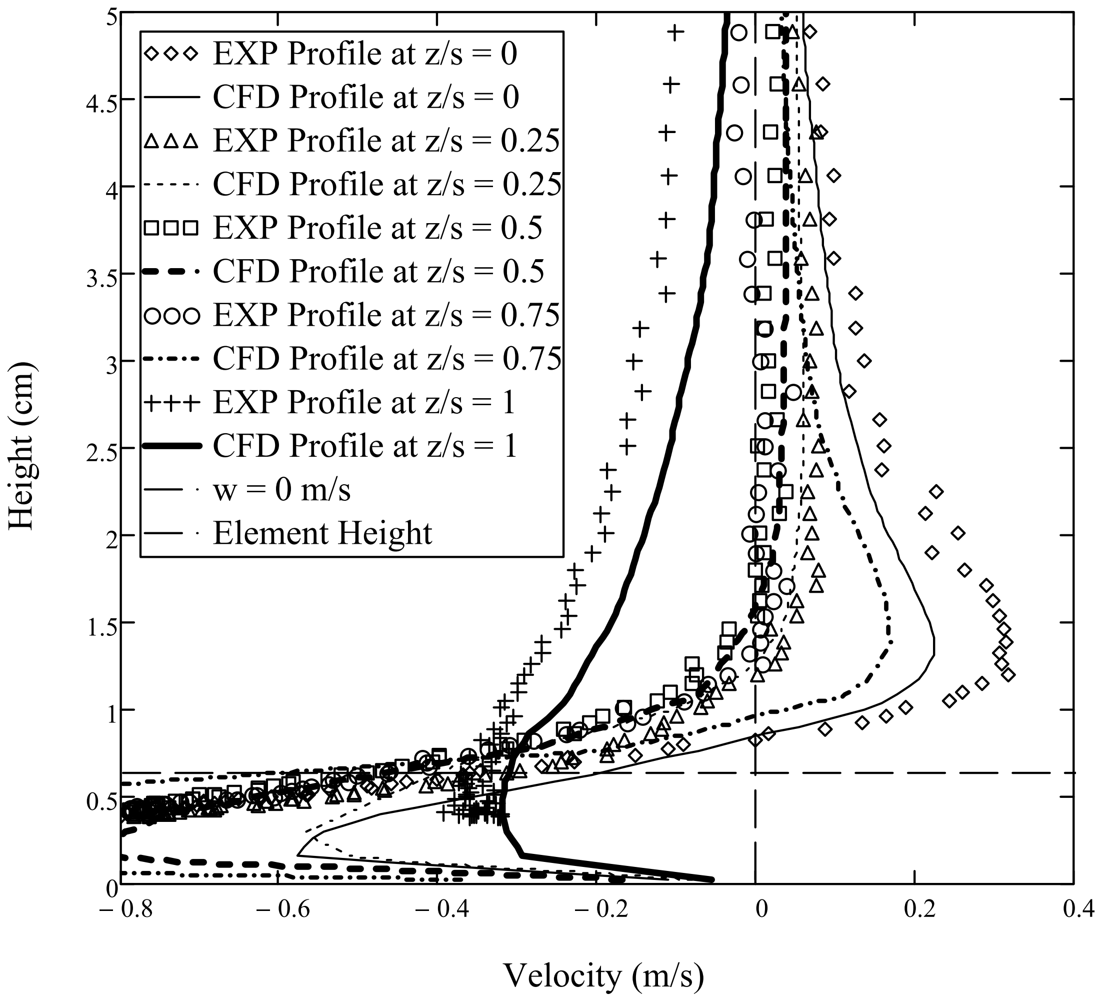

Figure 30: *w* Velocity Profiles for 15° Aligned Frustums

At z/s = 0.75, the CFD simulations demonstrate the reversal of flow similar to the one from z/s = 0, yet this is far from the experimental values. Truncated on the profile plot, the numerical method also predicts the highest *w* velocity (-1.8 m/s) to occur at the approximate height of 0.25 cm for profile z/s = 0.75.

Additionally, the contour plots of the other angle alignments are displayed in Figure 31-33, and the profile plots are shown in Figures 34-36. At the ends of the test plates, the *w* velocities still have opposite directions, yet at z/s = 0, the magnitude decreases with the decrease of the elements' alignment angle. Furthermore, with the decrease in alignment angle, the *w* velocities below the 1 cm height diminish across the span for both experimental and computational results. Both sets of results show flow pathways from the arrays of elements, however, the CFD simulations demonstrate sharper inclines and declines of velocities along the test plate.

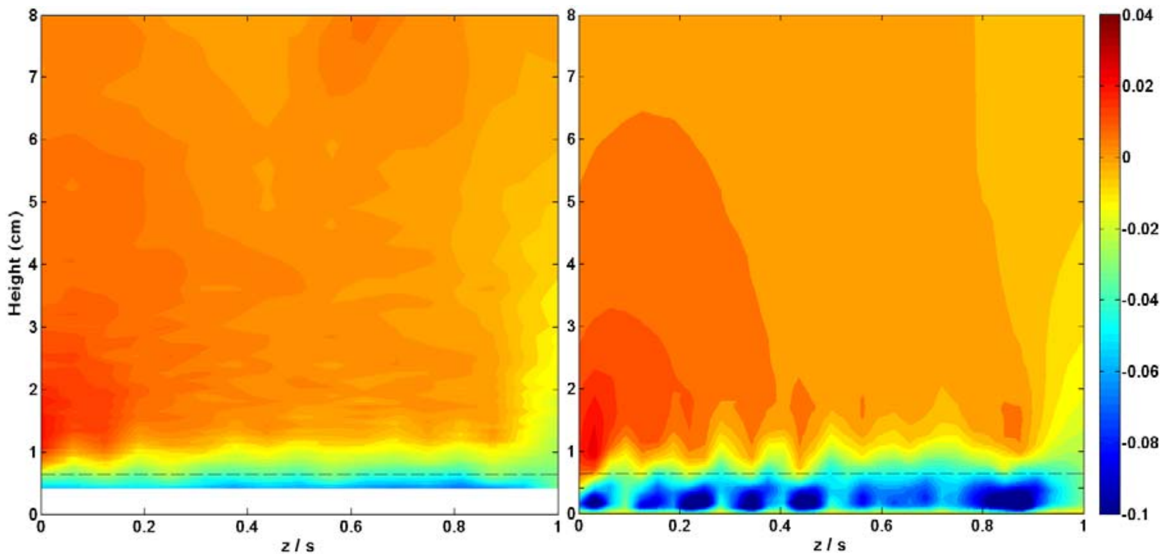

Figure 31: Normalized *w* Velocity Contour Plots for 10° Alignment: Experimental (left), Numerical (right)

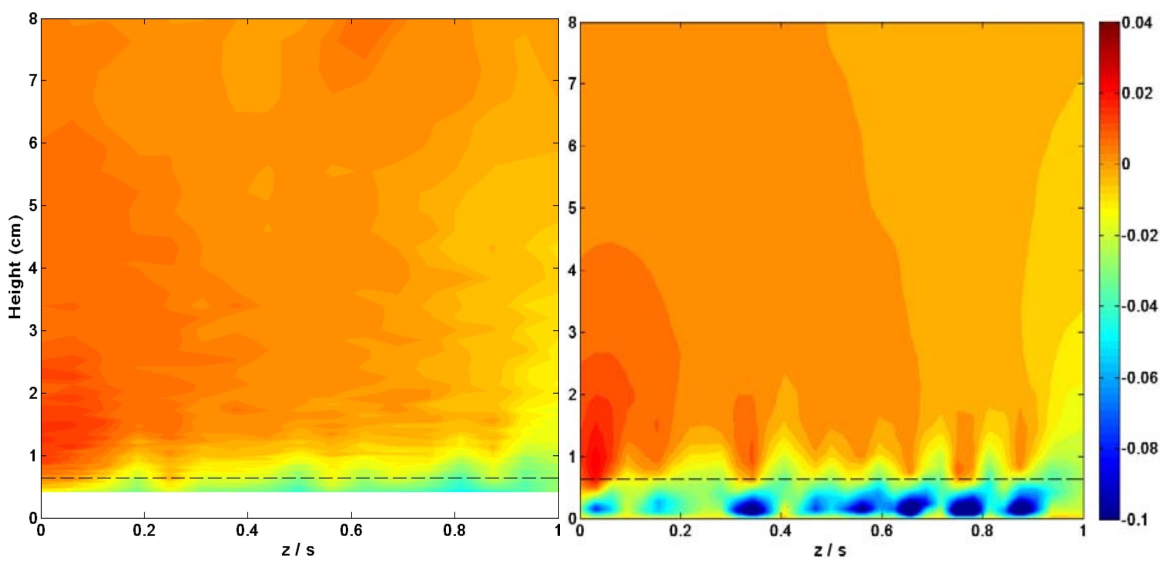

Figure 32: Normalized *w* Velocity Contour Plots for 5° Alignment: Experimental (left), Numerical (right)

The contour plots in Figure 33 are displayed on a smaller scale to give a better perspective of values between the experimental and computational data. From both sets of results, there are symmetrically opposite velocities starting from the center that increase as they traverse to the ends of the plates. Again, the CFD simulations display higher magnitudes of velocities reaching $w = \underline{+}0.5$ m/s below the element height for the z/s = 0.25 and 0.75 shown in the profile plot in Figure 34. Also, computational results for the profile plots with 0° and 5° frustum alignment match the experimental data well above the element height. The 10° orientation shows a similar match, but the centerline profile is slightly higher until the approximate height of 1.5 cm.

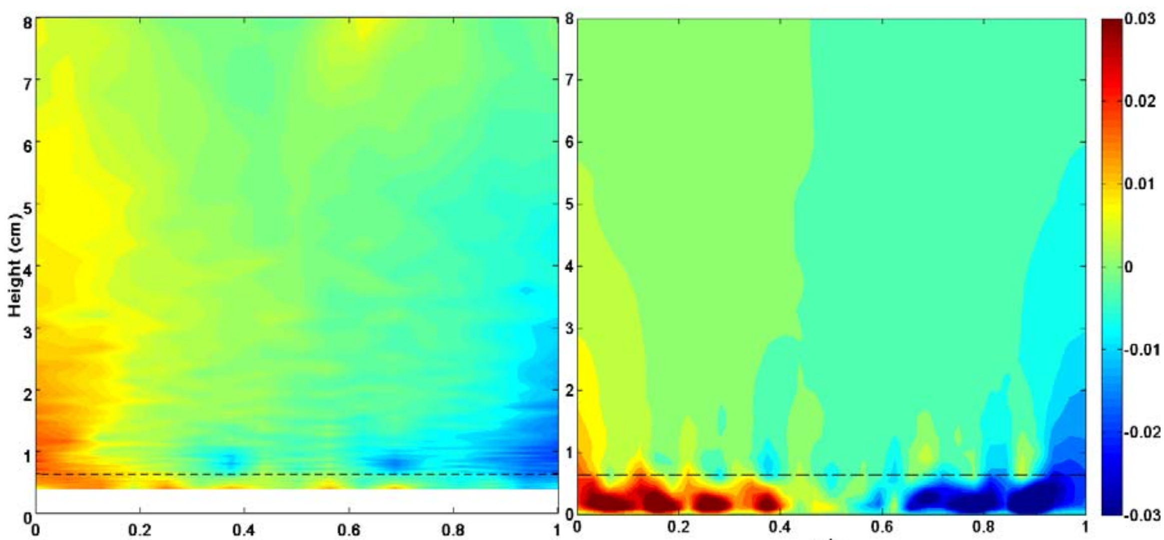

Figure 33: Normalized *w* Velocity Contour Plots for 0° Alignment: Experimental (left), Numerical (right)

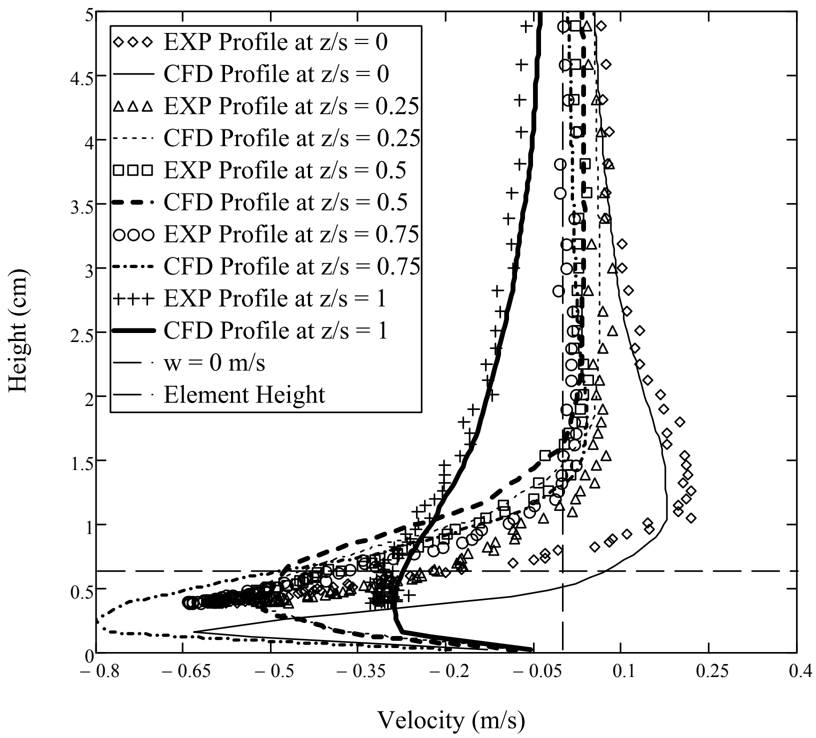

Figure 34: *w* Velocity Profiles for 10° Aligned Frustums

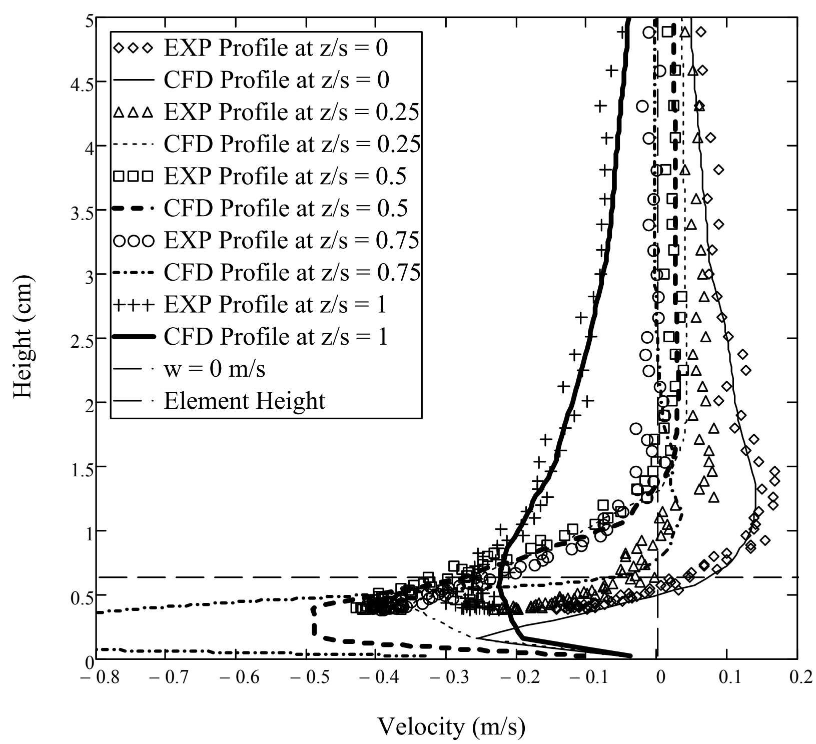

Figure 35: *w* Velocity Profiles for 5° Aligned Frustums

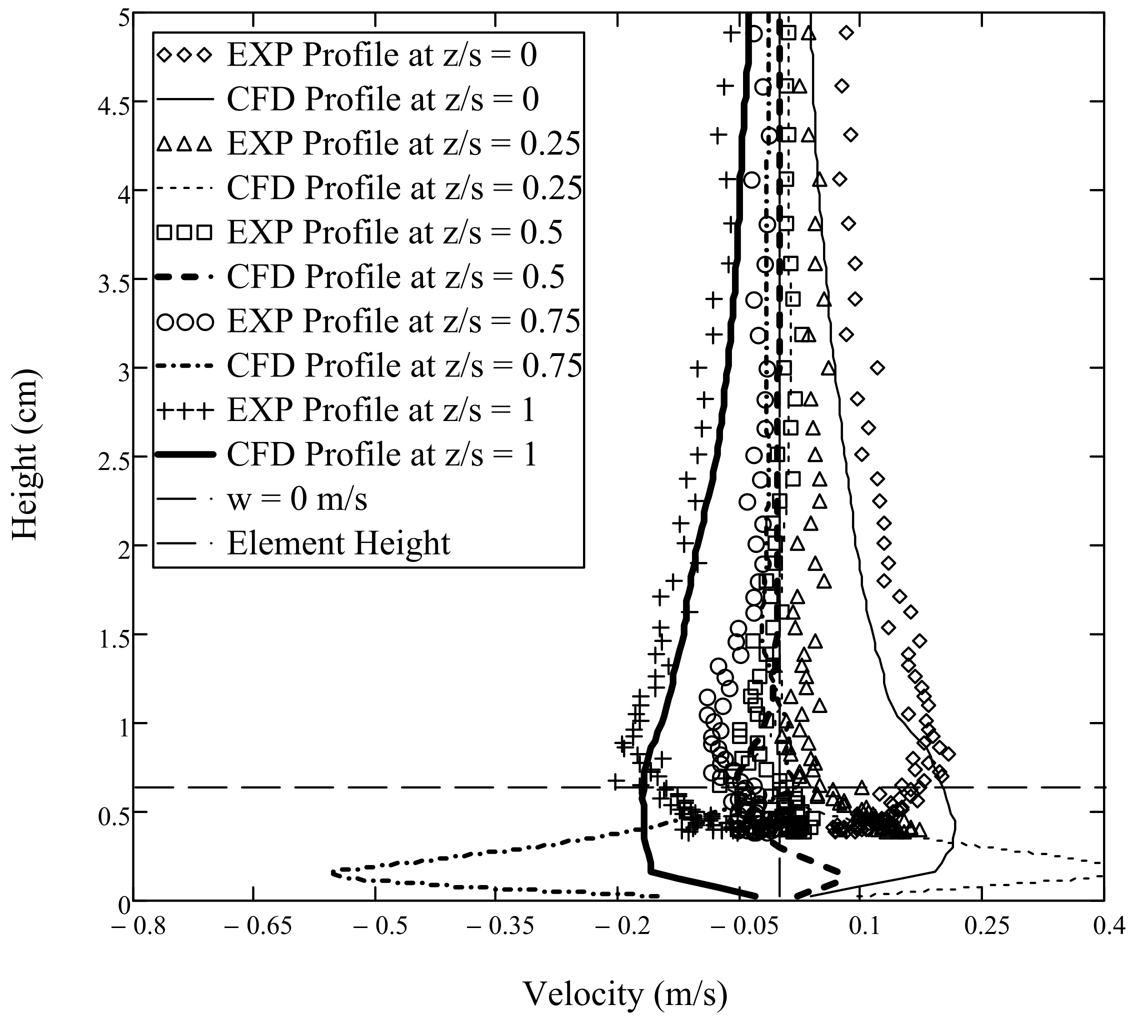

Figure 36: *w* Velocity Profiles for 0° Aligned Frustums

The overall centerline comparison for the experimental and computational *w* velocities of all the test coupons is shown in Figure 37. The CFD values for all orientations, except for 10°, match well with the experimental results especially below the element height. Furthermore, the experimental *w* velocities with respect to the elements orientation remain distinct up to the approximate height of 1 cm, where the results appear to converge to similar velocities. However, the computational *w* velocities do not converge until 1.5 cm in height, due mainly to the 10° centerline profile that appears to be offset above the experimental result.

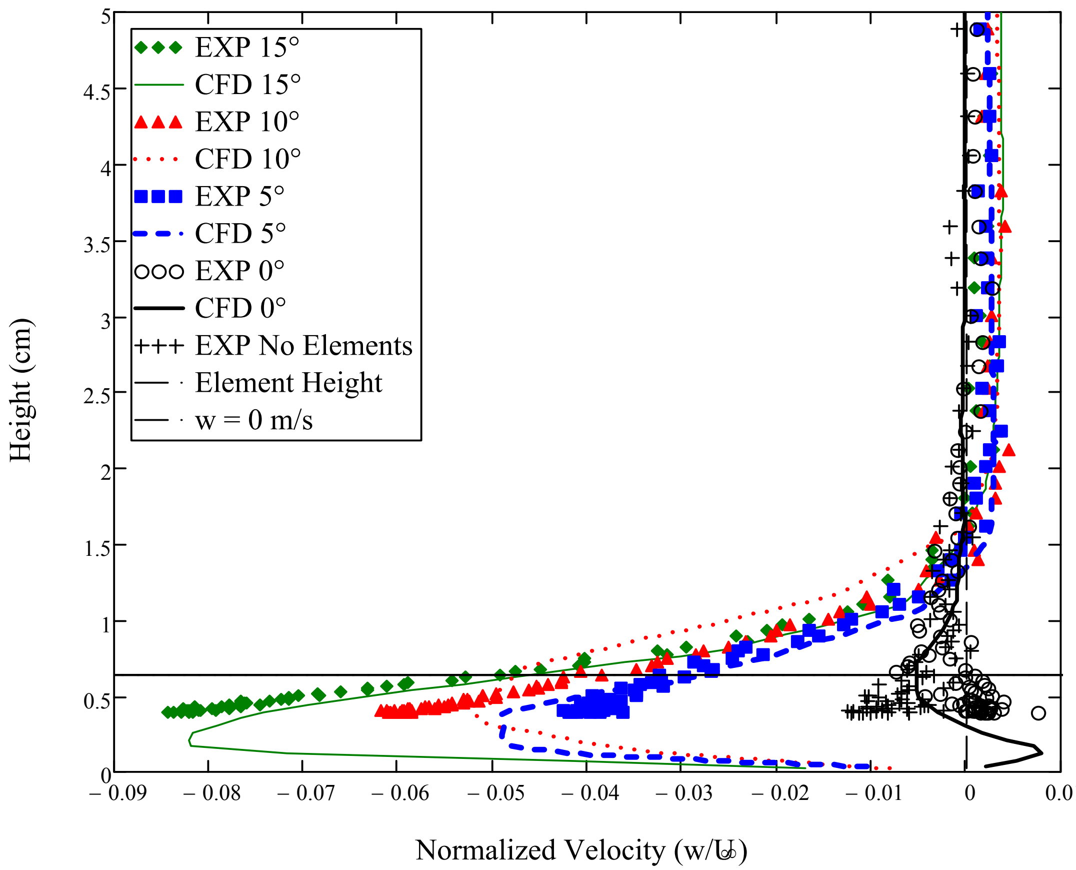

Figure 37: Overall Centerline Normalized *w* Velocity Profiles at $U_\infty = 10$ m/s

Flow Angle

The flow angle contour plots for the 15° test coupon orientation, shown in Figure 38, are very similar to those of the *w* velocity including the end effects from the flow reversal at z/s = 0 and z/s = 1. In the experimental results, the flow angle increases slightly in the direction of the elements' alignment across the test span as it approaches z/s = 0.9 at the element height. The CFD predictions display this behavior and also display gaps of increased flow angle that may be due to the location of the elements. Additionally, at location z/s = 0.75, the flow angle exceeds -14° below the element height and a second flow reversal from the approximate height range of 1.2 -2.2 cm, as shown in the *w* velocity contour plot.

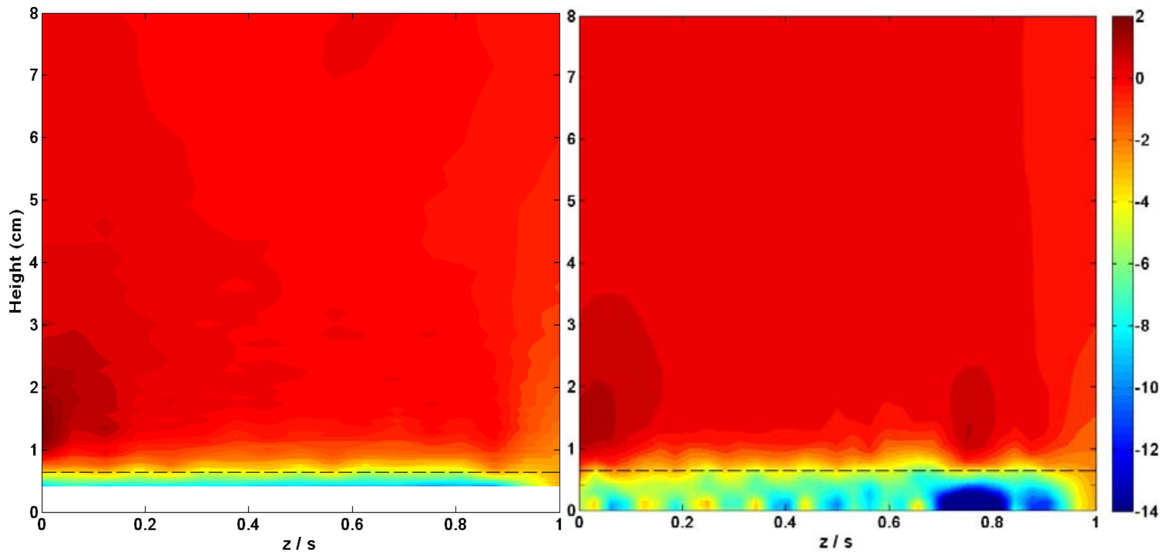

Figure 38: Flow Angle α Contour Plots for 15° Alignment: Experimental (left), Numerical (right)

Shown in Figure 39, the height where the flow realigns with the freestream (1 cm) is approximately the same through the span of the test plate, and the profiles have a similar shape for both experimental and computational studies. The CFD results agree best with the experimental data for the z/s = 0.25 and centerline profiles below element height. Once again, the CFD prediction values at the ends of the plate are smaller as profiles stay within the bounds of the experimental profiles

The contour and profile plots for the 10°, 5°, and 0° frustum alignment are displayed in Figures 41-43 and Figures 44-46, respectively. As expected, the same trends and features from the *w* velocity results carry through the contour plots, including the decrease in flow angle with respect to the decrease in the elements' alignment and the flow reversal that occurs toward the location z/s = 0. Furthermore, the contour plots for the 0° degree alignment are displayed on a smaller scale to demonstrate the symmetry of the flow angle throughout the span.

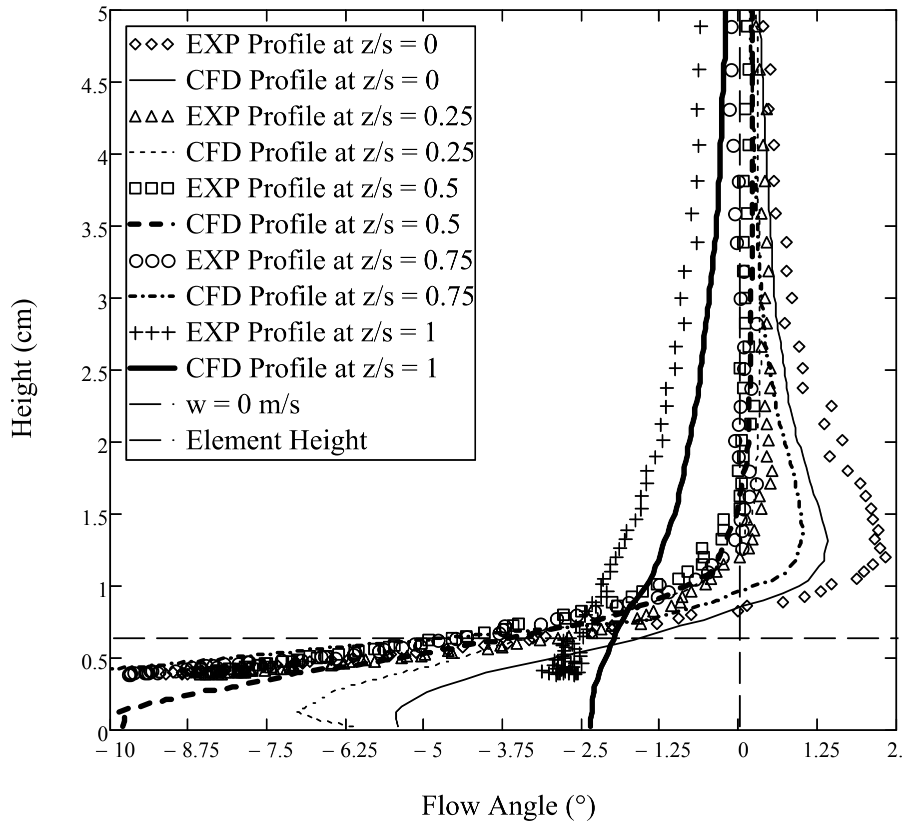

Figure 39: Flow Angle α Profiles for 15° Aligned Frustums

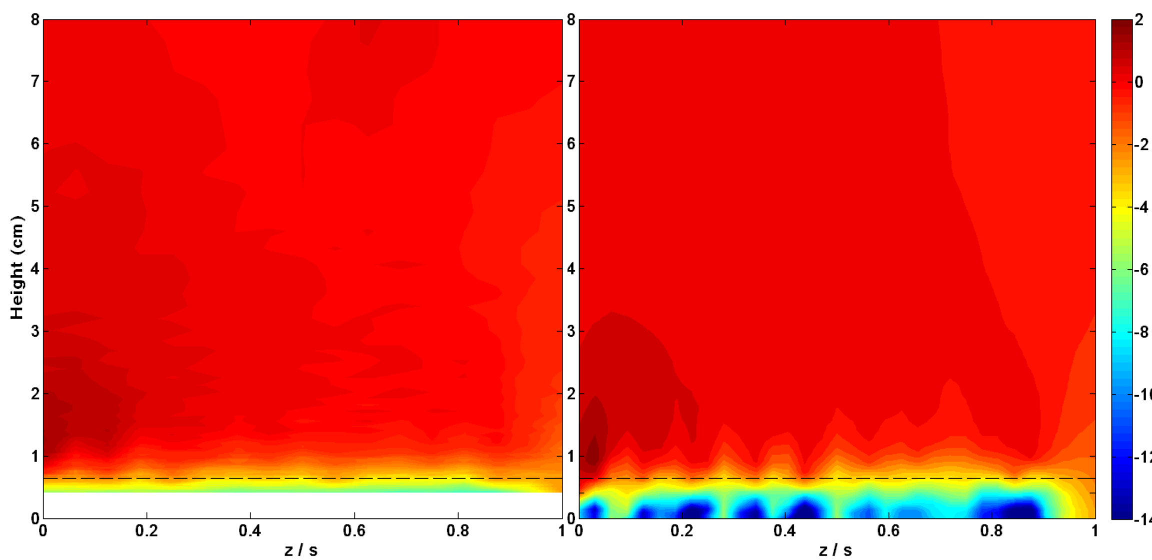

Figure 40: Flow Angle α Contour Plots for 10° Alignment: Experimental (left), Numerical (right)

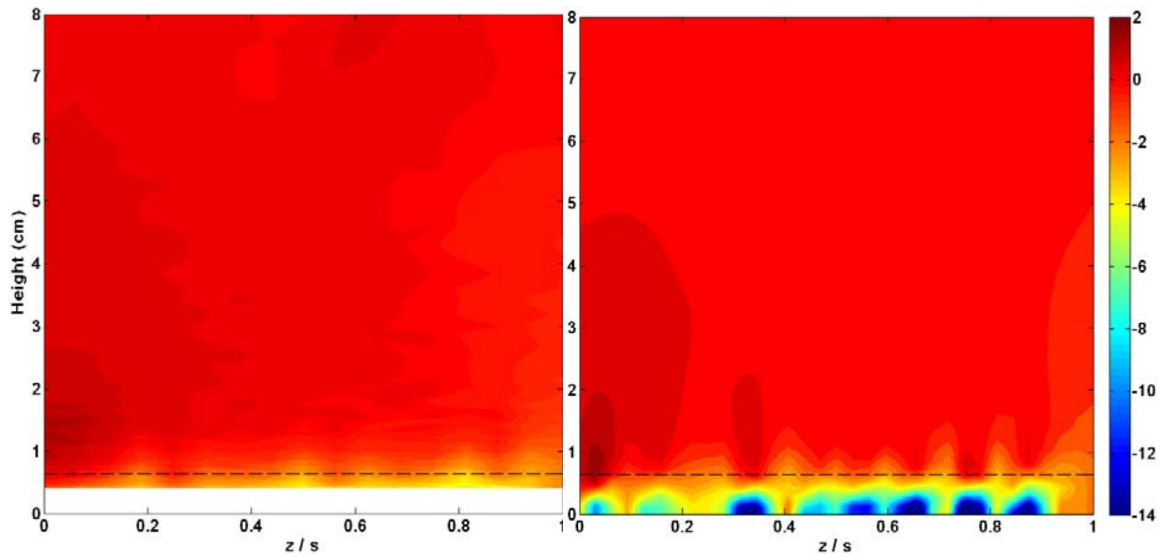

Figure 41: Flow Angle α Contour Plots for 5° Alignment: Experimental (left), Numerical (right)

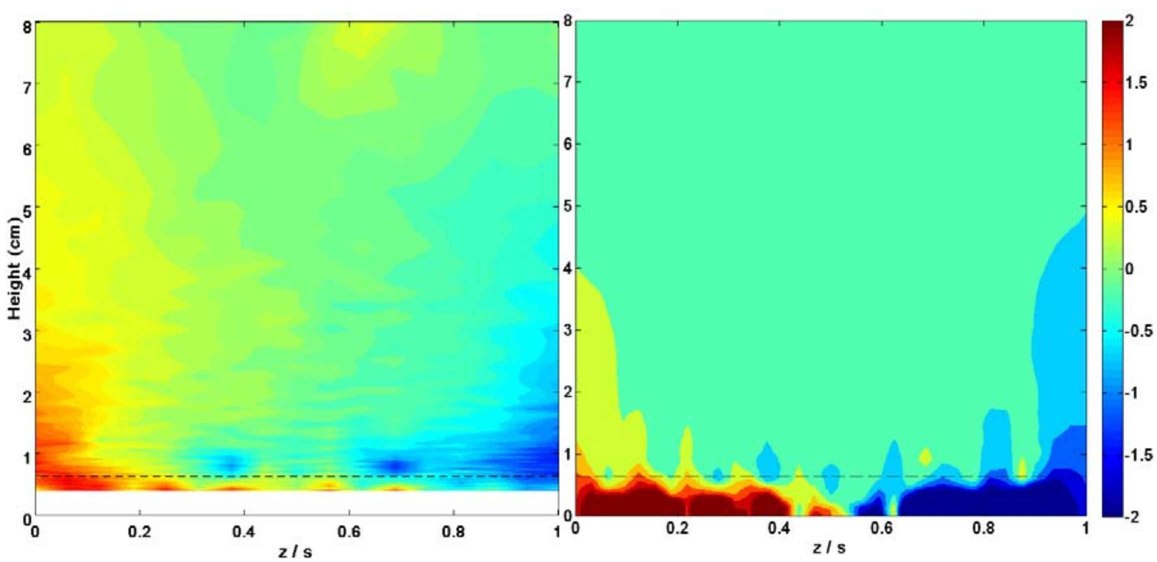

Figure 42: Flow Angle α Contour Plots for 0° Alignment: Experimental (left), Numerical (right)

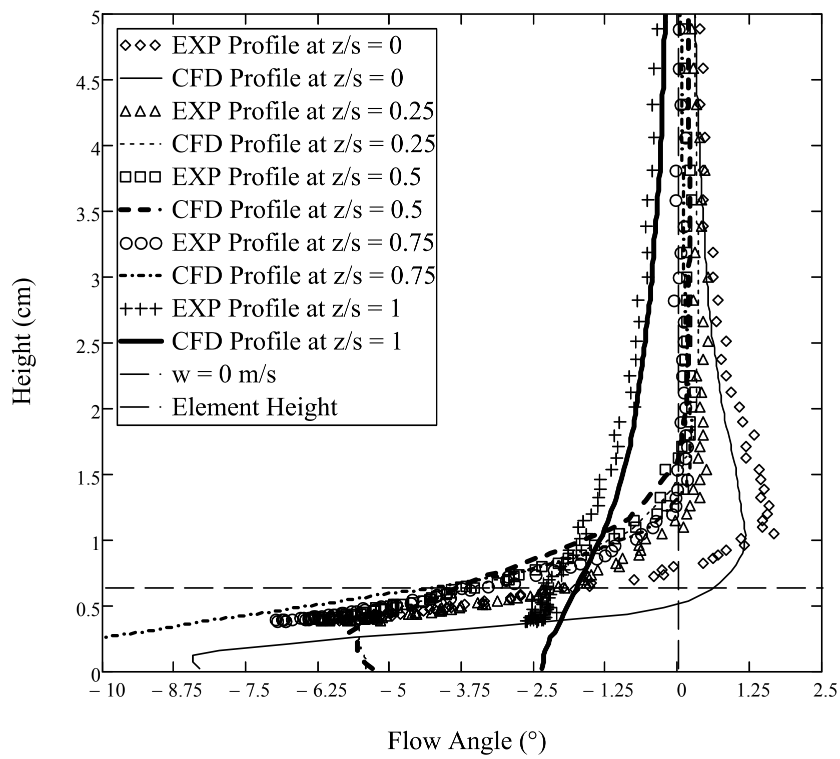

Figure 43: Flow Angle α Profiles for 10° Aligned Frustums

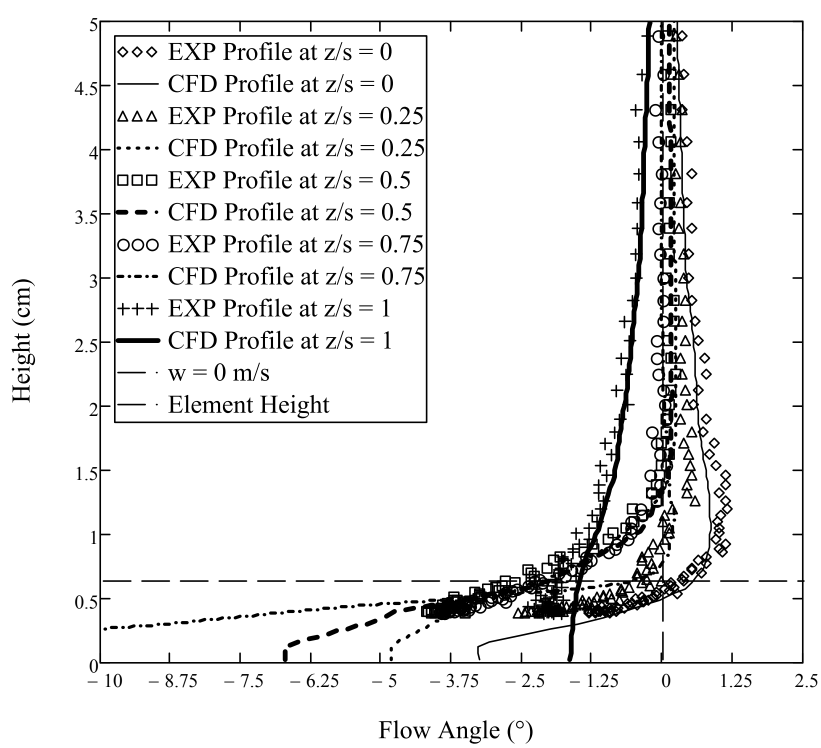

Figure 44: Flow Angle α Profiles for 5° Aligned Frustums

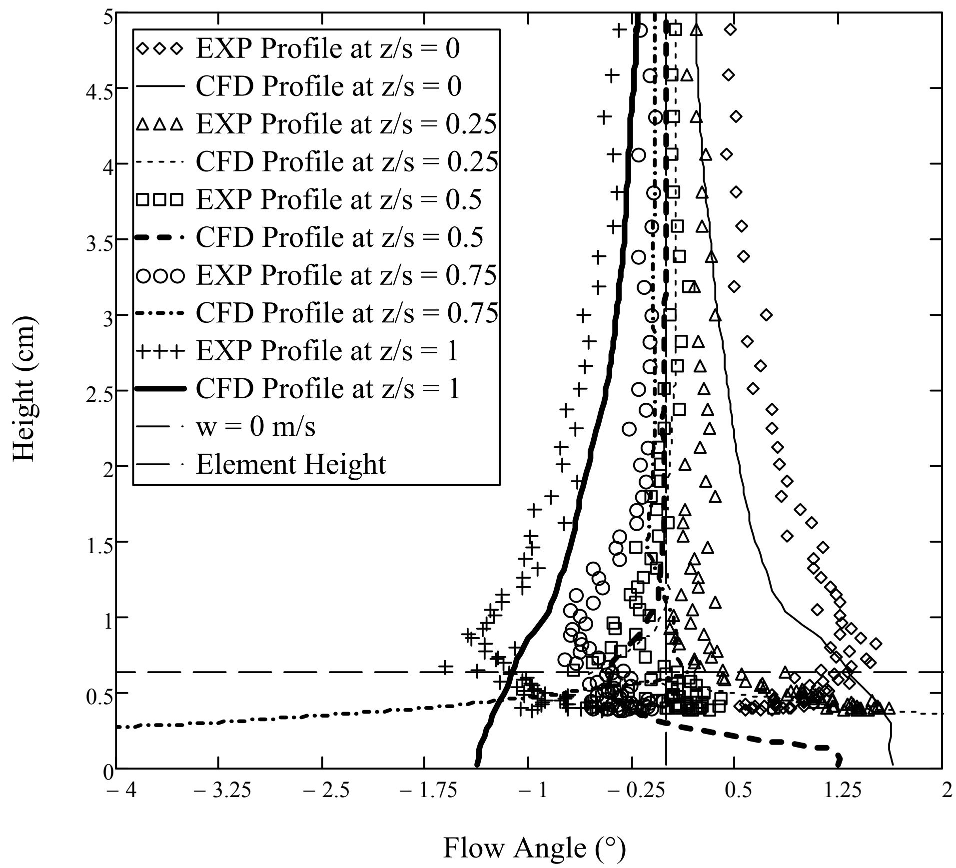

Figure 45: Flow Angle α Profiles for 0° Aligned Frustums

The overall centerline comparison of the test coupons for experimental and numerical results of the flow angle are displayed in Figure 46. The computational results have reasonable agreement with experimental results with differences of 1-2° for the flow angle at the same height up to 1.5 cm. At the lowest experimental measurement height, the flow angles among the 15°, 10°, and 5° cases vary by approximately 2.5° of each other, and at the element height, the difference decreases to approximately 1°. The CFD results follow the same trend with smaller differences, including a flow angle difference of 3° between 15° and 5° frustum orientations. However, upon reaching element height, the computational predictions of flow for the 10° case surpasses the 15° case by about 1° until about 1.75 cm height.

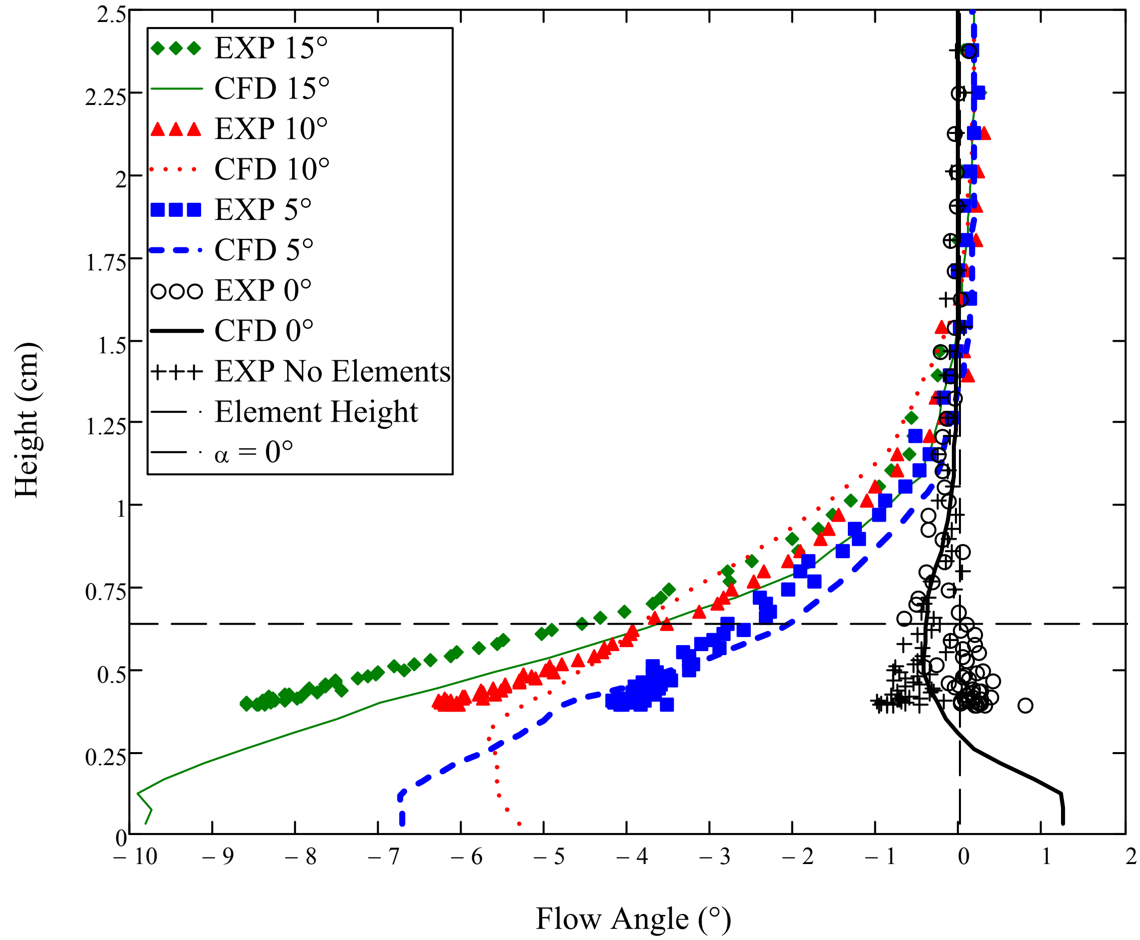

Figure 46: Overall Flow Angle α Profiles at $U_\infty = 10$ m/s

Grid Independence Study

The test for grid independence was conducted for the 15° frustum orientation model consisting of different node counts and compared on the basis of u and w velocities and the flow angle. Additionally, the residuals and computational time are displayed for each of the different mesh sizes.

For the u velocity, the profile plot shown in Figure 47 compares the data at the ends and centerline of the test coupon and displays some agreement between the models. The fine and medium mesh models are more in agreement with each other throughout the profiles at the given locations.

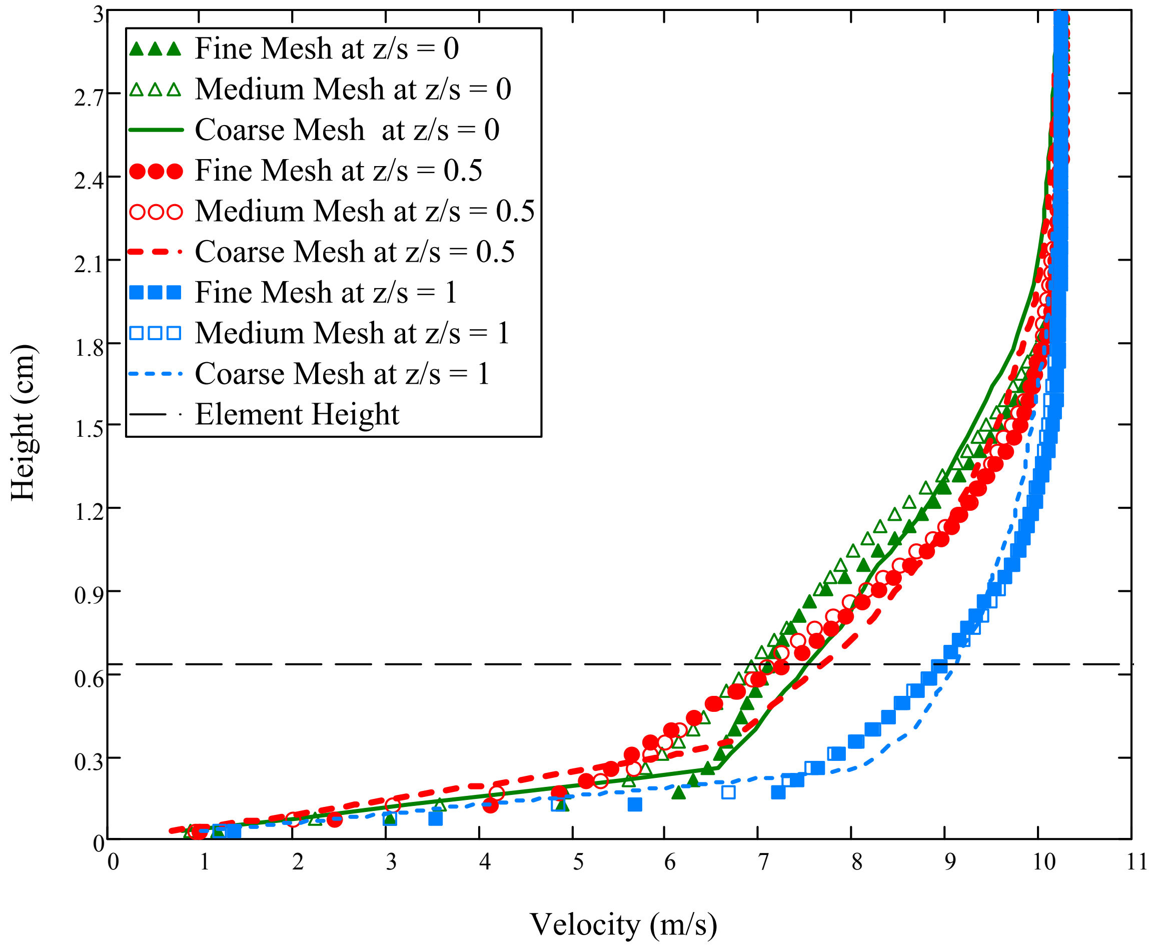

Figure 47: *u* Velocity Profiles for Grid Independence

However, in the contour plots displayed in Figure 48, the coarse model displays a slightly larger boundary layer height and does not exhibit the same fluctuations and gaps of velocity magnitudes across below the element height across the test span than the fine and medium mesh models. Furthermore, these fluctuations are less uniform in the medium mesh than the fine mesh.

The profile plot comparing the *w* velocities for the meshes, displayed in Figure 49, demonstrates that the profiles of the different meshes have similar shapes and coincide at certain heights and profiles. As expected, the profiles at z/s = 1 collapse together while at z/s = 0, the medium and coarse mesh profiles match well, though these values are smaller than the fine mesh profile values, which are closer to the experimental results. The different velocities from the meshes at centerline profile appear to be offset from each other, with the coarse mesh having the lowest values above element height and the fine mesh profile as the best approximation to the experimental values.

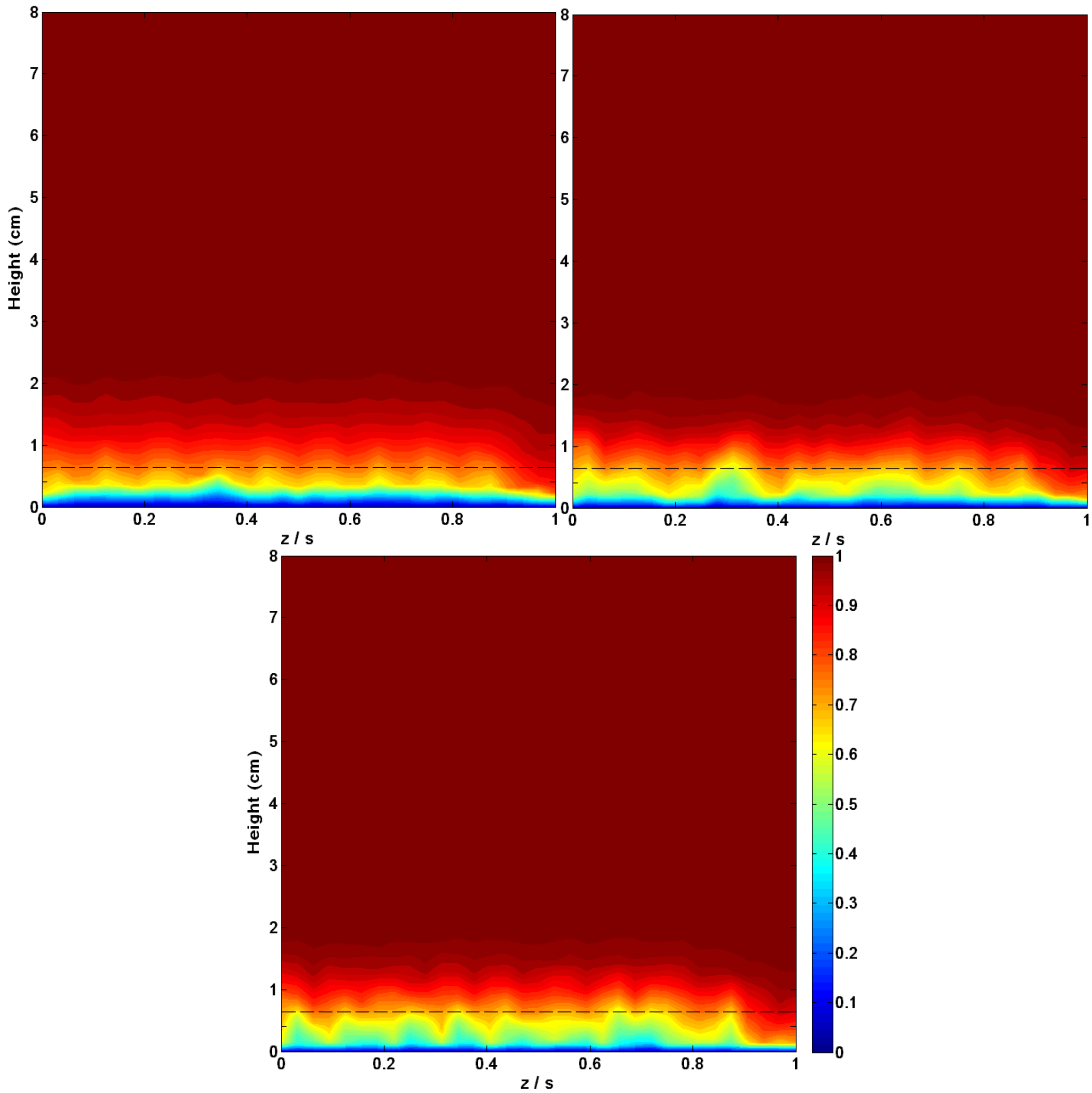

Figure 48: Normalized *u* Velocity Comparisons for Coarse (left), Medium (right), and Fine Meshes (bottom)

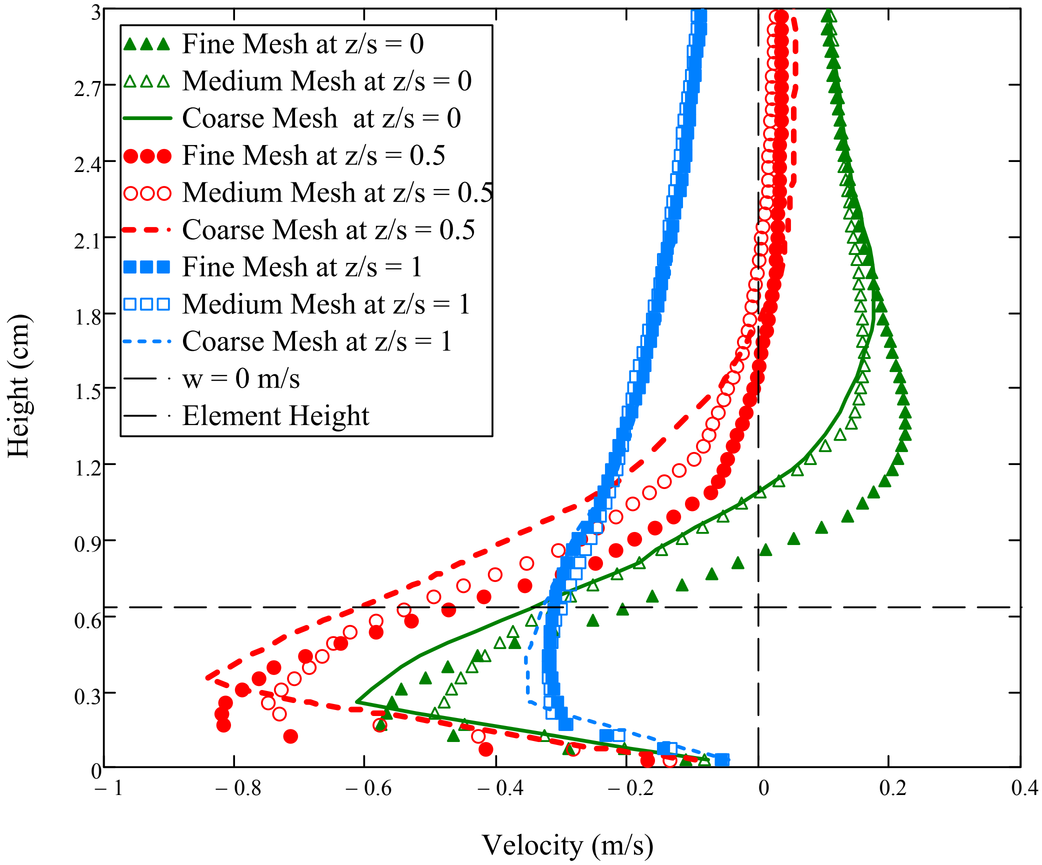

Figure 49: *w* Velocity Profiles for Grid Independence

In Figure 50, the contour plots of the meshes show how the velocities vary across the element height in the middle of the test span. Although the end effects of the test plate are similar with small quantitative differences, both the medium and fine mesh exhibit much higher velocities at different locations on the test span. The coarse and fine mesh models are more consistent with the experimental results in describing the increase of velocities from z/s = 0 to z/s =1 at the element height, yet the medium mesh contains normalized velocities exceeding 0.14 at locations z/s = 0.15 and z/s = 0.4, where values are expected to be lower.

The profile and contour plots of the flow angle quantities for the different mesh models are shown in Figures 51 and 52, respectively, and show results similar to the *w*

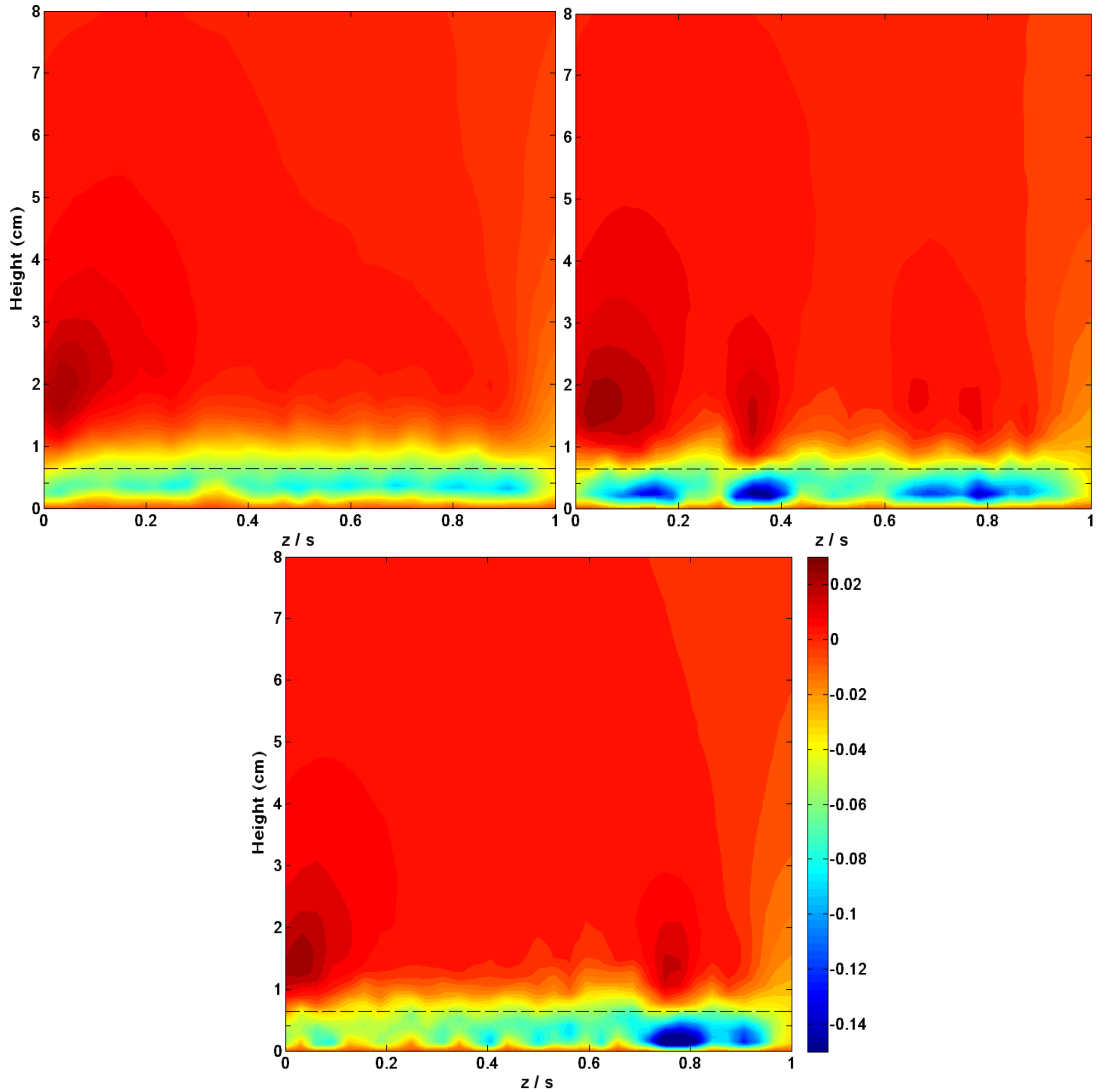

Figure 50: Normalized w Velocity Comparisons for Coarse (left), Medium (right), and Fine Meshes (bottom)

velocities with more agreement among the different mesh sizes. In particular, the flow angle profiles below the element height nearly collapse together for each respective location. Once again, the smaller values are in the coarse and medium mesh results and displayed in the centerline profiles at the beginning height and past the element height, where the flow aligns back to freestream at a lower height for both the centerline and z/s = 0 locations.

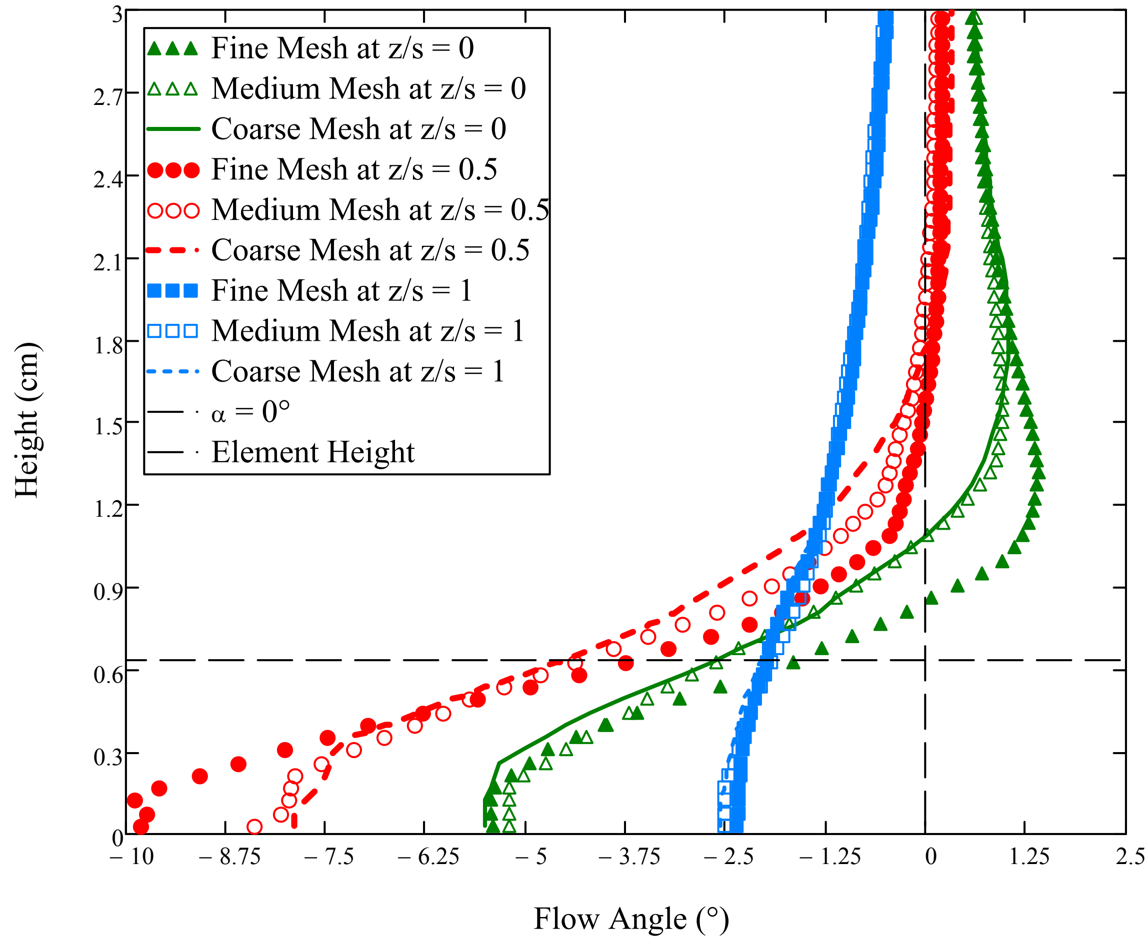

Figure 51: Flow Angle α Profiles for Grid Independence

For the contour plots, the coarse and fine meshes appear to have similar values at the element height across the test span, yet with greater values in both positive and negative flow angles in the fine mesh. Nonetheless, both models display the gaps of lower values and growth of negative flow angles from the z/s = 0 to z/s = 0.9. Once again, the end effects are the similar for the all meshes, yet the medium mesh model contains high negative flow angles, a flow reversal at a later height for z = 0.35, and large variations across the test span.

In Table 4, the computation and residuals data from the CFD results display that, for each case, the residuals from continuity, turbulent kinetic energy, and turbulent

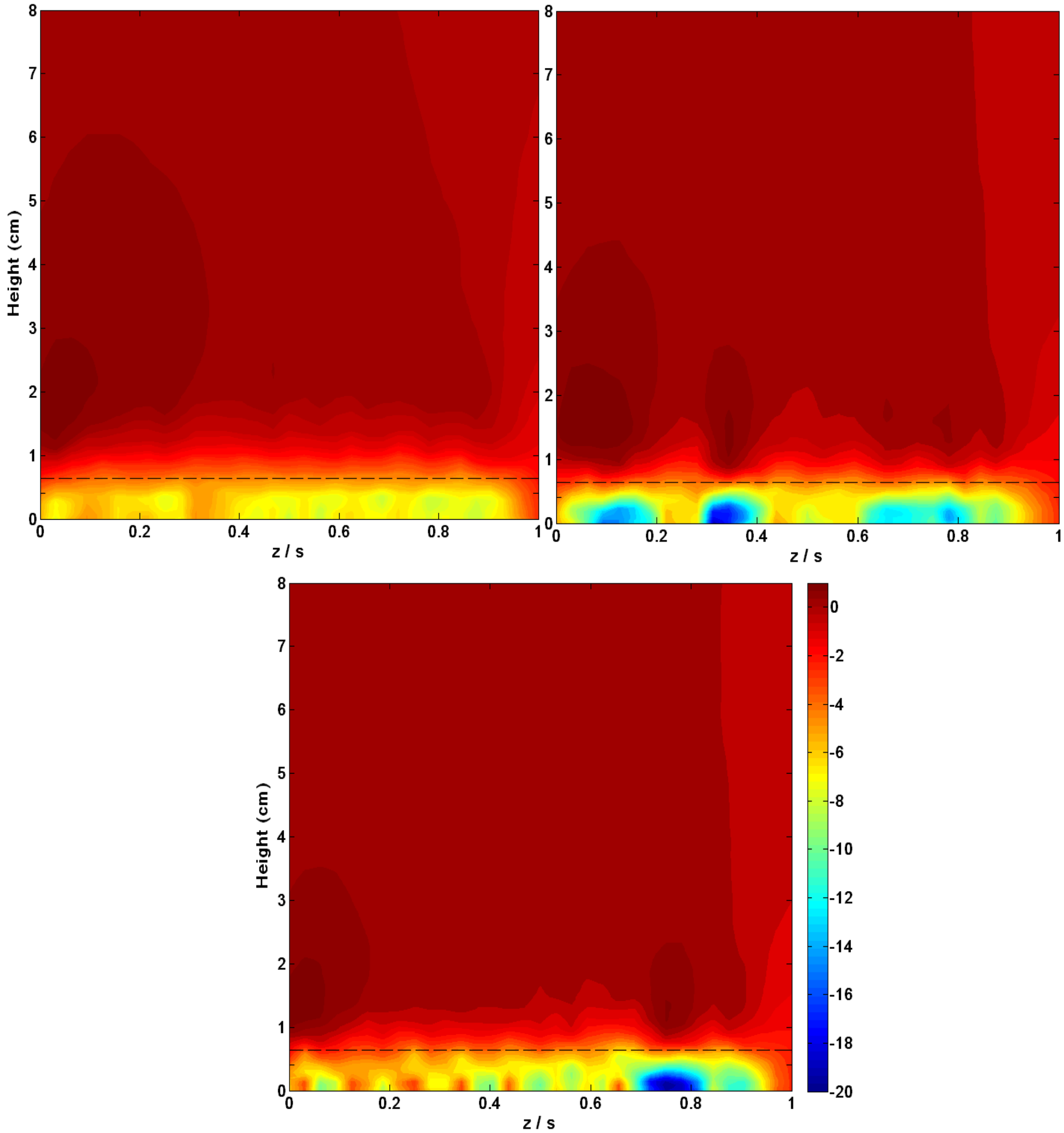

Figure 52: Flow Angle α Comparisons for Coarse (left), Medium (right), and Fine Meshes (bottom)

dissipation did not reach the desired residual value less than 1 x 10^{-6} with oscillating values throughout the remaining iterations. In the medium mesh results, the residuals are approximately an order of magnitude of 10 higher than the coarse and fine mesh despite having the most iterations. This may explain the variations that occur in the *w* velocities and flow angles across the test span.

Although the *u* velocities are consistent with each other throughout the different CFD models, they do not match the experimental values because the viscous effects are not captured. Contrarily, the *w* velocities vary slightly across the test span among the models, yet still have similar values to the experimental values. This phenomenon demonstrates that the capturing of the *w* velocities is based on inviscid pressure effects.

Table 4: Computations and Residuals Data

Mesh Model	*Iterations*	*Properties not converged to 1 x 10^{-6}*	*Time (hr)*	*Time Per Iteration (s)*
Coarse	900	continuity: 1.6615 x 10^{-4} k: 7.4813 x 10^{-5} ε: 2.0466 x 10^{-5}	2.889	11.557
Medium	1800	continuity: 4.5314 x 10^{-3} k: 4.5352 x 10^{-5} ε: 1.8758 x 10^{-4}	4.507	9.014
Fine	1500	continuity: 3.9928 x 10^{-4} k: 1.1628 x 10^{-5} ε: 1.5238 x 10^{-5}	68.730	164.951

Extended Experimental Study

Because viscous effects are not captured by the CFD simulations, the investigation of turbulence quantities is limited to the experimental results. In the following sections, the turbulence quantities are investigated for all test coupons at the freestream velocity of 10 m/s, and an off-speed study is conducted to compare the different test plates at freestream velocities of 2, 5, 10 m/s.

Turbulence

In this section, an in-depth comparison of turbulence profiles for the 15° and No Element test coupons and an overall comparison of the turbulence intensities and Reynolds stresses at $U_\infty = 10$ m/s for all the plates are presented.

15° Orientation vs. Flat Plate. The turbulence intensities, Tu_u and Tu_w, for 15° orientation and baseline flat coupon are shown as profile plots in Figures 53 and 54, respectively. The 15° orientation profile plot, demonstrates that largest turbulence intensities with *u* velocity is almost 16 % and occurs at the element height throughout the span. For Tu_w, values peak before element height also, however beyond that height the intensities are slightly larger towards the left end of the plate (z/s = 0). This effect is propagated up to the height of 5 cm and may be explained by the strength of the directed flow increasing through the columns of the angled elements' pathways.

Compared to the flat plate results, the 15° orientation profiles demonstrate that even though the element height only perturbs about 10 % of the boundary layer height, the turbulence intensities Tu_u and Tu_w extend to approximately 1 cm in height, where the flat plate values are highest in Figure 54. For both test coupons, the values of Tu_u drop to the same turbulence intensities as the Tu_w at 6.5 cm height. Both turbulence intensity components reach the expected freestream turbulence intensity of 0.2% as reported by the wind tunnel manufacturer at approximately 9 cm.

Overall Comparison. For all five test coupons, the contour plots for turbulence intensity components in *x* and *z*, Tu_u and Tu_w, are displayed in Fig. 48 and 49, respectively. From Fig. 48, the plots display that the turbulence intensity Tu_u decreases in strength and height as the angle of the elements orientation decreases for 15° to 5°.

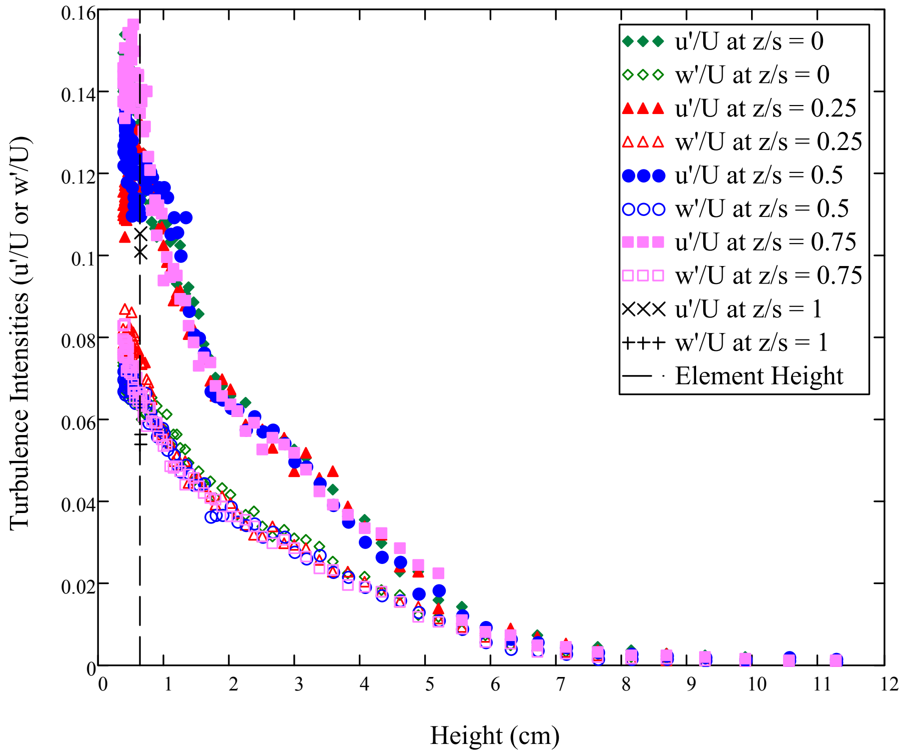

Figure 53: Turbulence Intensities for 15° Orientation at $U_\infty = 10$ m/s

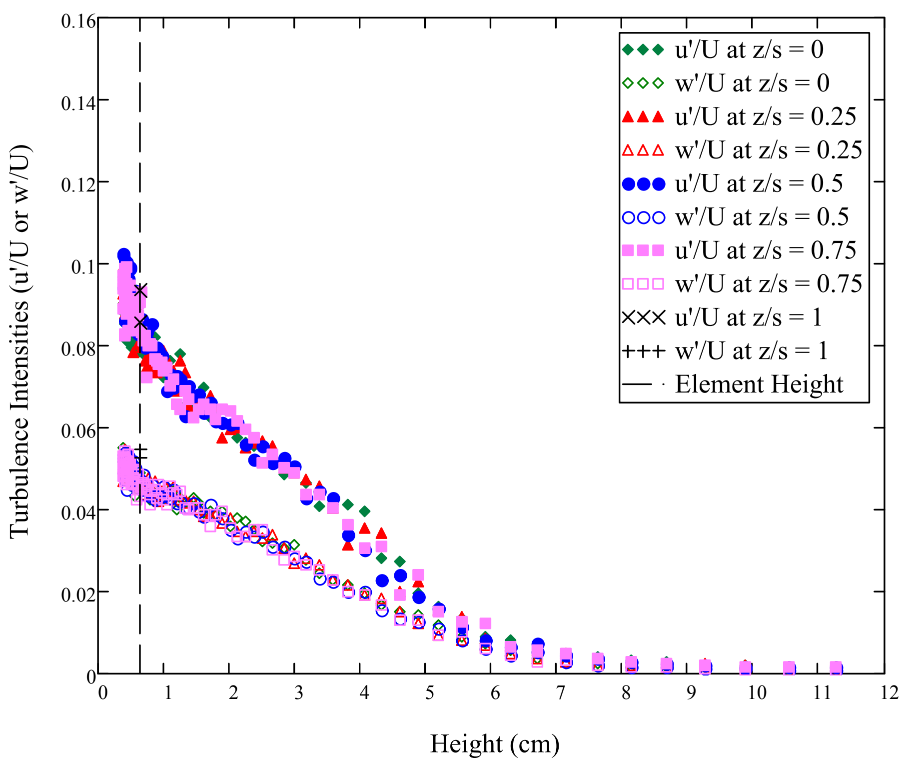

Figure 54: Turbulence Intensities for No Elements Orientation at $U_\infty = 10$ m/s

However, as the angle decreases, the turbulence intensities vary less across the span test coupon. The 0° case is an exception to both of these trends because the pathways seen in the other orientations do not exist and thus, the flow is impeded after each row. Additionally, Tu_u distribution across the plate appears to have higher values in a slanted orientation for the 15° case, but this phenomenon appears to decrease in the lower angle alignments and is no longer distinguishable at the 5° case.

Regarding the z-component of the turbulence intensity, the 10° test coupon is observed to have the least turbulence intensity values across the test span, followed by the 15° case. However, at the 5° and 0° cases, occurrences of stronger turbulence intensities appear across the span in the shape of hemispheres that are extended a little further in height than the other cases. These occurrences may be explained by the ability of the flow pathways to keep consistent velocities behind the elements.

The Reynolds Shear Stress contour plots in Figure 50 display that the cases of 15° and 10° orientation have similar patterns for where the negative values of shear stresses occur, with higher values in the 15° case. Within the 5° and 0° case, there are both negative and positive values of Reynolds stress that alternate along the span of the plate. The negative and positive values indicate the difference in direction of the eddy motion occurring across the plate can may give insight to saying that the 15° and 10° cases have eddies occurring in a consistent direction, thus the flow is moving consistently along the pathways of the arrays. For the other cases, the directed flow is not as strong at the measurement plane. The motion of eddies develop in different directions after the elements because of the separated flow that occurs from each side of the frustums.

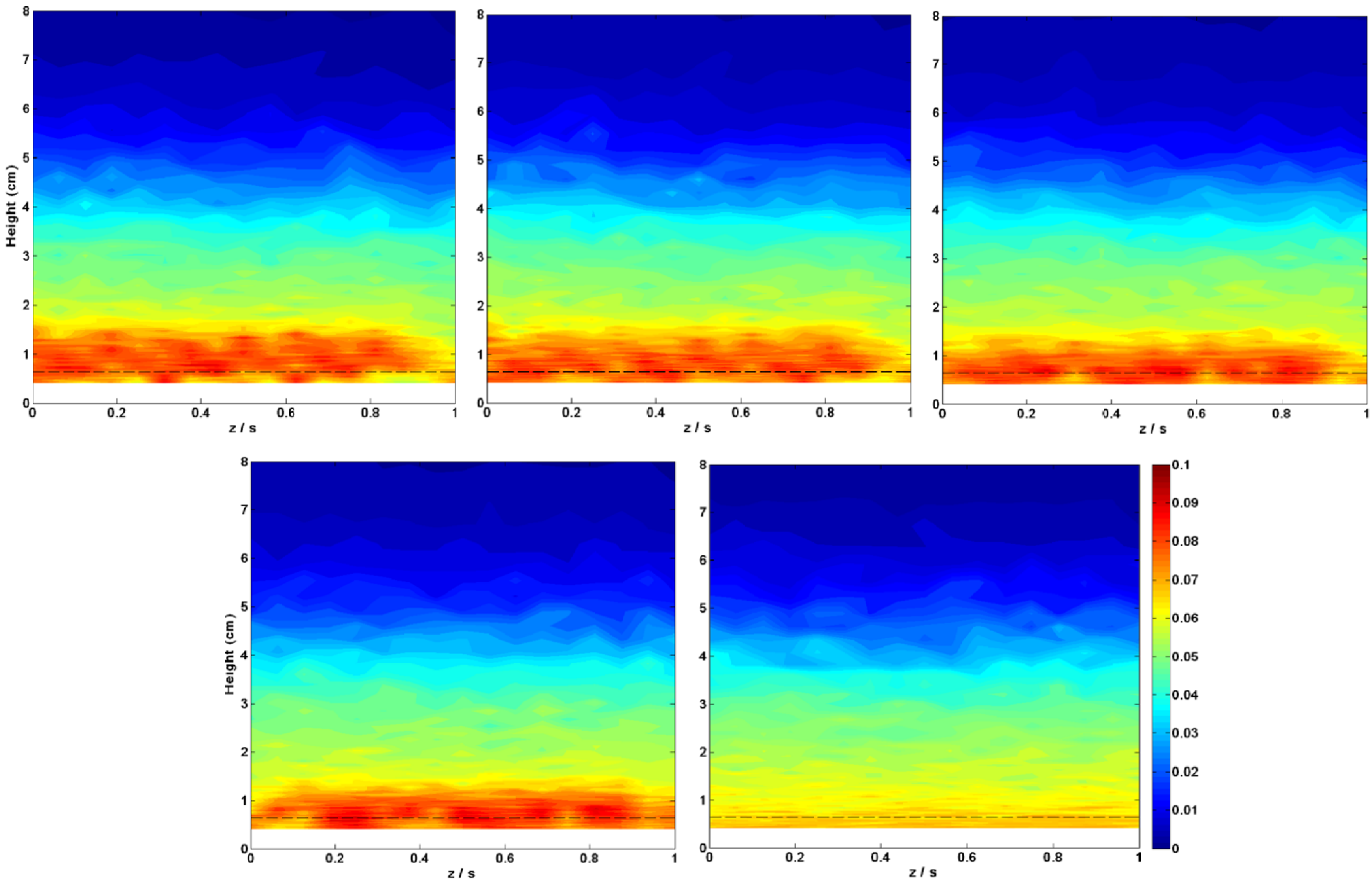

Figure 55: Turbulence Intensities (Tu_u) for 15°, 10°, 5°, 0°, and No Elements (Top Left to Right; Bottom Left to Right) at $U_\infty = 10$ m/s

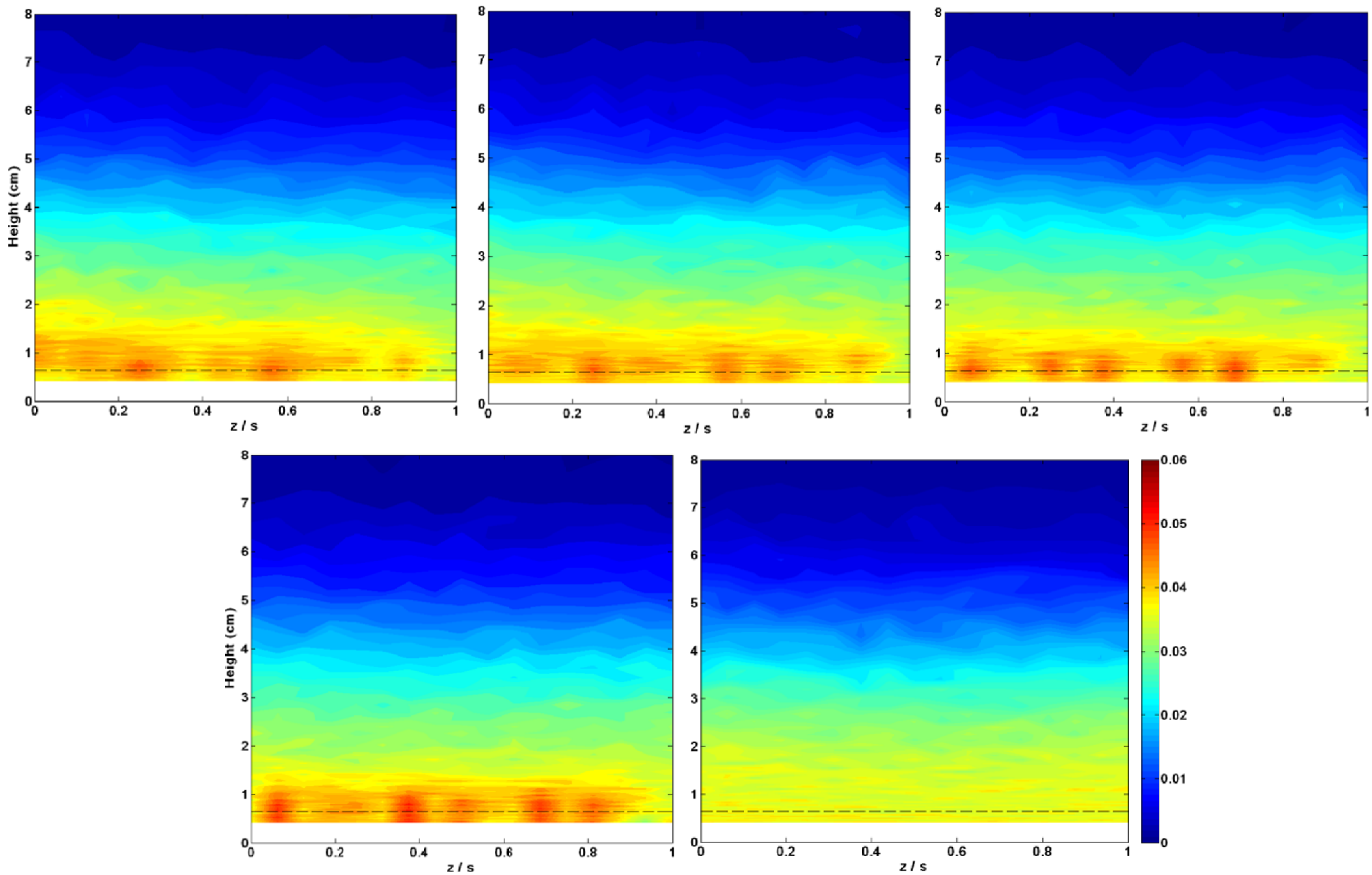

Figure 56: Turbulence Intensities (Tu_w) for 15°, 10°, 5°, 0°, and No Elements (Top-Left to Right; Bottom Left to Right) at $U_\infty = 10$ m/s

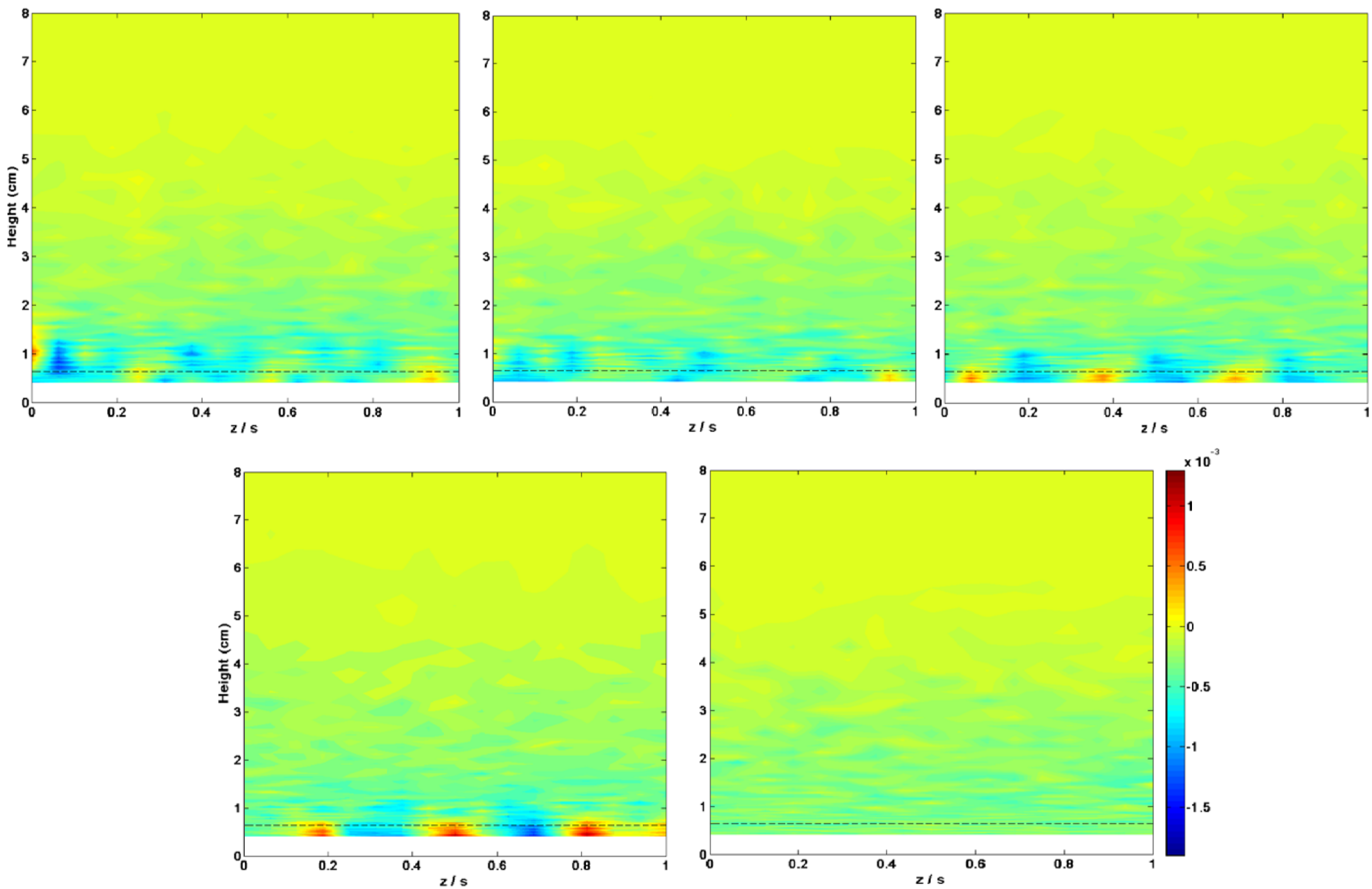

Figure 57: Normalized Reynolds Shear Stress (τ_{Re}) for (for 15°, 10°, 5°, 0°, and No Elements (Top Left to Right; Bottom Left to Right) at $U_{\infty} = 10$ m/s

Off-Speed Comparison

The following section includes comparisons of centerline plots for the different speeds and frustum orientations (FO) evaluated by *u* and *w* velocities and flow angle.

15° FO at 10, 5, and 2 m/s. The normalized *u* velocity in Figure 58 displays the expected turbulent profiles with the same boundary layer height of approximately 5 cm and more turbulent flow occurring for the higher velocities. The normalized *w* velocity and flow angle profiles in Figures 59 and 60 demonstrate how the profiles at speeds of 5 and 10 m/s keep distinct values until the height of 1.5 cm, where the data pair completely collapses.

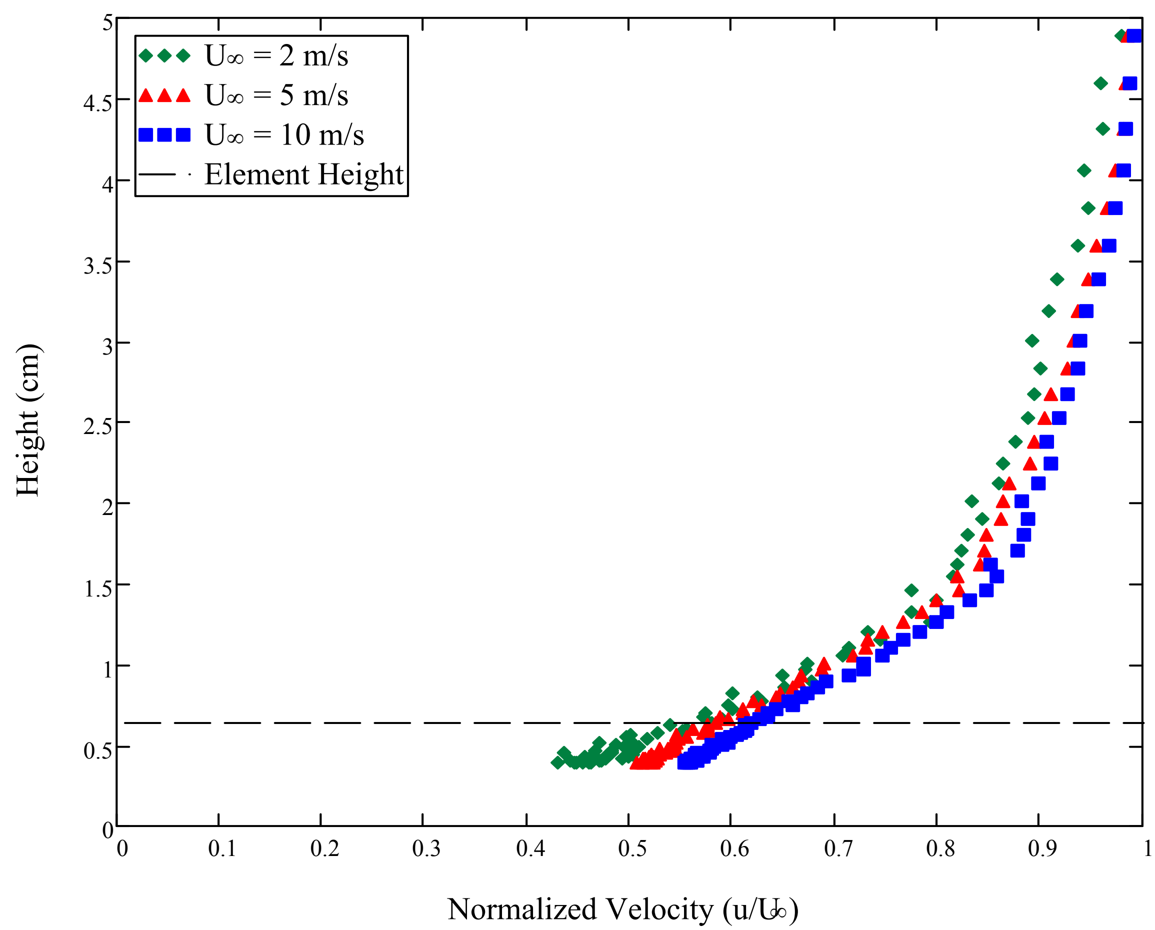

Figure 58: Off-Speed Comparison of Normalized *u* Velocity Profiles for 15° Orientation

From the lowest measurement, the normalized *w* velocity between the two speeds is approximately 0.02 while the flow angle differential value is about 2°. However, at the freestream velocity of 2 m/s there is a large variation in measurement points, especially at the lower measurements because of separation occurring after the frustum arrays.

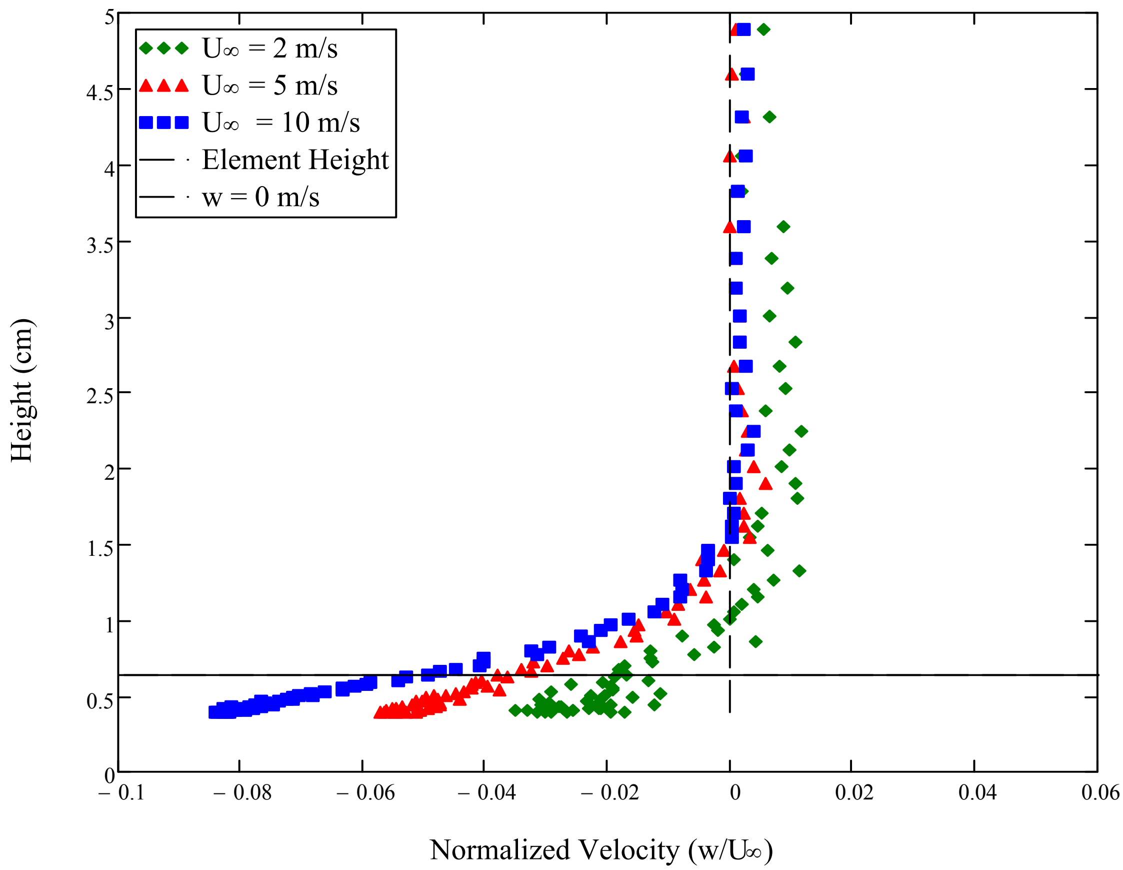

Figure 59: Off-Speed Comparison of Normalized *w* Velocity Profiles for 15° Orientation

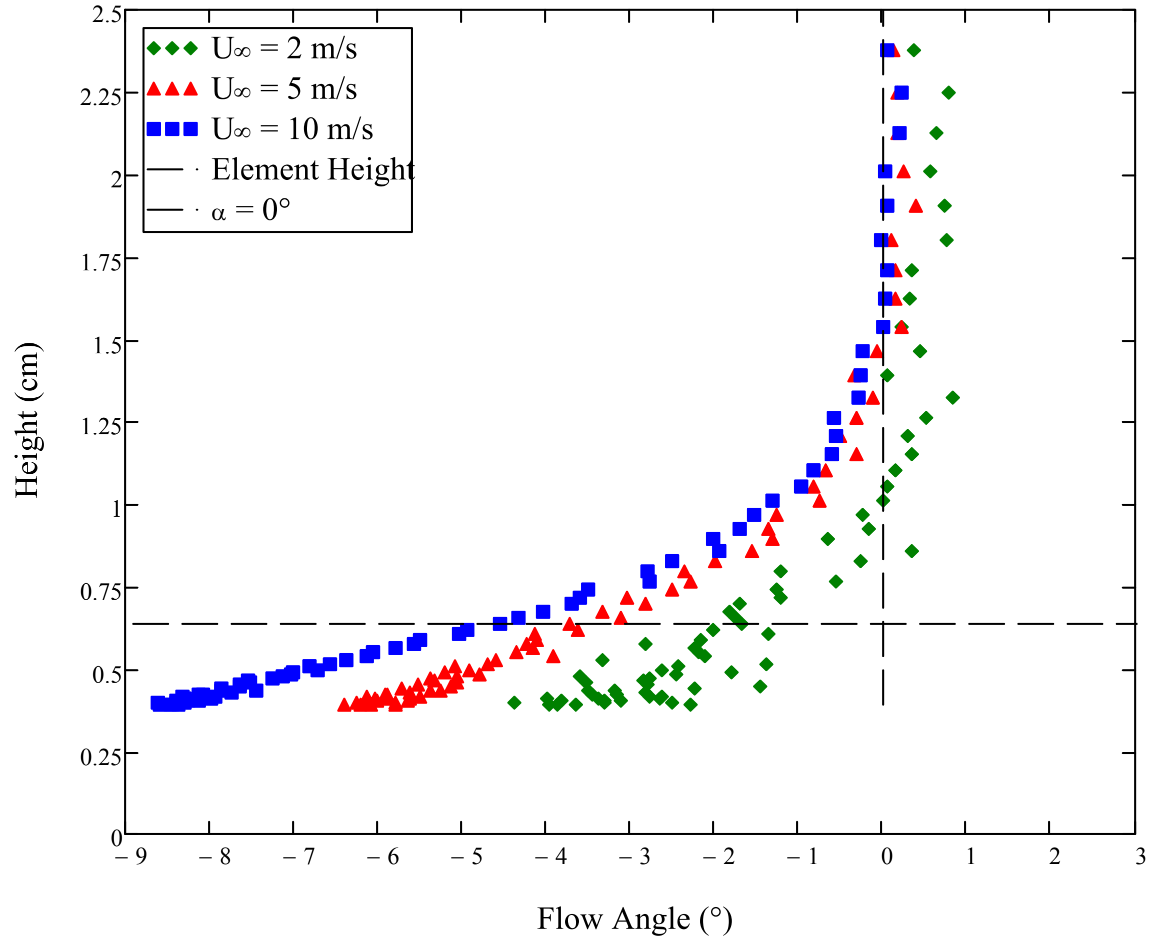

Figure 60: Off-Speed Comparison of Flow Angle α Profiles for 15° Orientation

Case A: 5° FO at 2 m/s, 15° FO at 5 m/s, and 10° FO at 10 m/s. The following figures compare the frustum orientation of 5°, 15°, and 10° at 2, 5, and 10 m/s, respectively. Interestingly, in Figure 61, the *u* velocity boundary layer profiles between the 5° and 15° orientation match up before the element height. This may be due to the combination of a lower freestream velocity and the decrease of the *u* velocity component in the 15° orientation that directs the velocity towards the z-direction. In both the *w*-velocity and flow angle profile plots, displayed in Figures 62 and 63, the 10° and 15° data collapses from the start of the measurements, while the 5° plate remains distinct with little spanwise velocity or flow angle.

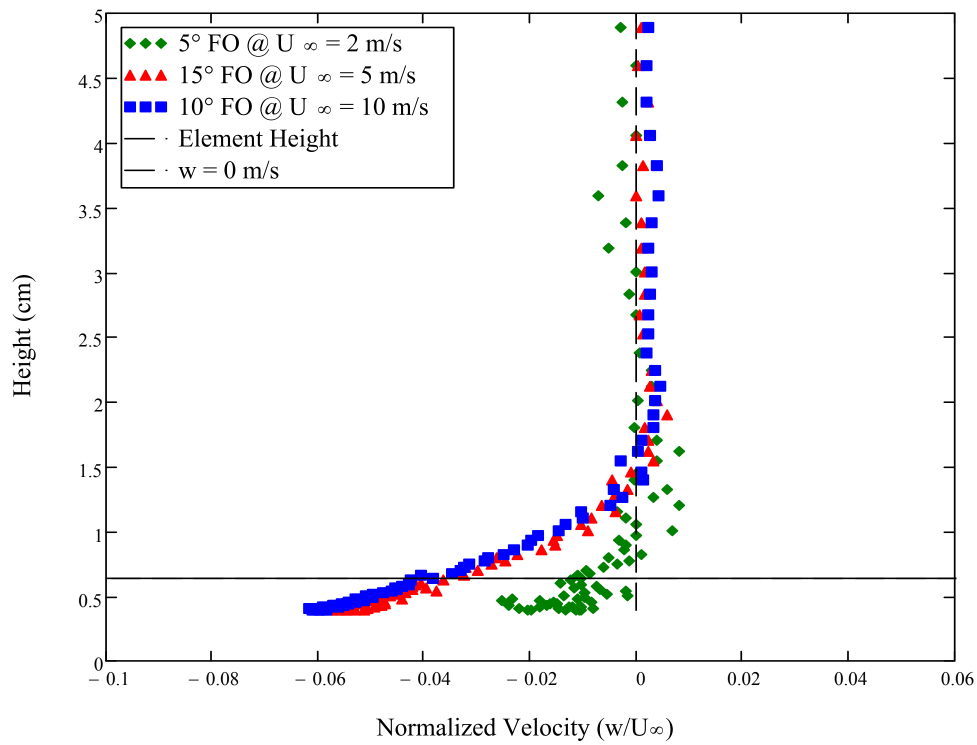

Figure 61: Off-Speed Comparison of Normalized *u* Velocity Profiles for Case A

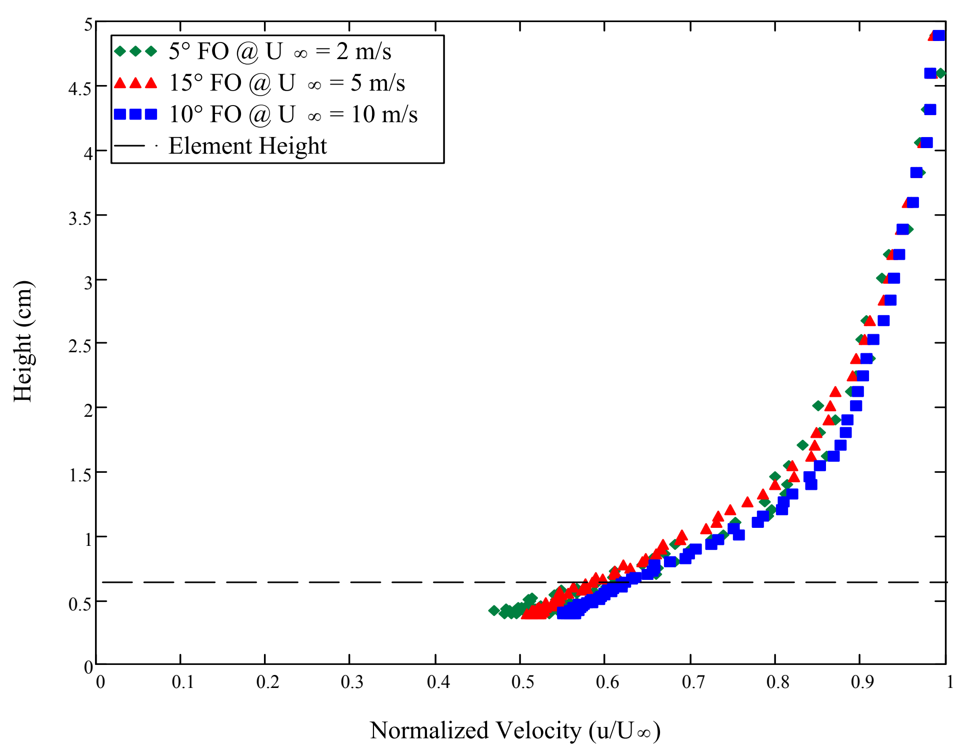

Figure 62: Off-Speed Comparison of Normalized *w* Velocity Profiles for Case A

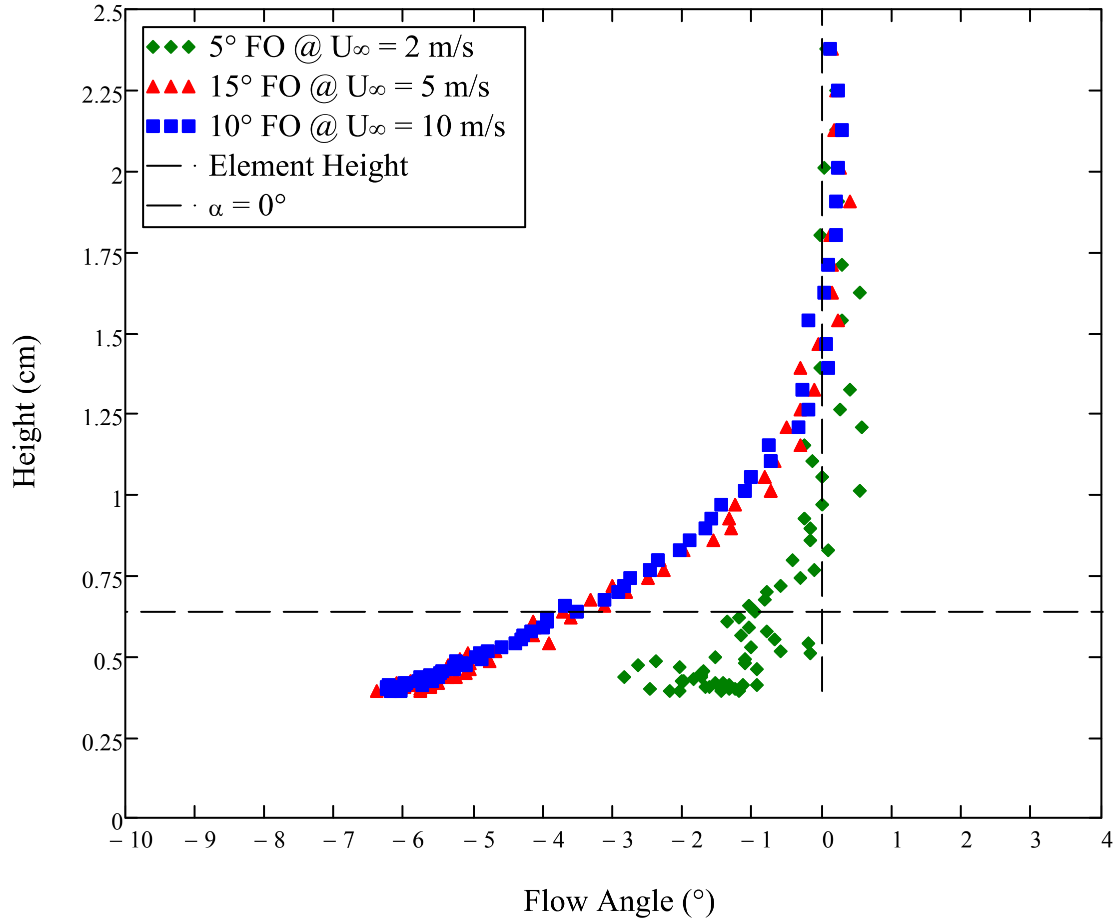

Figure 63: Off-Speed Comparison of Flow Angle α Profiles for Case A

Case B: 15° FO at 2 m/s, 10° FO at 5 m/s, and 5° FO at 10 m/s. The second case of the off-speed comparison includes the 15°, 10°, and 5° orientation for the freestream velocities 2, 5, and 10 m/s, respectively. In Figure 64, the normalized *u* velocity shows a clear distinction between the orientations' profiles for the same reasons indicated in Case A. For the *w* velocity and flow angle profiles, shown in Figures 65 and 66, the 10° and 5° orientations' data collapse in the same manner as Case A. This indicates that there may be a correlation between the magnitudes of the flow with different FOs to match up to each other.

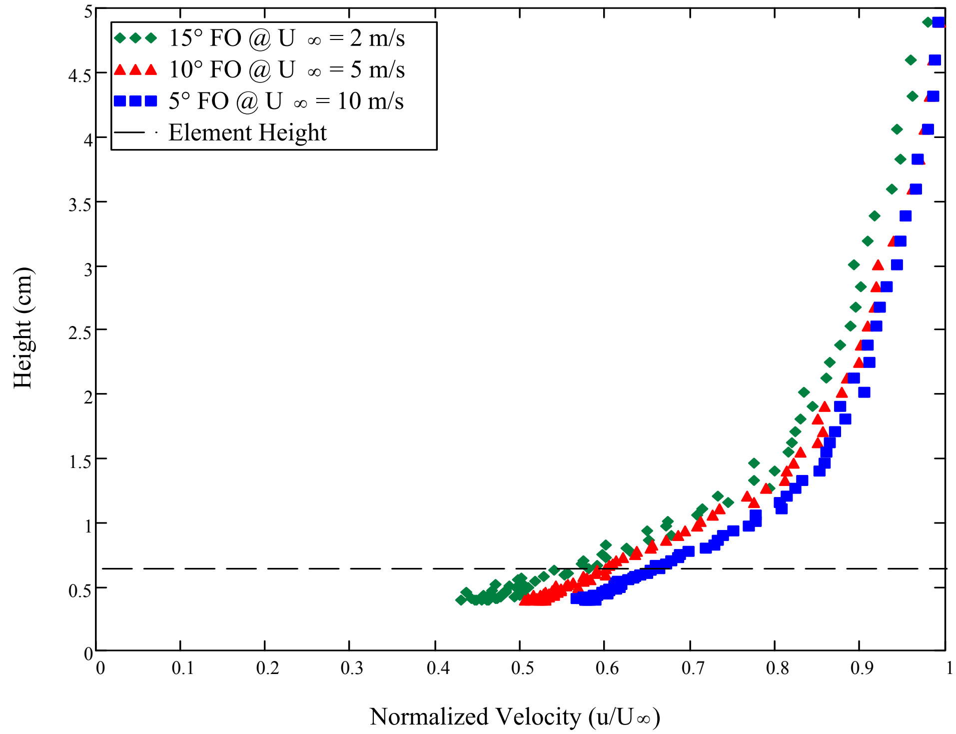

Figure 64: Off-Speed Comparison of Normalized *u* Velocity Profiles for Case B

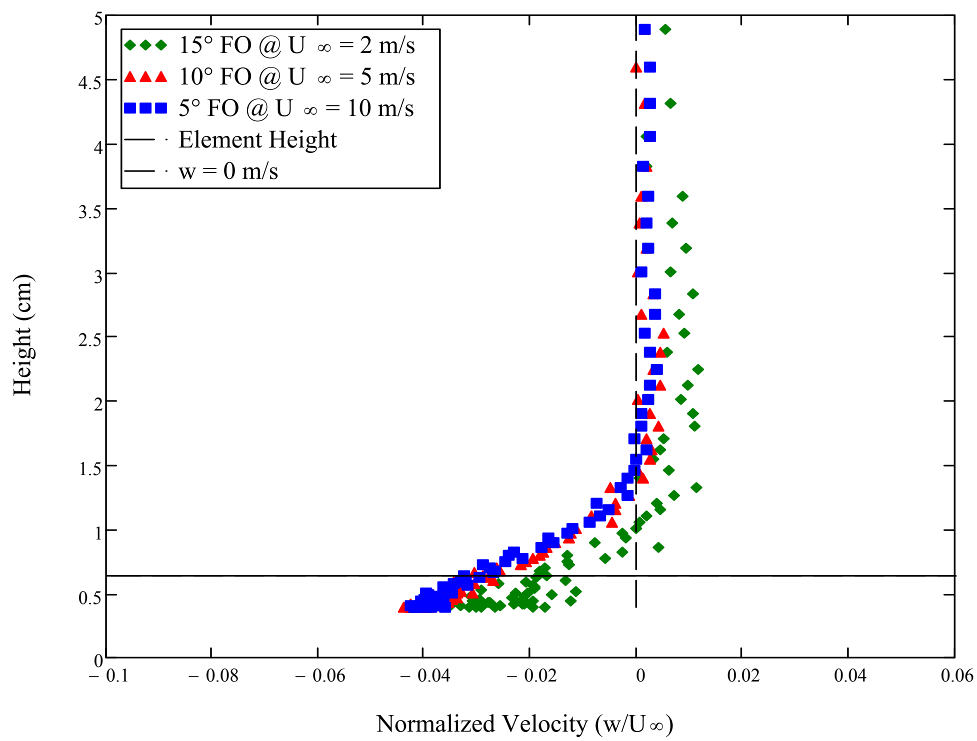

Figure 65: Off-Speed Comparison of Normalized *w* Velocity Profiles for Case B

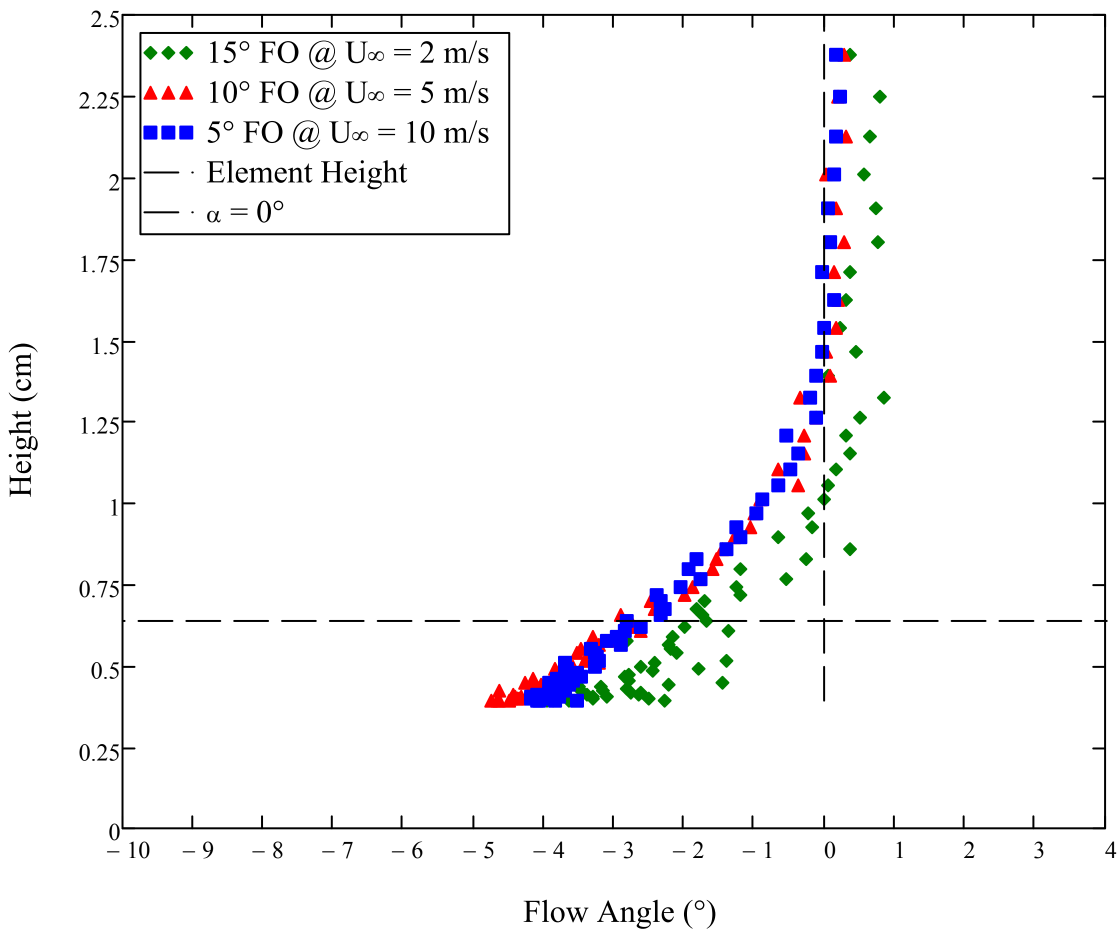

Figure 66: Off-Speed Comparison of Flow Angle α Profiles for Case B

CHAPTER SIX

Conclusion

In the final chapter of this study, a summary of the results, recommendations, and future work involving flow control are presented. The objective of this investigation was to measure the flow characteristics and turbulence quantities produced by arrays of 0°, 5°, 10°, and 15° frustums in turbulent flow at 2, 5, and 10 m/s on a flat plate.

Summary of Results

The experimental results demonstrate that the effects of flow tailoring were captured at the downstream measurement plane. For the *u* velocity, the boundary layer appears to have a less turbulent boundary layer profile with higher alignment angles because flow is being directed to the *w* velocity component. With the angle orientation, the *u* velocity slightly drops, but loss of the *u* velocity is minimal between the angles. Regarding the *w* velocities and flow angle, the flow from a specific test coupon orientation is distinguishable up to the element height, but does not reach the freestream velocity or flow angle until the height of 2 cm for measurements taken between the ends of the test span.

These experimental velocities and flow angle quantities were compared to CFD simulations using the k-ε turbulence model at U_∞ = 10 m/s to explore the ability of commercially available CFD software to predict the flow results. In the CFD results, viscous effects were not captured since the boundary layer height for the *u* velocity is approximately 2.5 cm lower than the experimental data. For the *w* velocities and flow angle, the CFD and experimental values were reasonably agreeable, especially for the centerline measurements. However, there may have been some overestimation of quantities predicted but this cannot be confirmed due to the height limitations of the probe. Additionally, the CFD predictions appear to have trouble simulating flows around the roughness elements as the angle of obliqueness increases. These problems may be associated with the viscous effects that created the inconsistency in the *u* velocity boundary layer.

In the grid independence study, the coarse, medium and fine meshes were observed to be similar to each other for *u* velocity, *w* velocity, and flow angle values. The *u* velocities demonstrated the best match among the grids although the boundary layer heights are different from the experimental values. The *w* velocity and flow angle values demonstrate the same trend of increasing quantities below the element height for all grids. In the residuals and test results, the variations of both the flow quantities across the test span in the medium mesh are explained by the lower values of residuals even with the most iterations executed. Despite this shortcoming, the results still demonstrate that the flow turning inside the boundary layer is an inviscid pressure effect.

Furthermore, the extended study of the experimental results was conducted to examine the turbulence intensities and normalized Reynolds stresses. The effect of frustum orientation in the x-component of the turbulence intensity shows some indication of flow tailoring occurring by the increasing and decreasing quantities in an angled pattern across the test span. Regarding the z-component of the turbulence intensity, the 15° and 10° plates show a wider distribution of turbulence, while the 5° and 0° test plate display concentrated areas with larger turbulences than those in the previous plates, with the 0° case being the highest. The normalized Reynolds stresses are lower in one direction for the 15° and 10° plate, indicating the flow may be directed in an ordered manner. The remaining frustum orientations not only display larger values of normalized Reynolds stresses, but the occurrence of shear forces in different directions in the flow indicated by the negative and positive values.

Finally, an off-speed comparison between different frustum orientations and velocities was conducted to also demonstrate that at certain combinations of FO and freestream velocity, the *w* velocities and flow angles at centerline can emulate each other.

Recommendations & Future Work

Regarding CFD, a higher node count for the meshed model and equal boundary layer spacing throughout the model may alleviate the problem of the non-captured viscous effects. Once the experimental and computational values are in better agreement, other flow qualities such as vorticity and shear stress on the surface should be explored in order to compare to studies regarding wing-tip vortices. Since the test coupon has a finite span of frustum arrays, a measurement should be taken at least 1.27 cm outside of the test span to study the vortical effects at the ends. The future work should also include a study of the micro-balloon shaped elements, displayed in Figure 67, that simulate the geometry of a possible MEMS system based on the concept from Tung et al. [33]. With the same array arrangement, dimensions, and angles of alignment, the flow and turbulence quantities will be investigated and compared to the current results of the frustum arrays.

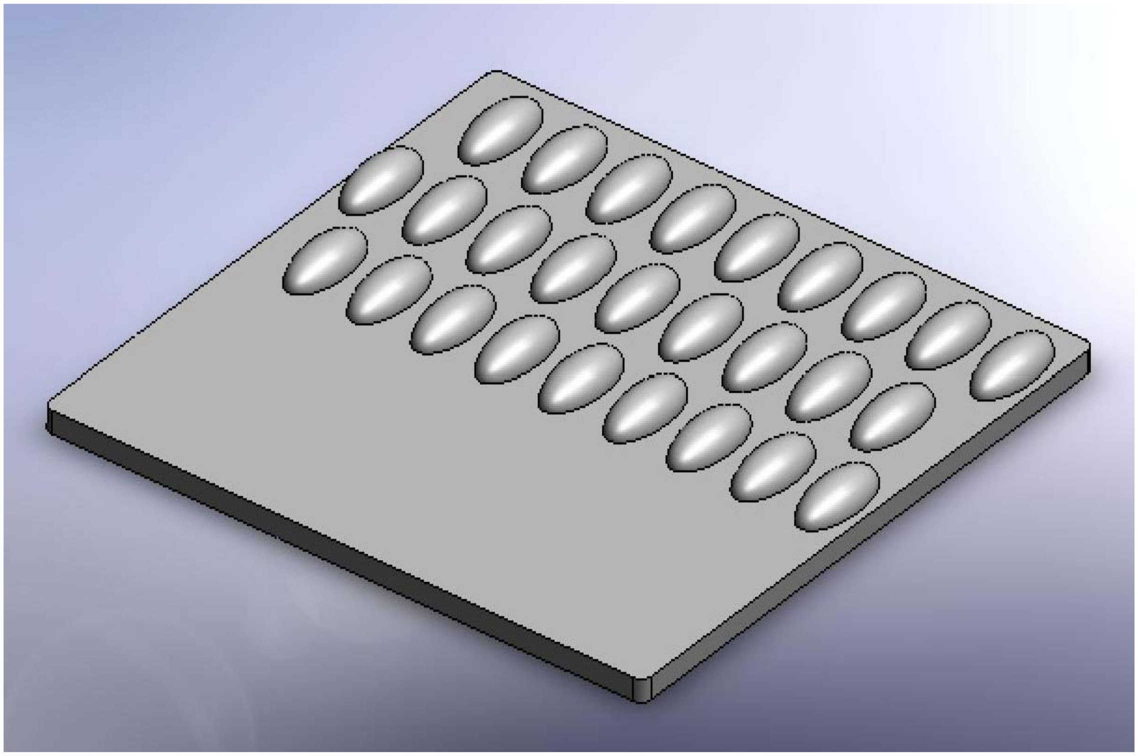

Figure 67: Test Coupon with Ellipsoidal “Bubble-type” Elements

APPENDICES

APPENDIX A

LabVIEW Automation and DAQ

For this experiment, National Instrument's *LabVIEW*, a visual programming language, was used for multi-tasking between instrumentation and data acquisition. The program will create a folder that will house a summary file of laboratory conditions and hot-wire anemometry voltages and also create a file for each hot-wire anemometry measurement containing only the raw voltage samples. The summary file contains the following inputs with the entries containing (*) to denote the random uncertainties were also calculated:

- measurement reference number
- date
- time
- probe position upstream
- probe position downstream – z
- probe position downstream – y
- time elapsed
- atmospheric pressure
- relative humidity*
- free stream temperature*
- dynamic pressure*
- voltages*

As each voltage measurement file is created, the summary file will update for each measurement taken in both upstream and downstream measurements. The program operates in a sequential manner to move the position of the hotwire anemometry probes by controlling the *Velmex* Positioners and measuring the voltages along a line in the upstream flow using a geometric spacing equation for more positions to be measured closer to the plate. This process is repeated for a grid of measurements in the downstream measurement, and the probes are reset to their original location to finish the test run.

Data Acquisition

The data acquisition system for this experiment is composed of five major components: transducers, signal conditioners, DAQ device, computer workstation, and DAQ software. The flow of data is shown in Figure A.1.

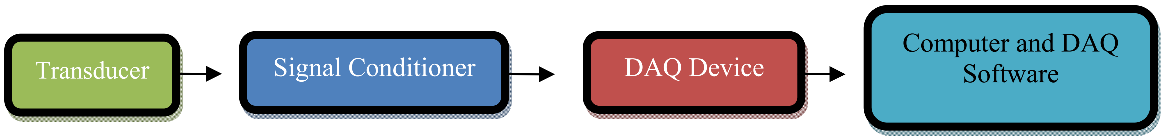

Figure A.1: General Data Acquisition System

Although the transducer/signal conditioners vary according to the physical phenomena being measured, the DAQ device is different for the laboratory measurements and hot-wire voltages because of the requirements for sampling a signal. The hot-wire anemometry system must use simultaneous sampling to minimize the phase shift among the channels in order to derive moments at both the u and w velocity measurements and cross-moments (Reynolds shear stresses). However, the laboratory conditions may have a larger phase shift among the measurements and use the interval sampling method.

Laboratory Measurements

The relative humidity and free stream temperature were measured with their own respective transducer/signal conditioner device and connect to *National Instruments BNC 2110 Shielded Connecter Block* to simplify and protect the connection of analog signals. The connector block is linked with a 68-pin connector cable to a *National Instruments PCI-6052 E Multifunction DAQ* to run interval sampling. The *Analog Input (AI) Acquire Waveform* Virtual Instrument in the *LabVIEW* environment, displayed in Figure A.2, can acquire a specified number of samples at a specified sample rate from a single input channel in the DAQ device and output the acquired data.

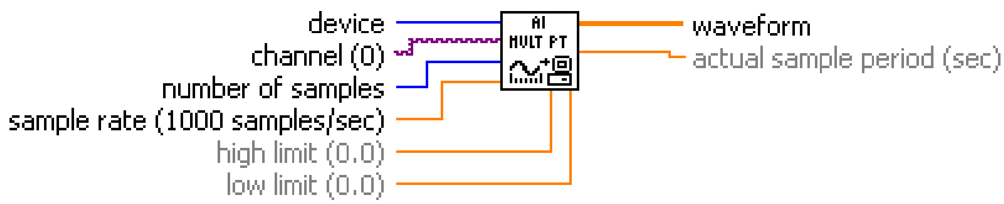

Figure A.2: AI Acquire Waveform VI

Additionally, the dynamic pressure is measured using an *Omega PCL2-A* Pressure transducer and relays measurements into the computer via serial port communication. For this measurement, *Virtual Instrument Software Architecture (VISA)* is used to communicate with the serial-interfaced instrument. Shown in Figure A.3, the *VISA* VIs are shown to configure the serial port, writes the data from the *Write buffer* string to pressure transducer device, reads the specified number of bytes from the device and returns the data in *Read buffer*, and finally closes the session.

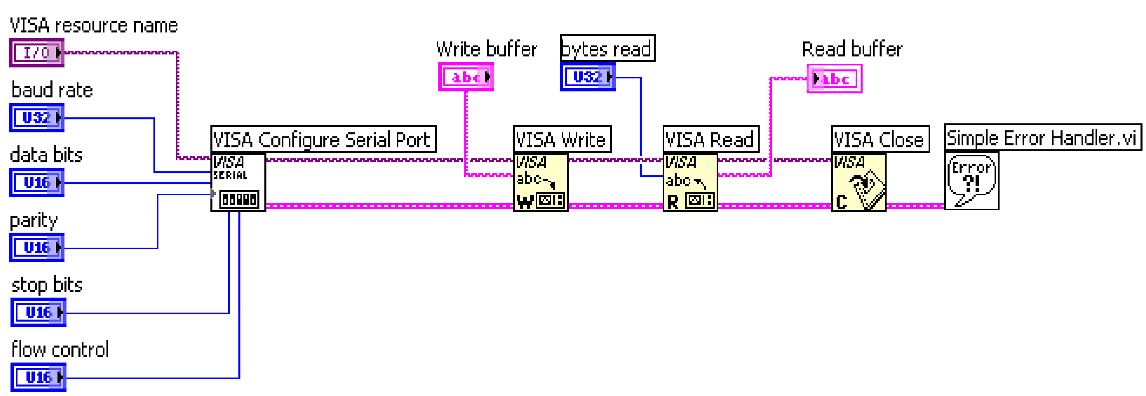

Figure A.3: Sample VISA block diagram

Hot-Wire Anemometry Measurements

The voltages were measured using the X – hot-wire probes powered by the *IFA 300 Constant Temperature Anemometery* system. The *Thermal Pro* software is used to assign the channels and probes and function as a signal conditioner to input the gains and offsets for measurements. However, since simultaneous measurements from the hot-wire probes are desired, a PD2-MFS-4-300/16 PowerDAQ device from *United Electronic Industries* is used inconjuction with *LabVIEW* with additional DAQ framework architecture displayed in Figure A.4.

Figure A.4: UEIDAQ Framework Architecture

The UEIDAQ framework contains a LabVIEW binding to allow communication with the core of the framework, the UEIDAQ Application Programming Interface *(API)*. The UEIDAQ API detects the hardware devices and implements a hierarchy of classes to manage communication with the PowerDAQ device. The PowerDAQ device driver for LabVIEW allows the user to execute a DAQ session with pre-configured VIs, displayed in Figure A.5, that follow the hierarchy of classes. The data and commands are then relayed using a Peripheral Component Interconnect (PCI) Board with simultaneous sampling capabilities.

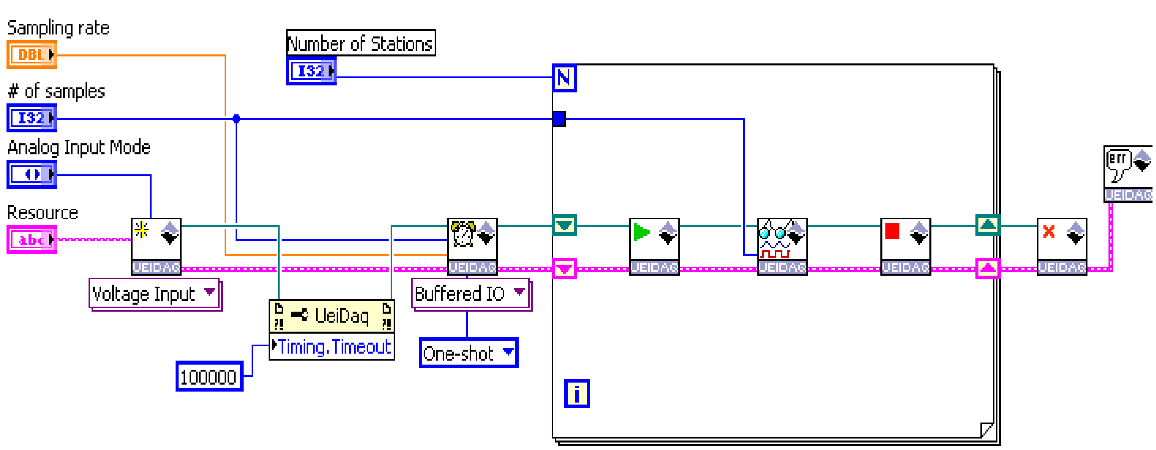

Figure A.5: Summary of UEIDAQ VIs used for the Boundary Layer Test

The UEIDAQ framework and classes are distributed into the different sequence frames and sub-VIs within the test program. The program executes through the UEIDAQ VIs and gives the operator feedback with the description of the error at any point within the experiment. The first two VI icons on the left, detailed in Figure A.6, create a session and configure the timing for the data acquisition, respectively, and are displayed in the input section of the program. For the *Create Session* VI, the resource draws from the PowerDAQ with a minimum and maximum range to be set by the operator. The property node between the two icons indicates that the data acquisition timeouts automatically after 100 seconds of starting the session. The *Configure Timing* VI is set to Buffered IO mode to allow for high-speed data acquisition and to read a finite number of samples per channel (*One-shot*) then stop the data acquisition session.

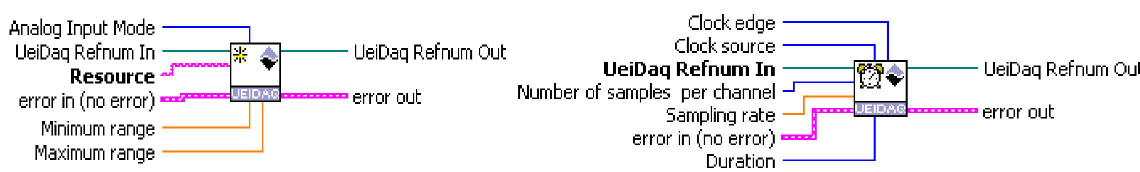

Figure A.6: UEIDAQ VIs - Create Session (left); Configure Timing (right)

Inside the for-loop structure, the session starts, data is read, and the session finishes for that measurement. The shift register was used in-order to continue the data acquisition process for a station in the experiment by starting, reading, and stopping the data flow for each measurement. This portion of the UEIDAQ framework is found within the measurement sub-VIs of the program described later. After all the desired measurements have been taken and if no errors have occurred, the session is destroyed and the program will finish properly.

User Interface

The front panel window of the program, shown in Figure A.7, prompts the user to specify the number of measurements for both the upstream and downstream flow, the atmospheric pressure of the laboratory, the channels used in the PowerDAQ device, nomenclature for naming files and folders, number of samples per channel, and sampling rate. For the upstream and downstream flow measurements, the user can input the number of stations to scan, the length of the boundary layer measurement, and a scaling factor to determine a geometric spacing between the scans. As displayed in Figure A.8, the scaling factor is 1.07 for the upstream and downstream Y-axis in order to concentrate the number of scans closer to the surface of the plate, while the downstream Z-axis scaling factor is 1 to provide an equal grid of lateral spacing for the Y-axis stations. Furthermore, the user can see the individual movement length between the scans for the upstream and downstream grid and view the voltages of the probes as the program progresses.

Block Diagram Code

The operator must align the probes at the lower limit coordinates and the downstream probe at the end of the test coupon that is away from the CTA/DAQ system. The user inputs are displayed in the front panel are located on the left side of Figure A.8, including the file and folder creation and concatenation scheme. Additionally, the first sequence in the program, Frame 0, sets the absolute or origin position of the *Velmex* Positioner system for both the upstream and downstream and references these positions in order to return to them at the end of program. The upstream and downstream measurement sequences are very similar with the exception of a nested loop for generating a plane of measurements in the downstream flow. The following is a description of the sequence of events and sub-VIs used throughout the execution of the program.

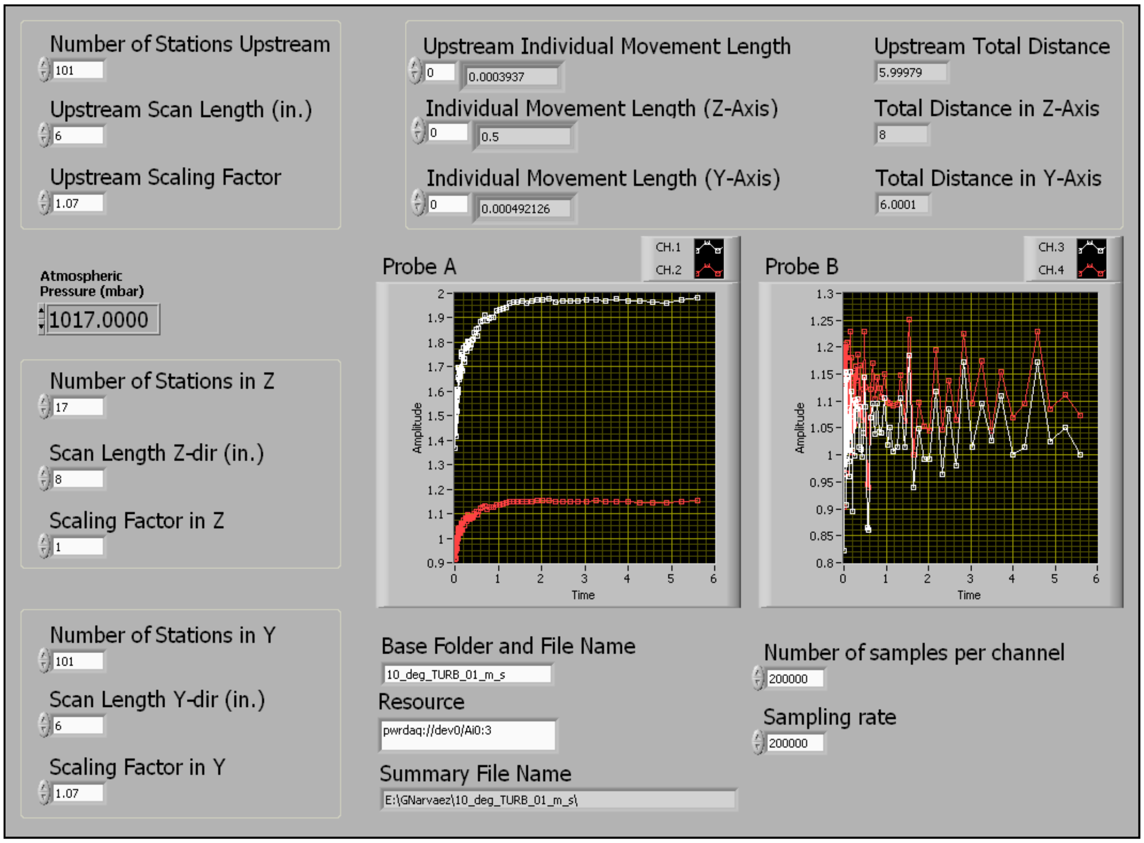

Figure A.7: LabVIEW Front Panel of Boundary Layer Measurement Program

Frame 1: Initializing Upstream Positions

The first frame in the Upstream Measurements section, shown in Figure A.9, the *Auto Step Size* sub-VI is enclosed within a for-loop structure that will iterate for the *Number of Stations Upstream* input. The sub-VI reads in the *Scan Length*, *Scaling Factor*, and *Number of Stations Upstream* inputs to determine the *Scan Positions*, *Number of Steps at Station*, *Total Number of Steps* outputs and displays the *Total Distance* and *Individual Movement Length* in the front panel. Using a local sequence, the scan positions, number of steps at station, and total number of steps values are passed to later frames to indicate the distance per interval and the amount of steps required to reach the distance per interval and to return the probe to its absolute position, respectively. It should be noted that the *Motor Step Size* input refers to the advance per step; thus, for the upstream measurements, the Velmex Unislide Positioner value is 0.0005 cm. per step.

Auto Step Size sub-VI. The coding for the Auto Step Size sub-VI allows for it to be used for upstream measurements and generating a grid of measurements in the downstream region. This sub-VI finds the amount of steps required at a measurement station, then utilizes the user inputs to determine the total number of steps for the station, individual movement length, total distance, and scan positions. As shown in Figure A.10, the Scaling Factor input will determine the type of algorithm used for determining spacing. Thus, only if the scaling factor is equal to 1, the case structure will yield "True" and the intermediate variable Y can be found for by Eq. 1 and 2 for both "True" and "False" conditions, respectively:

$$Y = L/N \tag{1}$$

$$Y = L * \frac{(1-SF)}{(1-SF^N)} \tag{2}$$

where L is the scan length, N is the number of stations in scan (minus 1 to set the amount of movement intervals), and SF is the scaling factor. After Y has been calculated, this variable and the scaling factor input enter a for-loop structure containing a formula node and case structure that will iterate for the number of stations in scan minus one to calculate the number of steps to reach each station. From the formula node, the number of steps required to reach the distance interval, ΔI, is displayed in Eq. 3:

$$\Delta I = Y * SF^i \tag{3}$$

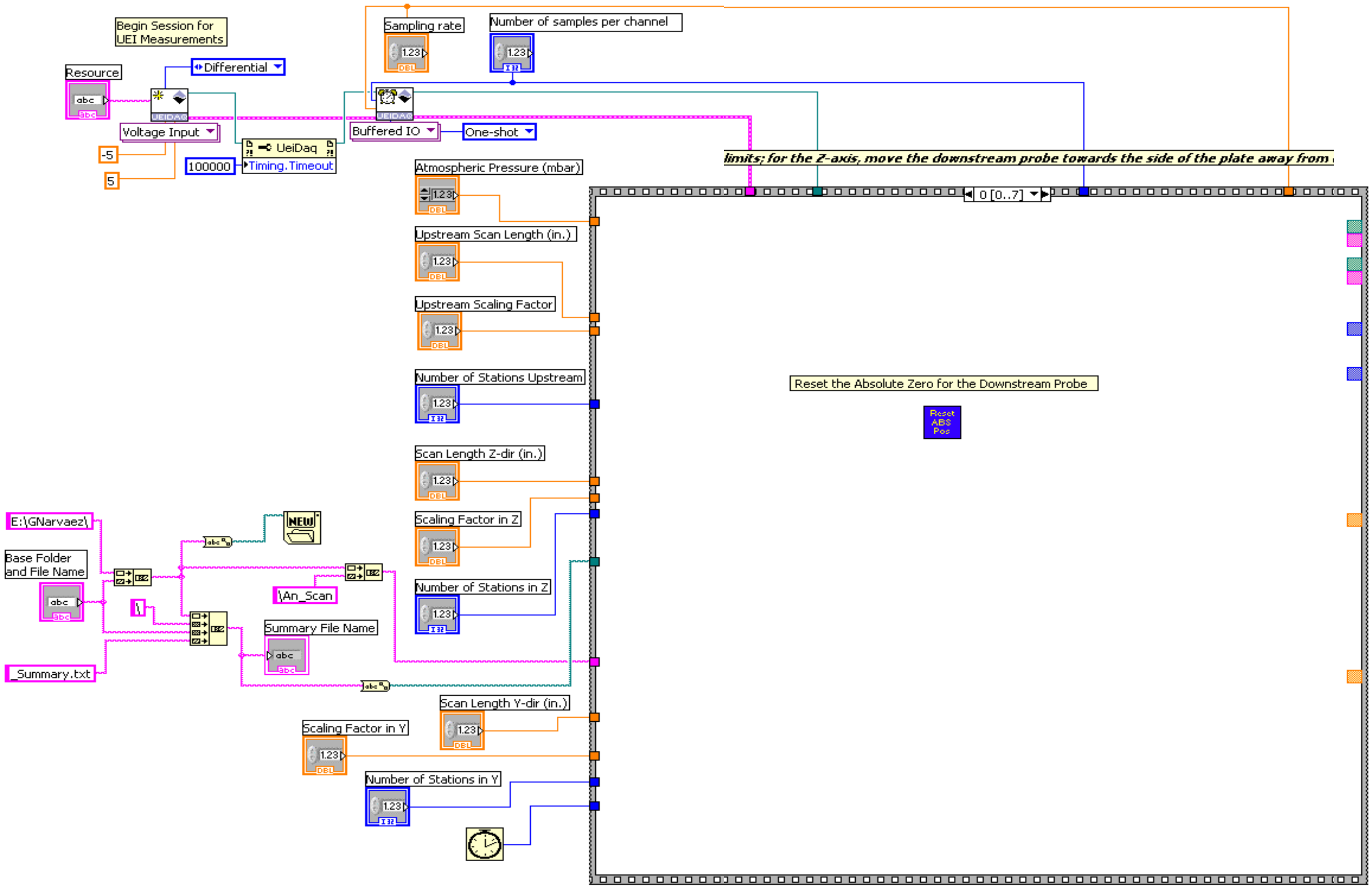

Figure A.8: Overview of Boundary Layer Test VI with Reset Absolute Position VI

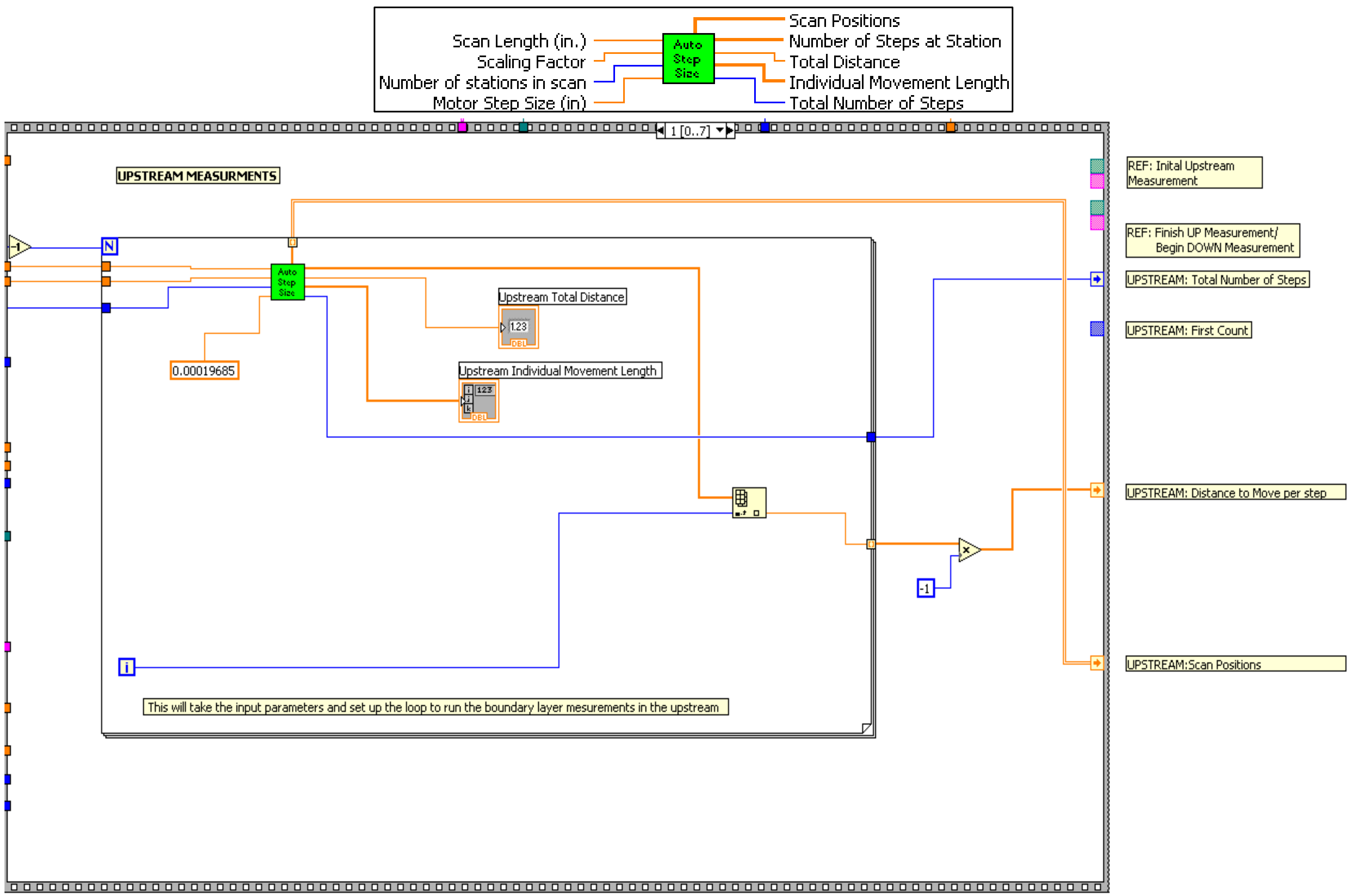

Figure A.9: Initializing Upstream Measurements (Frame 1)

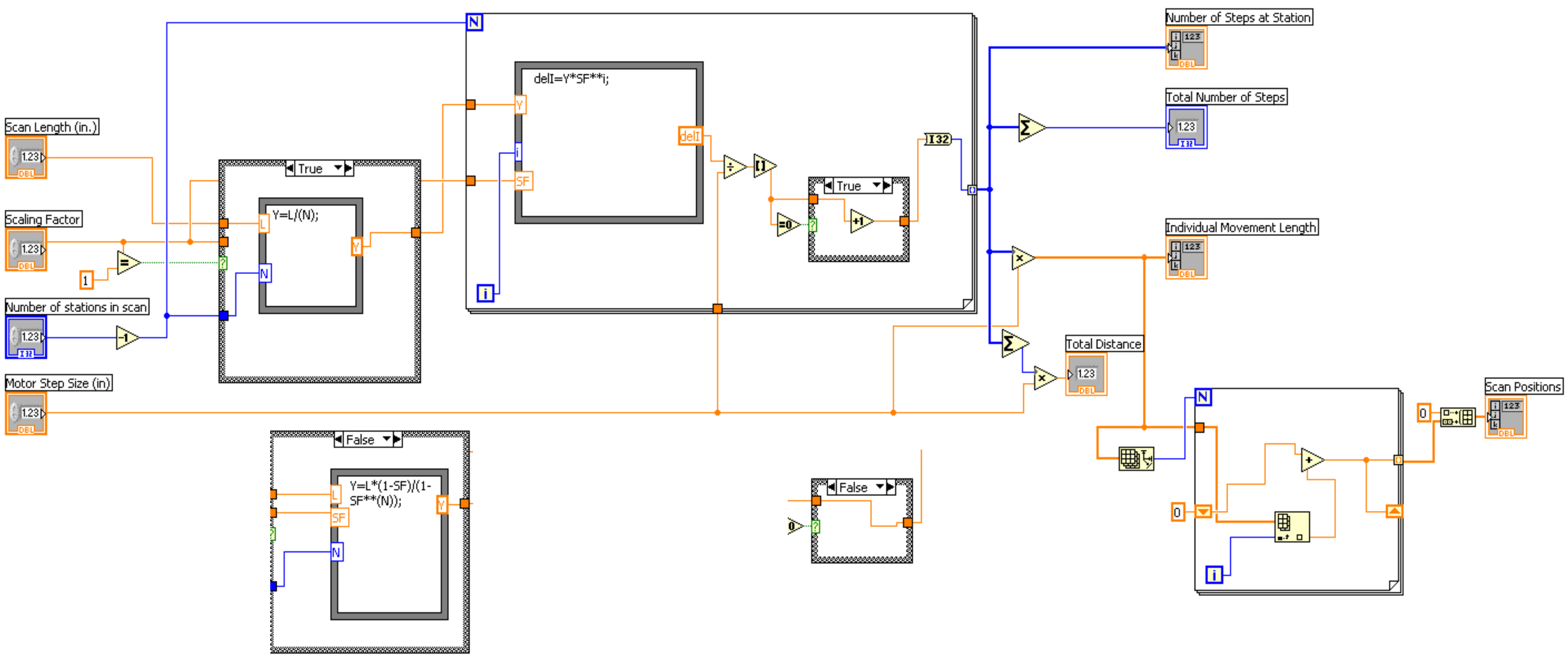

Figure A.10: Auto Step Size sub-VI Block Diagram where i is the scan measurement number (counter in the for-loop structure). The ΔI value is then divided by the motor step size input (advance per step), rounded to the nearest whole number, and enters the case structure that will add a step on the condition that the step equals 0 ("True") or allow the value to pass if it is greater than 0 ("False").

The number of steps is then auto-indexed out of the for-loop structure and creates a 1-D array of the steps required at each station. Other sub-VI outputs are found by the following additional steps. The total number of steps is the summation all the steps in the 1-D array, the individual movement length is the product of the 1-D array multiplied the motor step size input, and the total distance is found by multiplying both of these procedures. To find the scan positions, the individual movement length array enters another for-loop structure to that uses shift registers to add the distance intervals and give the position of the probe at a given a measurement reference number.

Frame 2: Initial Measurement Upstream

The next sequence is comprised of the *Initial Measurement Upstream* sub-VI, displayed in Figure A.11 with inputs and outputs. This sub-VI will wait for 0.5 seconds (Frame 2.0) then execute a series of commands that will measure the laboratory conditions, start the UEIDAQ session to read the hot-wire probe voltages, and concatenate the results into a summary file and single measurement file. A more detailed description of Frame 2.1 is displayed in Figure A.12 and is discussed in the following paragraphs.

On the left side of the sub-VI are the inputs including the *UeiDaq Refnum In* terminal for continuing the commands of the open session and links to the UEI UEIDAQ *Start Session* VI to begin the measurement process. The components inside the sequence structure can be categorized according to their location. The top-left area includes the two sub-VIs *Measure Lab* and *Measure UEI* that measure the laboratory conditions and the hot-wire probe voltages, respectively. Below those sub-VIs is the concatenation scheme for the single measurement point that includes the raw voltages of the hot-wire probes. Once the sub-VIs have completed execution, the data along and concatenated strings are merged into an array, configured to display 9 decimal places, and combined into another array of data including a time stamp and the positions of the hot-wire probes. It should be noted that since this is the initial measurement of the experiment, the hot-wire positions should be zero. Finally, the array is written, saved into a summary file that is configured to append new readings, and the session is stopped.

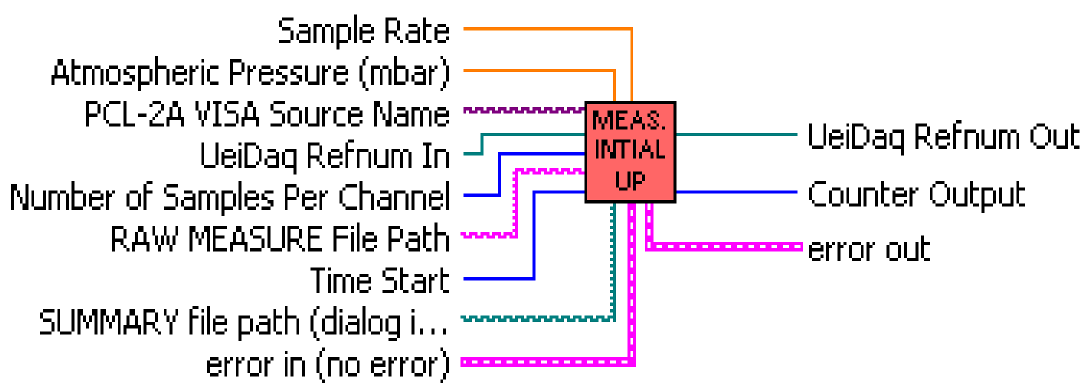

Figure A.11: Initial Measurement Upstream sub-VI

Measure Laboratory sub-VI. The *Measure Lab* sub-VI creates an output array with the following data: atmospheric pressure, relative humidity, free stream temperature, and dynamic pressure with their respective random uncertainties (expect for atmospheric pressure because of user-input). Displayed in Figure A.13, the relative humidity and freestream temperature are sampled by using the *AI Acquire Waveform* VI to access the DAQ device and input channels. The results of the output array flow into the *Mean &*

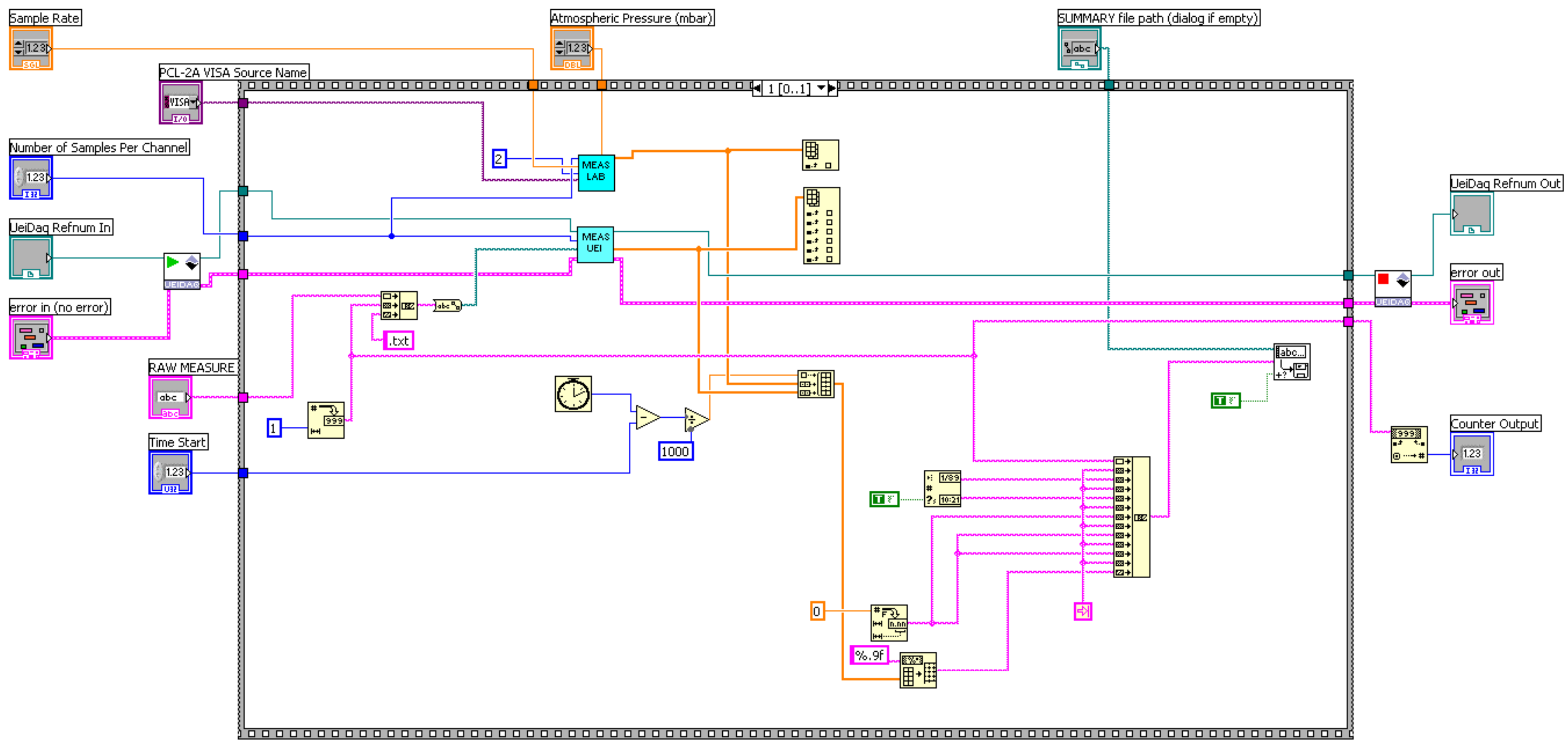

Figure A.12: Initial Measurement Upstream Block Diagram (Frame 2.1)

Uncertainty sub-VI that calculates the mean and random uncertainty of the measurements. Both of these values are transferred to their respective voltage conversion VIs that includes values and equations based on the calibration of the transducer.

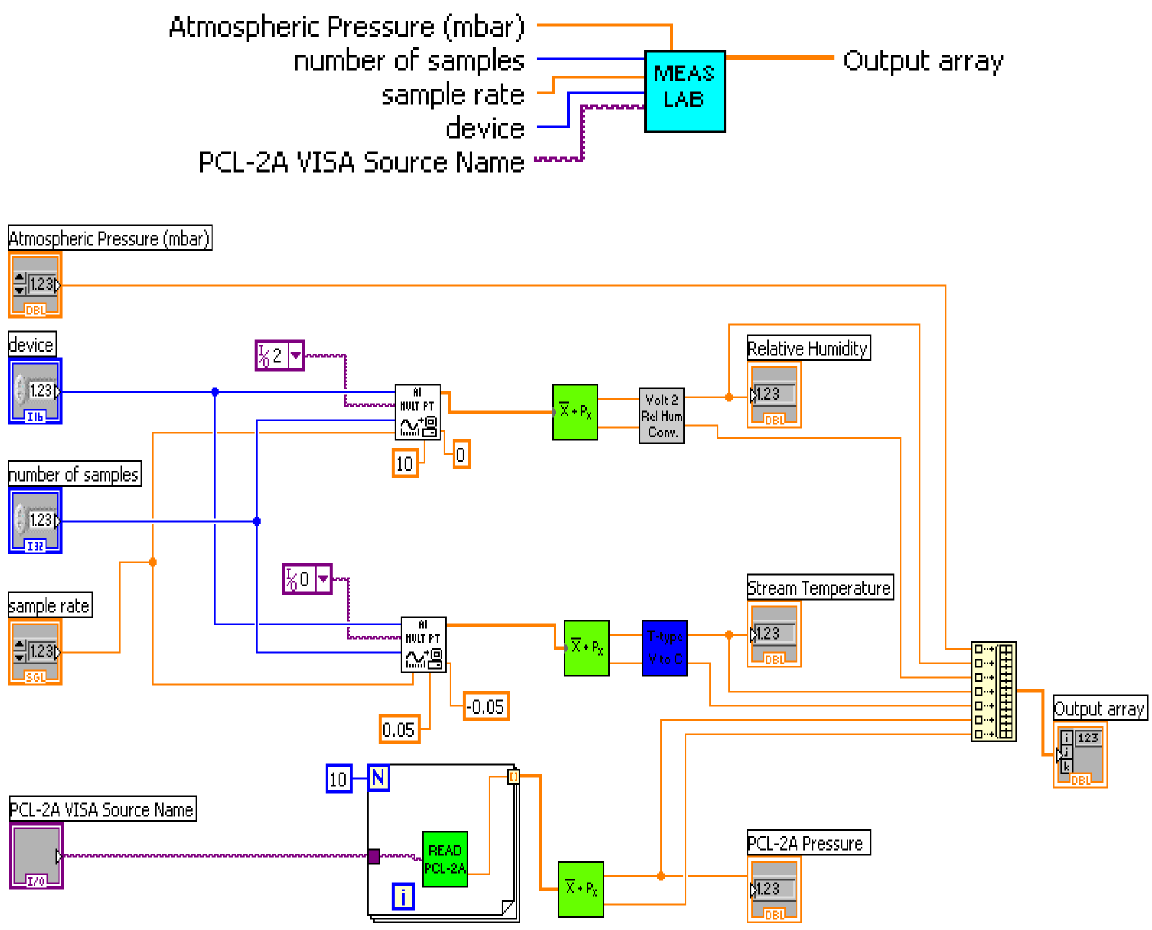

Figure A.13: Measure Laboratory VI and Block Diagram

The dynamic pressure input enters a for-loop structure into the *Read PCL-2A Dynamic Pressure* sub-VI, displayed in Figure A.14. In the top portion of the block diagram, the VISA VIs configure, write and read a buffer, and close the session. In the bottom, the buffer string is converted to a 2-D array of data with 8 decimal places and a comma as a delimiter. The data is then distributed into two different output arrays corresponding to the pressure transducer's channel inputs. This procedure will repeat 10 times within the for-loop structure and segue into the *Mean & Uncertainty* sub-VI. The statistics of these measurements are assembled into an output array that appends to the summary file.

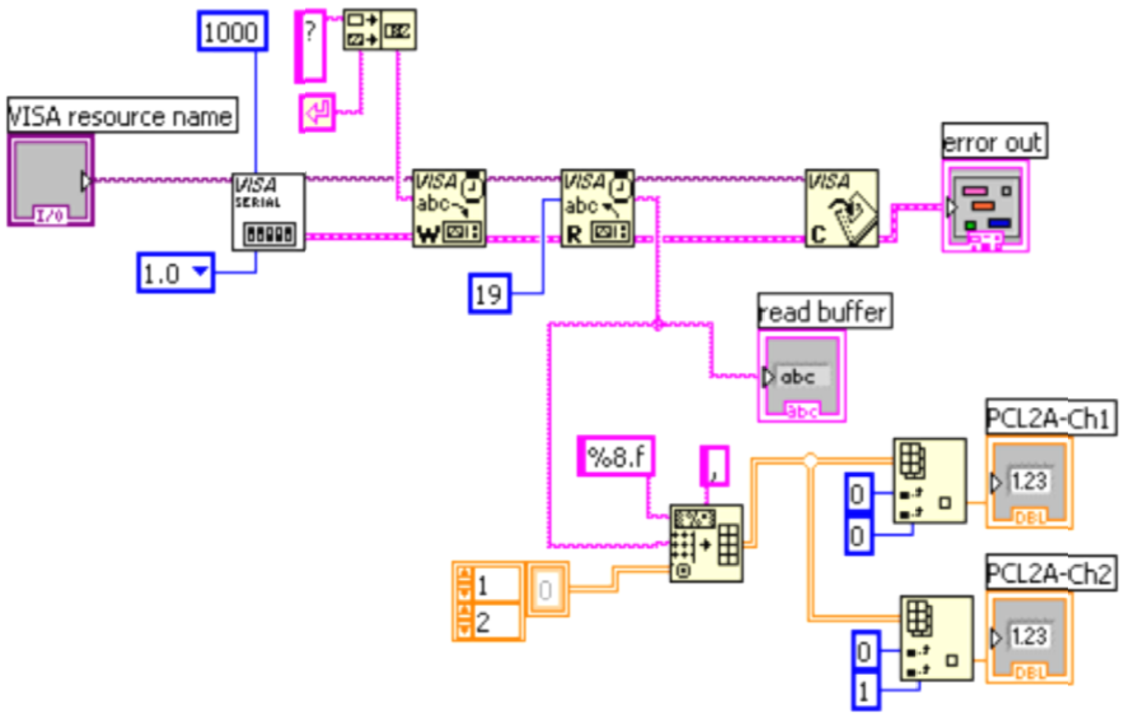

Figure A.14: Read PCL2A Dynamic Pressure Block Diagram

Measure UEI sub-VI. The *Measure UEI* sub-VI, shown in Figure A.15, contains the *UEIDAQ Read* VI that will scan the hot-wire probe voltages for the set amount of samples and return the data in 2-D array form. The data is saved into the measurement file and organized to four columns representing the channels of the probe. Similar to the lab measurements, enter the *Mean & Uncertainty* sub-VI for statistical analysis and summarized into an output array.

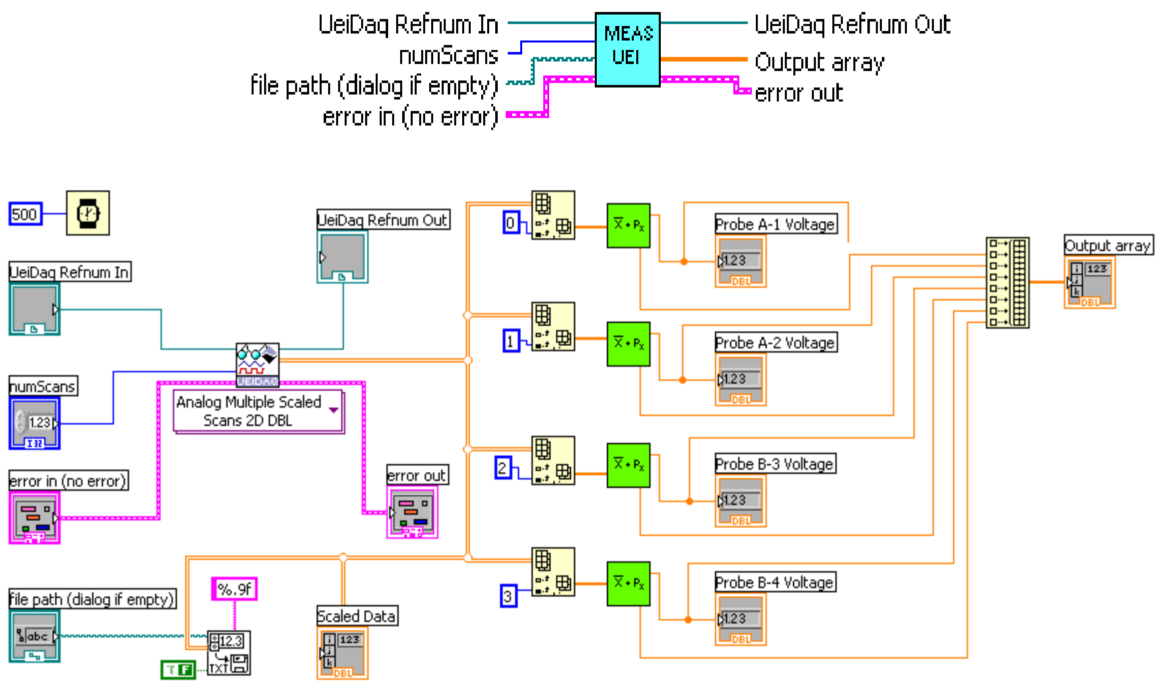

Figure A.15: Measure UEI VI and Block Diagram

Frame 3: Movement and Measurement Upstream

The third frame of the block diagram contains the *Move-Pause-Measure Upstream (MPM UP)* VI, shown in Figure A.16. This VI executes an iterative sequence of events, based on the number of scans set, that involves (1) moving the hot-wire probe, (2) wait for 3 seconds, and (3) a running measurement procedure similar to the *Initial Measurement Upstream* VI.

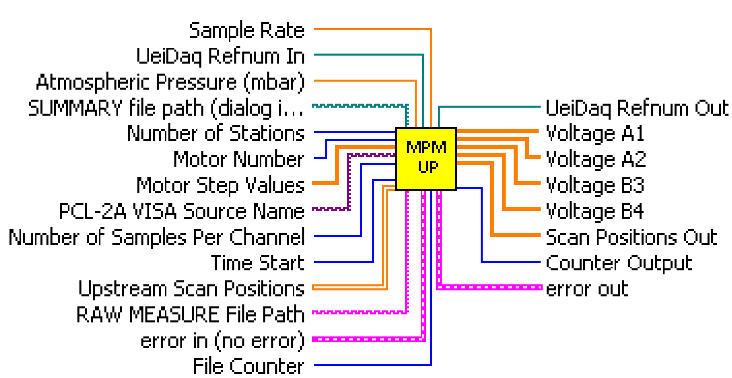

Figure A.16: Move, Pause, Measure Upstream VI Icon (Frame 3)

Move – Velmex Index Rotary Motor sub-VI. The first sequence of the *MPM UP* VI consists of the *Velmex Index Rotary Motor* sub-VI, shown in Figure A.17 that controls the *Velmex* Positioner system. Starting from the left of the sub-VI, the motor number and step value are formatted into strings and concatenated with other strings to communicate with the *Velmex* Positioners which motor active, the number of steps to move, and the rate of movement. The upper portion of the block diagram is used for moving the probes through the UniSlide and Bi Slide components. The lower portion of sub-VI code sets the rate of steps advancement per second. The first three sequences within the sub-VI (Frame 3.0.0-2) activate the connection with the *Velmex* Positioner, and send the string values for the rate of steps per second configuration. Then next two frames (Frames 3.0.3-4), divides the *step value* by the *degree/second* to find the amount of time to wait before executing the next sequence and wait an additional 0.75 seconds.

Measure – Modified Measurement VI Framework. The third sequence of the *MPM UP* VI is similar to the *Initial Measurement Upstream* VI with a few amendments, shown in Figure A.18. The sub-VIs and functions are enclosed in a for-loop structure that iterates the process for the set number of stations upstream. As described earlier in the Data Acquisition section, the UEIDAQ VIs are found inside the for-loop structure with shift registers to start, read, and stop the data flow for each measurement point. Additionally, new inputs include *File Counter* and *Upstream Scan Positions* with a set of functions that update the measurement file nomenclature and summary file data. The *MPM UP* VI runs until the set scan length has been achieved and the hot-wire probe will stay suspended at that position to allow for downstream measurements to occur without any unnecessary obstructions.

Frame 4: Downstream Measurements and Reset Positions

The downstream measurements are executed similarly to the upstream measurement with some VIs or VI code repeating. However, various positions across the test coupon are measured to create a grid of points. On the left side of Frame 4, displayed in Figure A.19, the *Auto Step Size* sub-VI is once again used to calculate the positions and distance intervals for the stations in the Y and Z-axis along with their respective advance per step values that are based on the UniSlide and Bi Slide positioning screw thread size. These values are transferred into another sequence frame structure that contains a for-loop structure that will iterate measurement and movement operations for the amount of Z-axis stations set minus one value (the last station in the Z-axis runs in a different sequence). In order to keep count of the measurement reference number, a set of VI operations and shift registers are used to create a conditional test. When the for-loop begins, the shift register is initialized to zero and is checked to see if the value matches. Thus, for the first iteration, the value is zero and the previous measurement count from the *Counter Output* (of the Upstream Measurements) passes through to the nested-sequence frame.

Downstream Measurements at Z-Stations (Frame 4.0.0-4). The first nested-sequence frame contains a block diagram similar to the Frame 2 and 3 with additional steps to return the probe to the absolute Y-axis position and move the hot-wire probe in the Z-direction, displayed in Figure A.20.

The first two frames contain the Initial Measurement Downstream and Move-Pause-Measure Downstream (MPM Down) VIs that are similar to those upstream measurements section, shown in Figure 20. However, both of these VIs contain

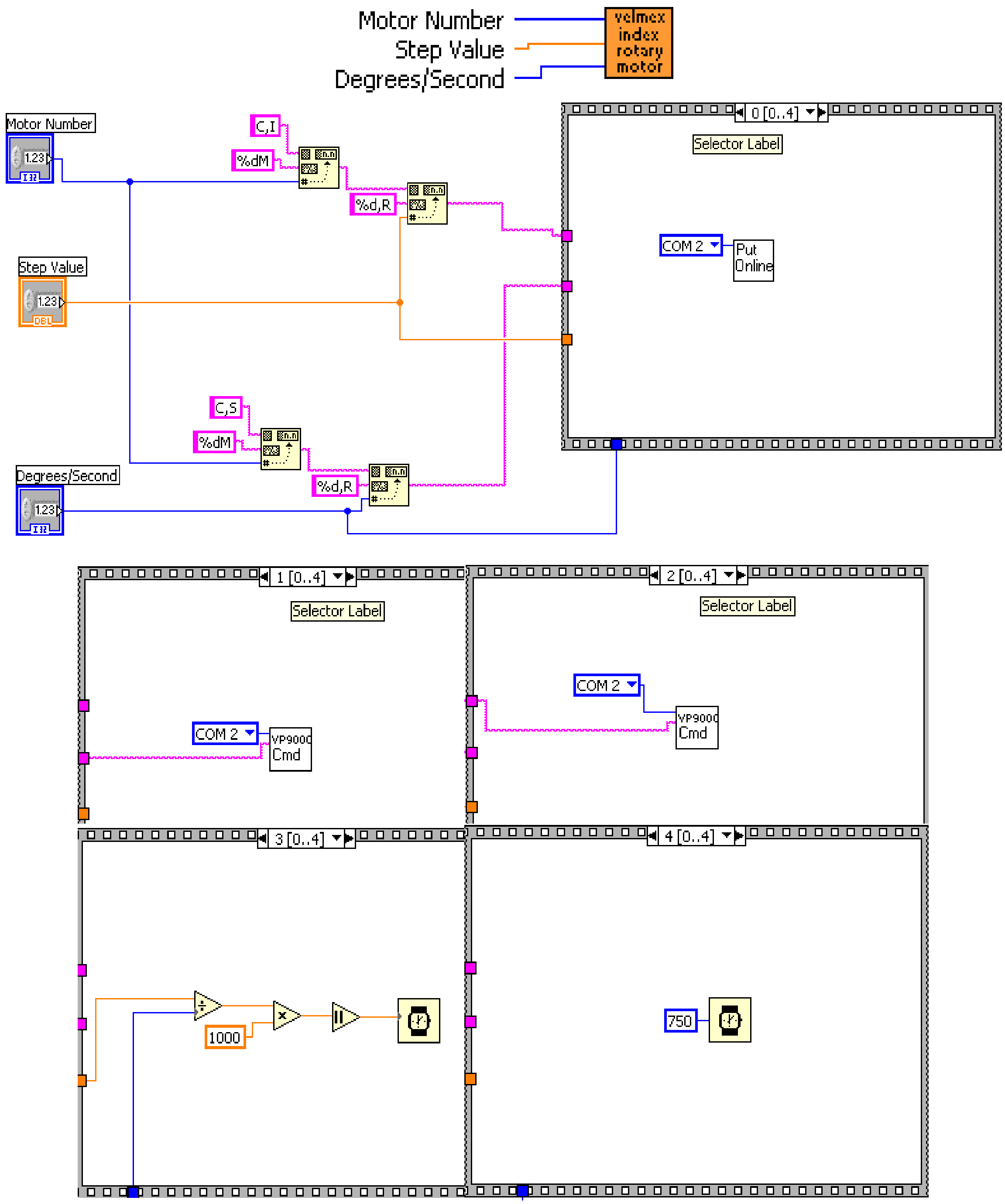

Figure A.17: Velmex Index (Rotary) Motor Movement sub-VI (Frame 3.0.0-4)

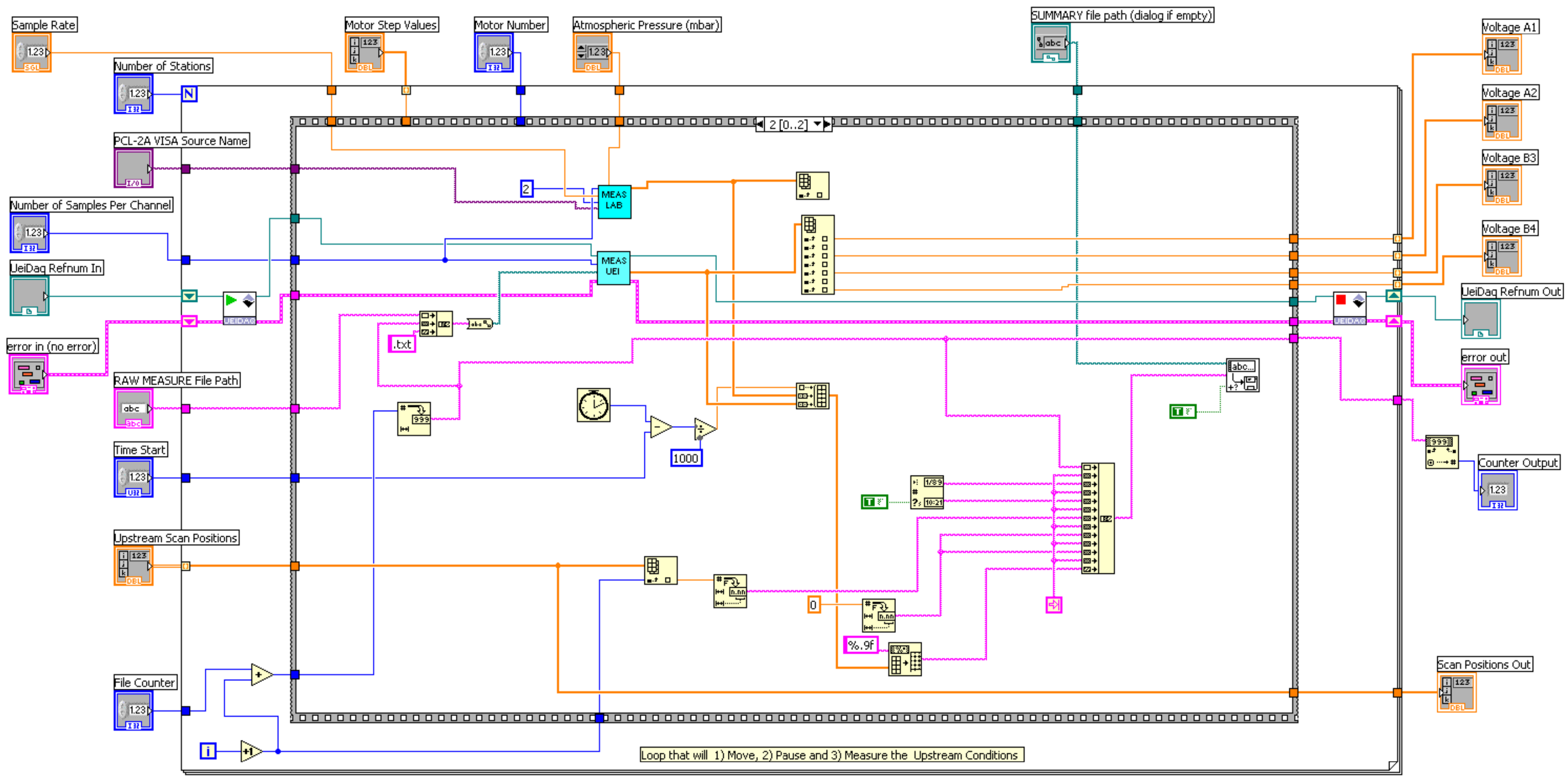

Figure A.18: MPM Up VI – Measurement Block Diagram (Frame 3.2) additional terminals and configuration to document the position of the hot-wire probe for a measurement. The Initial Measurement Downstream VI terminals Z-Station and Scan Positions Z enter an index array function to output the position of the probe. Additionally, the MPM Down VI includes these terminals along with Number of Stations in Y and Scan Positions Y to perform the same functions. The last three frames in Figure 20 will send the hot-wire probe down to the absolute position in the Y-axis with the *Velmex Index to ABS* VI, move the probe in the over to the next Z-axis station, and wait for one second before repeating the process. The VI icons and corresponding terminals for Frame 4.0 are displayed in Figure A.21

After the first iteration of the sequence, the shift register returns the new value from the *Counter Output* terminal and is not equal to zero (False). Thus, the value enters the *Counter Input* terminal of the *Initial Measurement Downstream* VI to continue keeping count of the measurement reference number. Once all the iterations have been completed, the *Counter Output* and *UeiDaq Ref Num* values are locally sequenced to the next frame (Frame 4.1).

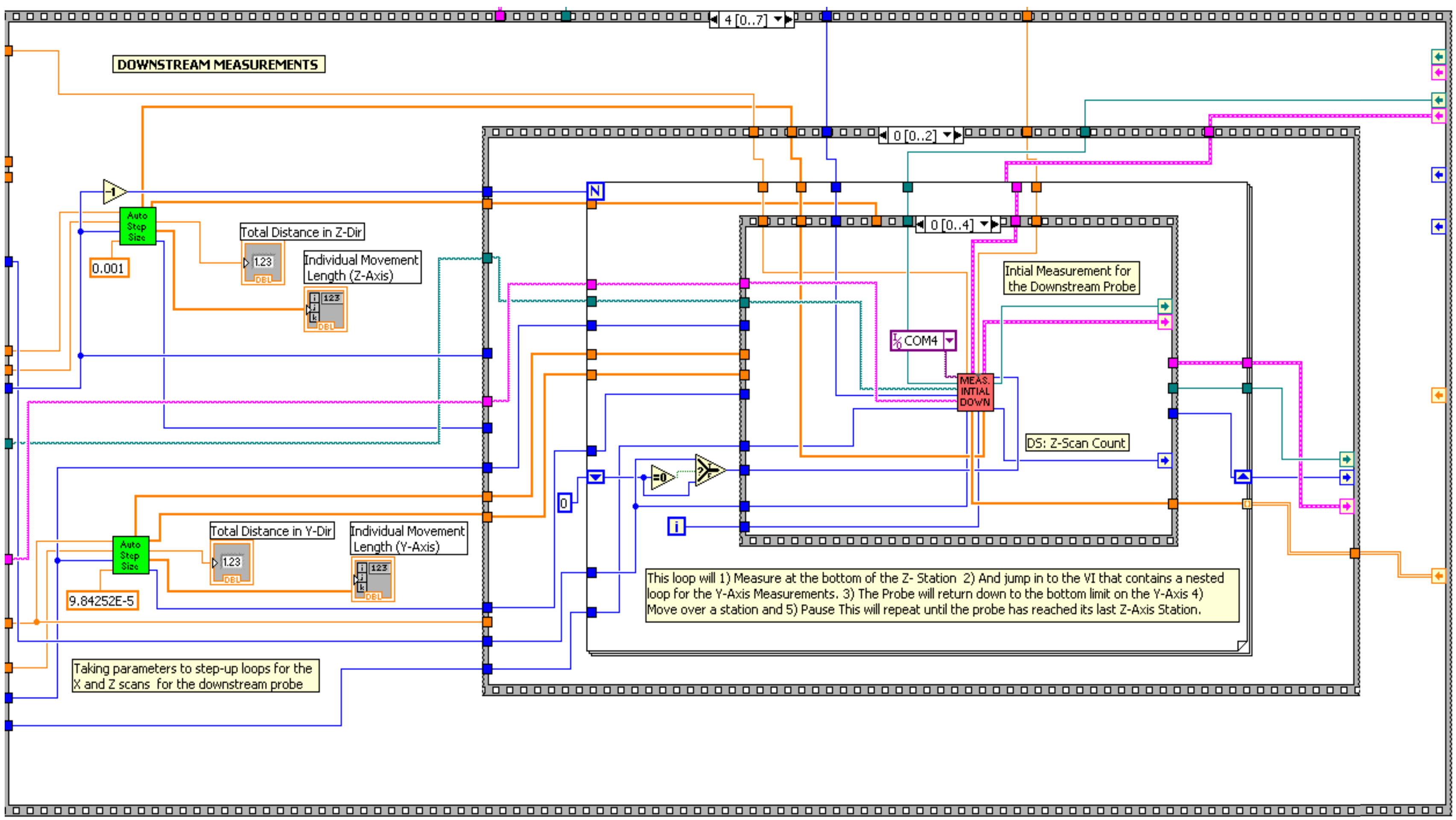

Figure A.19: Downstream Measurements Block Diagram (Frame 4)

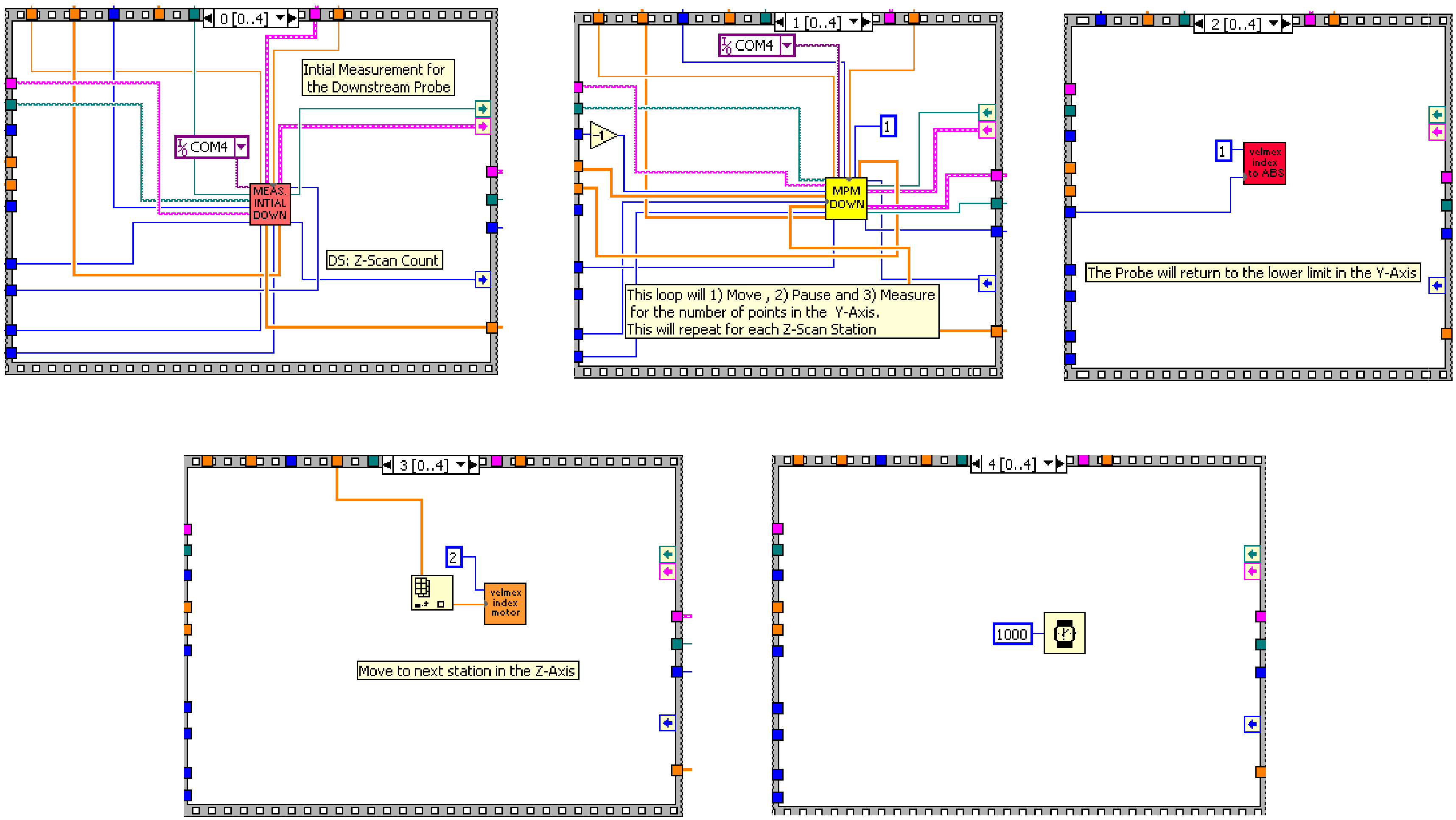

Figure A.20: Nested-Sequence of Downstream Measurements at Z-Stations

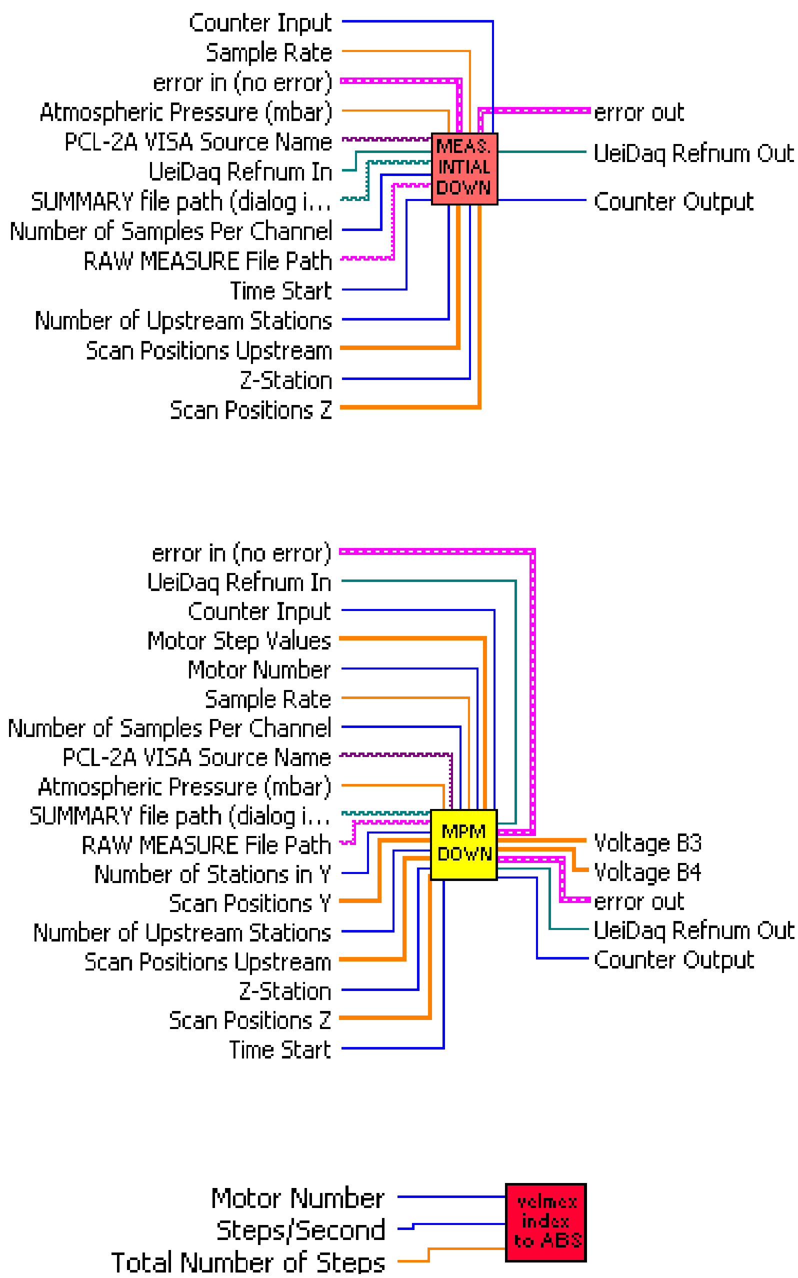

Figure A.21: Frame 4 VI Icons

Downstream Measurements at Last Z-Station (Frame 4.1.0-1). Within Frame 4.1 is another nested-sequence containing three frames at run only once to perform the last series of measurements at the final Z-station, displayed in Figure A.22. Compared to Frame 4.0.2.2, shown in Figure A.23, the structure names and order of the VIs are different, yet only the order of sequences is different within the VIs. The first frame contains the *Measure-Move-Pause Downstream (MMP Down)* VI that has the same sequence frames and terminals as the *MPM UP* VI, only now the measurement occurs first, then is followed by the positioning of the probe and wait sequence. This frame will run until the probe has reached the last position set by the scan length and will segue into Frame 4.1.1, where the last measurement is taken and the UEIDAQ session is destroyed.

Frame 4.1.2- Frame 7: Reset Positions and Shut-Down

The next two sequences, Frame 4.1.2 and Frame 4.2, are displayed in Figure A.24 and reset the probe positions back to the absolute positions in the Y and Z axis, respectively. Additionally, last frames of the program, displayed in Figure A.25, reset the upstream probe back to the absolute position and wait 5 seconds before disconnecting the control over the stepper motors in the *Velmex Positioners* to finish the experiment and program.

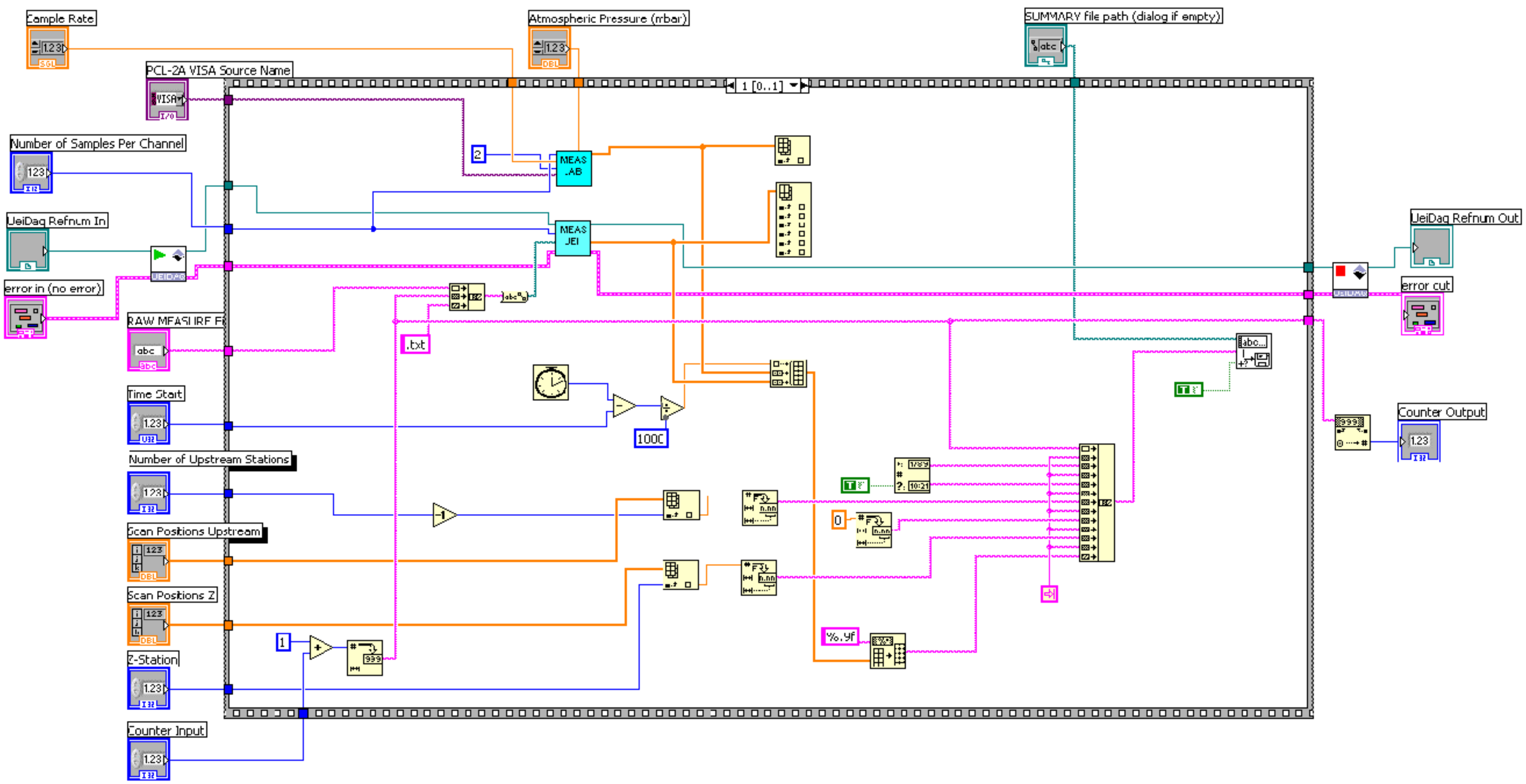

Figure A.22: Initial Measurement Downstream Block Diagram

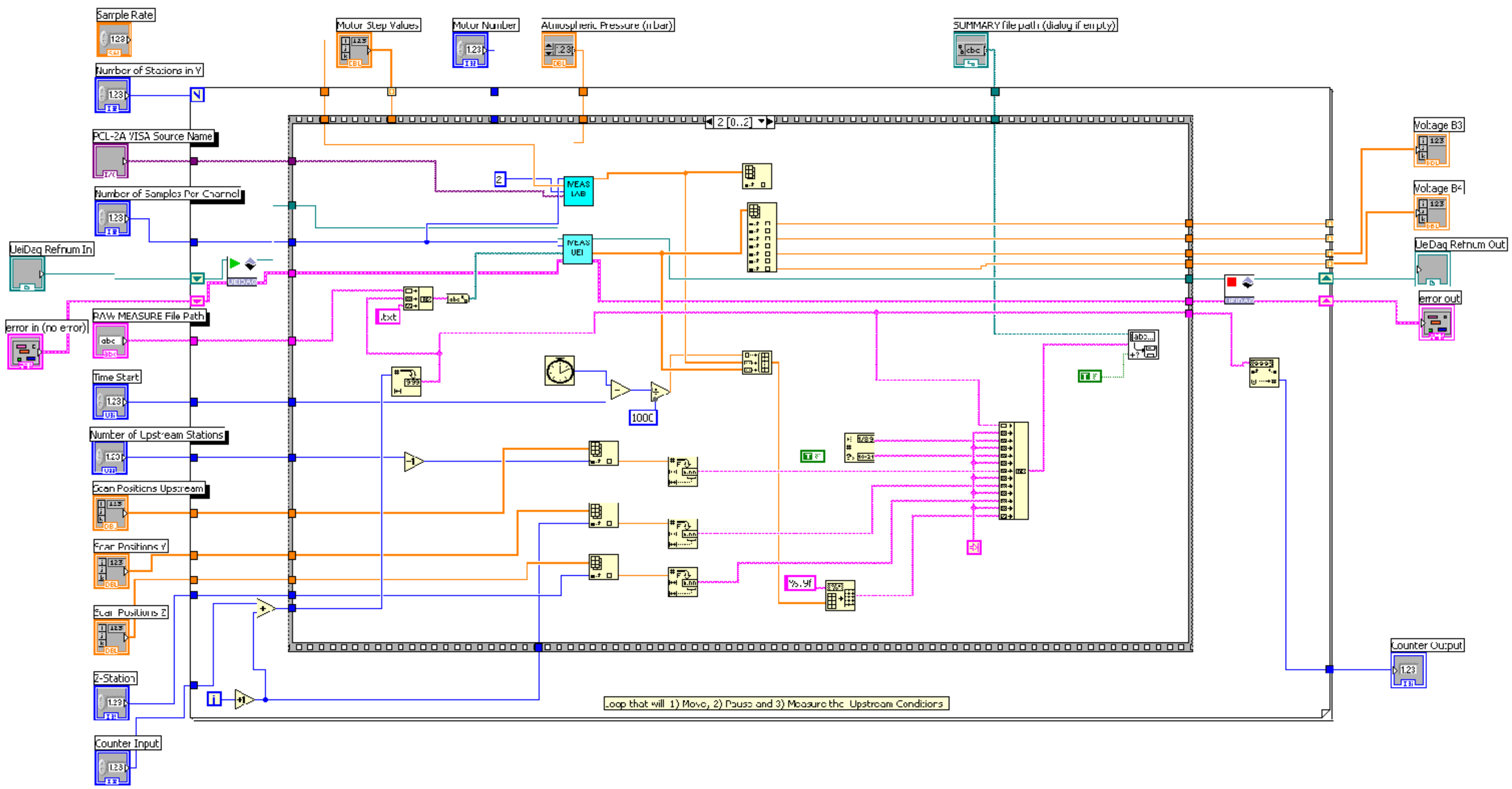

Figure A.23: MPM Down VI – Measurement Block Diagram (Frame 4.0.2.2)

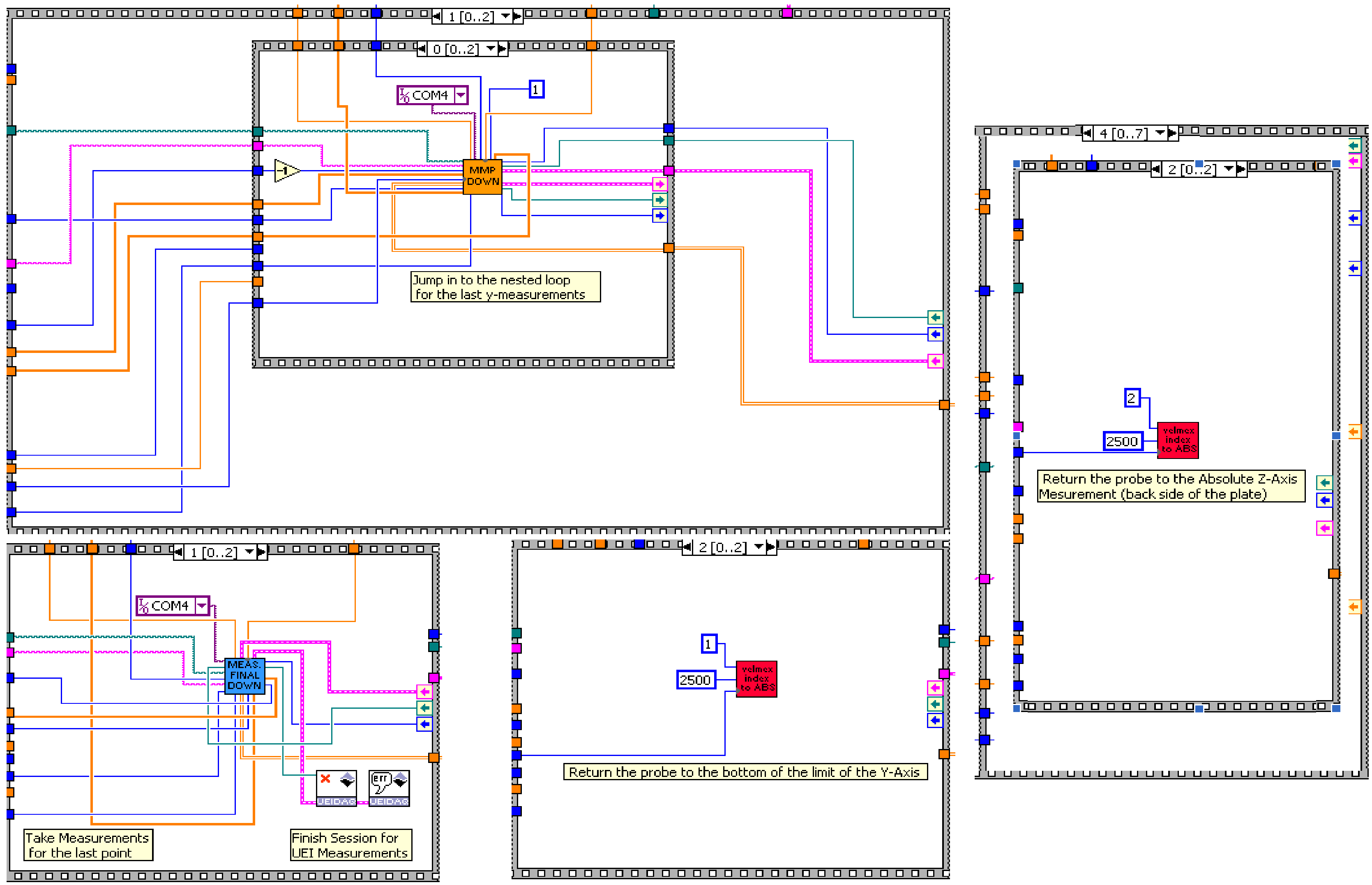

Figure A.24: Sequences for Last Z-Station Measurements (Frames 4.1-4.2)

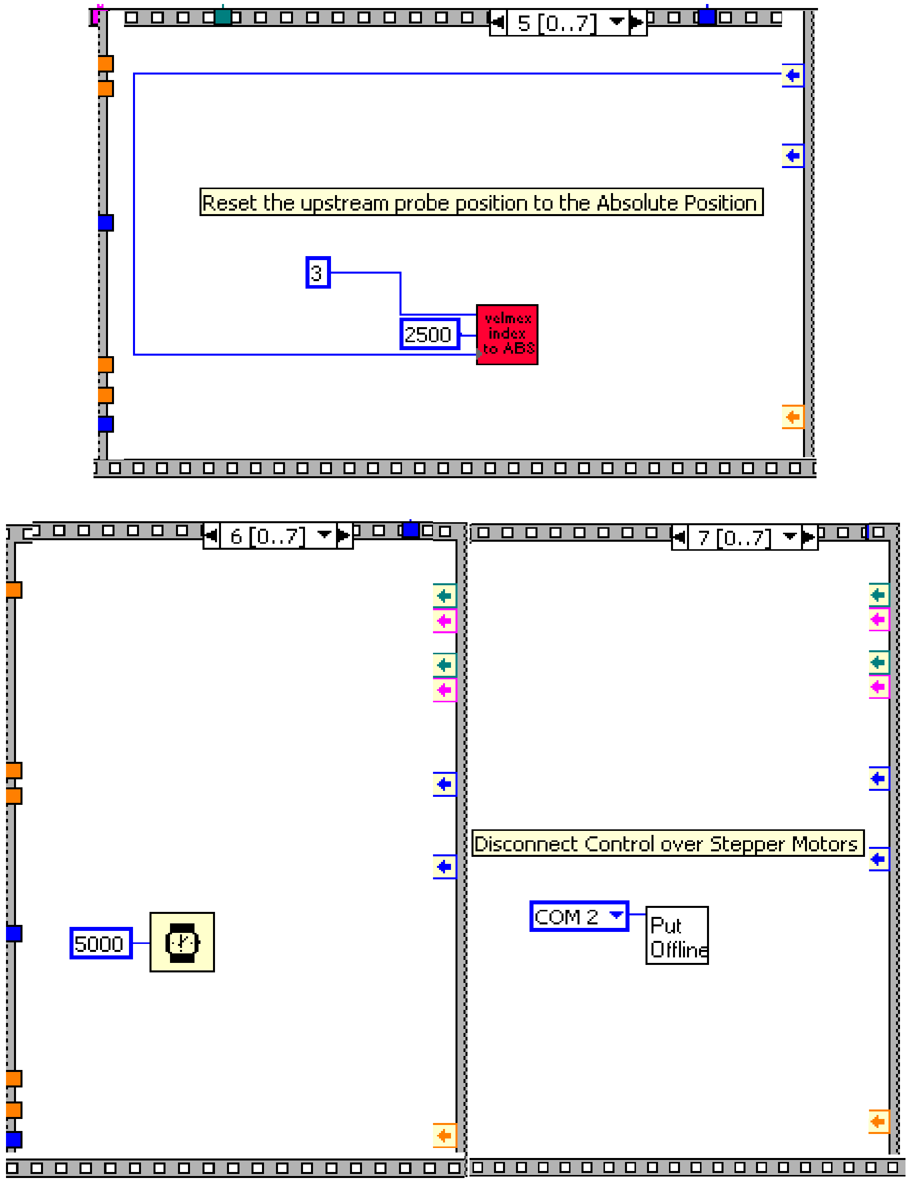

Figure A.25: Reset Upstream Probe Position and Disconnect Motor Control

APPENDIX B

Sample Uncertainty Analysis

The uncertainty analysis is for one velocity (10 m/s) measurement

Instrument Uncertainties	$i := 49$
Temperature (T-Type Thermocouple)	$B\_T_c := 1K$
Dynamic Pressure (PCL2A w/ Pitot Static tube)	$B\_\Delta P_{P2a} := (1 \cdot in\_H2O \cdot 0.06\%) = 0.149Pa$
Atm Pressure (Barometer)	$B\_P_{atm} := 0.001bar = 100Pa$
Relative Humidity (Siemens)	$B\_\phi := 0.2 \cdot \_\phi_i = 0.119$

To calculate the experimental uncertainty, the following equation was used based on the Kline and McClintock method:

$$U_R = \left(B_R^{\ 2} + t \cdot S_R^{\ 2}\right)^{\frac{1}{2}}$$

where
$$B_R = \left[\left[\left(\frac{\partial}{\partial x_1} R\right) \cdot B_1\right]^2 + \left[\left(\frac{\partial}{\partial x_2} R\right) \cdot B_2\right]^2 .. \left[\left(\frac{\partial}{\partial x_n} R\right) \cdot B_n\right]^2\right]$$

and
$$S_R = \left[\left[\left(\frac{\partial}{\partial x_1} R\right) \cdot S_1\right]^2 + \left[\left(\frac{\partial}{\partial x_2} R\right) \cdot S_2\right]^2 .. \left[\left(\frac{\partial}{\partial x_n} S\right) \cdot \sigma_n\right]^2\right]$$

where R is a function of the 'n' independent variables $R=R(x_1,x_2,...,x_n)$

B is the fixed or instrument uncertainty

S is the standard deviation of the samples taken

t is the Student's t multiplier for 95%

The Random Uncertainties have been calculated throughout the LabVIEW program for the raw measurement files that include the sensor voltages and the lab conditions (with 200,000 samples for a measurement). However, the fixed uncertainty errors still need to be calculated and are addressed according to the DANTEC guidelines

Calibration

This defines the accuracy of the lab equipment used to measure the atmospheric and freestream settings.

Density:

$$\rho_{ma} := \left(\frac{P_{atm} - \phi \cdot Psat\_T_{H2O}(T_c)}{\frac{R_u}{M_{air}} \cdot T_c} + v\_TP_{H2O}(T_c, \phi \cdot Psat\_T_{H2O}(T_c)) \right)^{-1} = 1.198 \frac{kg}{m^3}$$

Derivative with respect to Atmospheric Pressure

$$\rho d\_P_{atm} := \left[\frac{\partial}{\partial P_{atm}} \left(\frac{P_{atm} - \phi \cdot Psat\_T_{H2O}(T_c)}{\frac{R_u}{M_{air}} \cdot T_c} + v\_TP_{H2O}(T_c, \phi \cdot Psat\_T_{H2O}(T_c))^{-1} \right) \right]$$

Derivative with respect to Relative Humidity

$$\rho d\_\phi := \left[\frac{\partial}{\partial \phi} \left(\frac{P_{atm} - \phi \cdot Psat\_T_{H2O}(T_c)}{\frac{R_u}{M_{air}} \cdot T_c} + v\_TP_{H2O}(T_c, \phi \cdot Psat\_T_{H2O}(T_c))^{-1} \right) \right]$$

Derivative with respect to Freestream Temperature

$$\rho d\_T_c := \left[\frac{\partial}{\partial T_c} \left(\frac{P_{atm} - \phi \cdot Psat\_T_{H2O}(T_c)}{\frac{R_u}{M_{air}} \cdot T_c} + v\_TP_{H2O}(T_c, \phi \cdot Psat\_T_{H2O}(T_c))^{-1} \right) \right]$$

Density Uncertainty

$$B\_\rho_{ma} := \left[(\rho d\_P_{atm} \cdot B\_P_{atm})^2 + (\rho d\_\phi \cdot B\_\phi)^2 + (\rho d\_T_c \cdot B\_T_c)^2 \right]^{\frac{1}{2}} = 4.802 \times 10^{-3} \frac{kg}{m^3}$$

$$t\_S\_\rho_{ma} := \left[(\rho d\_\phi \cdot S\_\phi)^2 + (\rho d\_T_c \cdot S\_T_c)^2 \right]^{\frac{1}{2}} = 2.06 \times 10^{-4} \frac{kg}{m^3}$$

$$U\_\rho_{ma} := \left(B\_\rho_{ma}{}^2 + t\_S\_\rho_{ma}{}^2 \right)^{\frac{1}{2}} = 4.807 \times 10^{-3} \frac{kg}{m^3}$$

$$\frac{U\_\rho_{ma}}{\rho_{ma}} = 0.401 \cdot \%$$

Velocity from Pitot-Static Reference:

$$V_N := \sqrt{\frac{2 \cdot \Delta P_{P2a}}{\rho_{ma}}} = 10.043 \frac{m}{s}$$

Derivative with respect to Density

$$V\_d\rho_{ma} := \frac{\partial}{\partial \rho_{ma}} \left(\sqrt{\frac{2 \cdot \Delta P_{P2a}}{\rho_{ma}}} \right)$$

Derivative with respect to Density

$$V\_d\Delta P_{P2a} := \frac{\partial}{\partial \Delta P_{P2a}} \left(\sqrt{\frac{2 \cdot \Delta P_{P2a}}{\rho_{ma}}} \right)$$

Velocity from Pitot-Static Reference Uncertainty

$$B\_V_N := \left[\left(V\_d\rho_{ma} \cdot B\_\rho_{ma} \right)^2 + \left(V\_d\Delta P_{P2a} \cdot B\_\Delta P_{P2a} \right)^2 \right]^{\frac{1}{2}} = 0.024 \frac{m}{s}$$

$$t\_S\_V_N := \left[\left(V\_d\rho_{ma} \cdot t\_S\_\rho_{ma} \right)^2 + \left(V\_d\Delta P_{P2a} \cdot S\_\Delta P \right)^2 \right]^{\frac{1}{2}} = 1.065 \times 10^{-3} \frac{m}{s}$$

$$U\_V_N := \left(B\_V_N{}^2 + t\_S\_V_N{}^2 \right)^{\frac{1}{2}} = 0.024 \frac{m}{s}$$

$$\frac{U\_V_N}{V_N} = 0.236\%$$

Linearization

The linearization for each wire on the probe is estimated by the standard deviation of the curve fitting errors in the calibration points and the random uncertainties from the voltages measured.

The 9th-order Polynomial function that estimates the calibration data is shown below

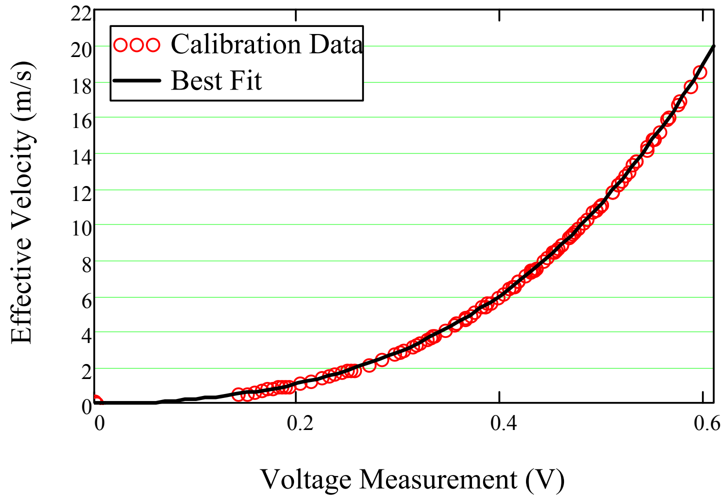

where $Vel_{B1} := VelE_{PBC3}(VP1)$ is the Velocity given by the Polynomial Function (Best Fit) and is also the effective velocity for later

Vel_{CD1} is the Velocity from the Calibration Data

$j := 0, 1 .. 107$ is the number of calibration points

S_VP1 is the random uncertainty of the voltages acquired

Then the standard deviation of the curve fitting errors is suggested for uncertainty and given by

$$Vel\_std1_j := \text{stdev}\left(Vel_{B1_j}, Vel_{CD1_j}\right) \cdot \frac{m}{s}$$

and the average of standard deviation of the points and Pearson's r correlation is

$$Vel\_avg\_std1 := \frac{\sum_j Vel\_std1_j}{107} = 0.012 \frac{m}{s}$$

$$Lin1_{Pearson} := \text{corr}\left(Vel_{BF1}, Vel_{CD1}\right) = 0.999981$$

$$B\_Lin1 := Vel\_avg\_std1 \qquad \frac{B\_Lin1}{V_N} = 0.119\%$$

For the other wire

$$Vel_{B2} := VelE_{PBC4}(VP2) \qquad Vel\_std2_j := \text{stdev}\left(Vel_{B2_j}, Vel_{CD2_j}\right) \cdot \frac{m}{s}$$

$$Vel\_avg\_std2 := \frac{\sum_j Vel\_std2_j}{107} = 0.152 \frac{m}{s}$$

$$Lin2_{Pearson} := \text{corr}\left(Vel_{BF2}, Vel_{CD2}\right) = 0.999195$$

$$B\_Lin2 := Vel\_avg\_std2 \qquad \frac{B\_Lin2}{V_N} = 1.509\%$$

Data Acquisition

Note that is separate from the other variables taken earlier using the Kline & McClintock method and this is only for one wire in the probe. Similarly, the uncertainty related to the Data Acquisition is related to the the A/D Board resolution and given below

$$B\_E_{range} := \frac{E_{AD}}{2^n}$$

$n := 16$ number of bits

$E_{AD} = 10\,V$ A/D Board input range

$$B_{DAQ} := B\_E_{range} \cdot \left(UE_{Slope}\right)$$

UE_{Slope} slope of inverse calibration curve (Sensitivity Factor)

$$B_{DAQ} = 9.431 \times 10^{-4}\,\frac{m}{s}$$

$$\frac{B_{DAQ}}{V_N} = 9.391 \times 10^{-3} \cdot \%$$

Error Propagation

The fixed errors from the calibration to DAQ portion will be propagated into the Experimental section as fixed uncertainties of the Calibrated Velocities shown below

$$B\_Vel_{BFC1} := B\_V_N + B\_Lin1 + B_{DAQ} = 0.037\frac{m}{s}$$

$$B\_Vel_{BFC2} := B\_V_N + B\_Lin2 + B_{DAQ} = 0.176\frac{m}{s}$$

Additionally, the random uncertainties of the calibration equipment and linearization of the voltages to velocity is given below and propagates to the experimental uncertainties as well.

$$t\_S\_Vel_{BFC1} := VelE_{PBC3}\left(\frac{S\_VP1}{V}\right) \cdot \frac{m}{s} + t\_S\_V_N = 0.033\frac{m}{s}$$

$$t\_S\_Vel_{BFC2} := VelE_{PBC4}\left(\frac{S\_VP2}{V}\right) \cdot \frac{m}{s} + t\_S\_V_N = 0.032\frac{m}{s}$$

Below is the total uncertainty from the calibration and linearization for each of the wires and in total.

$$U\_lin\_cal\_1 := \sqrt{B\_Vel_{BFC1}^{\;2} + t\_S\_Vel_{BFC1}^{\;2}} = 0.049\frac{m}{s} \qquad \frac{U\_lin\_cal\_1}{V_N} = 0.488\%$$

$$U\_lin\_cal\_2 := \sqrt{B\_Vel_{BFC2}^{\;2} + t\_S\_Vel_{BFC2}^{\;2}} = 0.179\frac{m}{s} \qquad \frac{U\_lin\_cal\_2}{V_N} = 1.783\%$$

$$U\_total\_lin\_cal := \sqrt{\left(\frac{U\_lin\_cal\_1}{V_N}\right)^2 + \left(\frac{U\_lin\_cal\_2}{V_N}\right)^2} = 1.848\%$$

Other uncertainties that need to be accounted for dealing with the velocity occur within the decomposition of the velocity components and velocity measurements with the temperature correction, linearization, and density in the experiment accounted for.

Temperature Correction Coefficient

$$C_{Ecorr} := \left(\frac{T_s - Tm_c}{T_s - T_e}\right)^{\frac{1}{2}} = 1.001$$

where

C_{Ecorr}	is the temperature correction coefficient for the voltages
$T_s = 523.15K$	is the sensor wire temperature
$T_e := 294K$	is the ambient temperature during DAQ
T_{mc}	is ambient temperature from last set-up
$B\_T_s := 0.5K$	is the temperature uncertainty of the sensor [DANTEC]

Derivative with respect to temperatures and acquired voltage

$$C_{Ecorr\_dT.s} := \frac{\partial}{\partial T_s}\left[\left(\frac{T_s - Tm_c}{T_s - T_e}\right)^{\frac{1}{2}}\right] \qquad C_{Ecorr\_dTm.c} := \frac{\partial}{\partial Tm_c}\left[\left(\frac{T_s - Tm_c}{T_s - T_e}\right)^{\frac{1}{2}}\right]$$

$$C_{Ecorr\_dT.e} := \frac{\partial}{\partial T_s}\left[\left(\frac{T_s - Tm_c}{T_s - T_e}\right)^{\frac{1}{2}}\right]$$

$$B\_C_{Ecorr} := \left[\left(C_{Ecorr\_dT.s} \cdot B\_T_s\right)^2 + \left(C_{Ecorr\_dT.e} \cdot B\_T_c\right)^2 \ldots + \left[\left(C_{Ecorr\_dTm.c} \cdot B\_T_c\right)^2\right]\right]^{\frac{1}{2}} = 2.18 \times 10^{-3}$$

Random Uncertainty of Sensor Temperature not counted

$$t\_S\_C_{Ecorr} := \left[\left(C_{Ecorr\_dT.e} \cdot S\_T_c\right)^2 + \left(C_{Ecorr\_dTm.c} \cdot S\_T_c\right)^2\right]^{\frac{1}{2}} = 1.003 \times 10^{-4}$$

$$U\_C_{Ecorr} := \left(B\_C_{Ecorr}{}^2 + t\_S\_C_{Ecorr}{}^2\right)^{\frac{1}{2}} = 2.182 \times 10^{-3}$$

Decomposition into Velocity Components

The uncertainty from the calibration portion also applies to the experimental

Given the following measurement from a point in the Freestream, the voltages and their uncertainties:

The Experimental Velocities and their uncertainties (including calibration and linearization)

$$Vel_{BFC1} := VelE_{PBC3}(VP\_1 \cdot C_{Ecorr}) \qquad Vel_{BFC2} := VelE_{PBC4}(VP\_2 \cdot C_{Ecorr})$$

$$B\_Vel_{BFC1} = 0.037\frac{m}{s} \qquad B\_Vel_{BFC2} = 0.176\frac{m}{s}$$

$$t\_S\_Vel_{BFC1} = 0.033\frac{m}{s} \qquad t\_S\_Vel_{BFC2} = 0.032\frac{m}{s}$$

Pressure Variations with density are the same as previous uncertainty analysis for density with change in temperature and humidity.

$$\rho_e := \frac{P_{atm} - \phi \cdot Psat\_T_{H2O}(T_e)}{\frac{R_u}{M_{air}} \cdot T_c} + v\_TP_{H2O}(T_c, \phi \cdot Psat\_T_{H2O}(T_e))^{-1} = 1.198\frac{kg}{m^3}$$

Uncertainty in Effective Velocities

$$u_{d1} := \left[\frac{Vel_{BFC1}^{\ 2} - (k_1 \cdot Vel_{BFC2})^2}{1 - k_1^{\ 2} \cdot k_2^{\ 2}}\right]^{\frac{1}{2}} \cdot \frac{m}{s} = 6.378\frac{m}{s}$$

"Normal Directional Velocity" ($Ueff_1$) without Pressure Variation

$$u_1 = u_d \cdot \left(\frac{\rho_{ma}}{\rho_e}\right)$$

Normal Directional Velocity with Pressure Variation

$$u_1 := \left[\frac{VelE_{PBC3}(VP\_1 \cdot C_{Ecorr})^2 - (k_1 \cdot VelE_{PBC4}(VP\_2 \cdot C_{Ecorr}))^2}{1 - k_1^{\ 2} \cdot k_2^{\ 2}}\right]^{\frac{1}{2}} \cdot \frac{\rho_{ma}}{\rho_e} \cdot \frac{m}{s} = 6.379\frac{m}{s}$$

Derivative with respect to Temperature Correction (Overheat)

$$u1\_dC_{Ecorr} := \frac{\partial}{\partial C_{Ecorr}}\left[\left[\frac{VelE_{PBC3}(VP\_1 \cdot C_{Ecorr})^2 - (k_1 \cdot VelE_{PBC4}(VP\_2 \cdot C_{Ecorr}))^2}{1 - k_1^2 \cdot k_2^2}\right]^{\frac{1}{2}} \cdot \frac{\rho_{ma}}{\rho_e}\right]$$

Derivative with respect to average density

$$u1\_d\rho_{ma} := \frac{\partial}{\partial \rho_{ma}}\left[\left[\frac{VelE_{PBC3}(VP\_1 \cdot C_{Ecorr})^2 - (k_1 \cdot VelE_{PBC4}(VP\_2 \cdot C_{Ecorr}))^2}{1 - k_1^2 \cdot k_2^2}\right]^{\frac{1}{2}} \cdot \frac{\rho_{ma}}{\rho_e}\right]$$

Derivative with respect to one sample density

$$u1\_d\rho_{e} := \frac{\partial}{\partial \rho_{e}}\left[\left[\frac{VelE_{PBC3}(VP\_1 \cdot C_{Ecorr})^2 - (k_1 \cdot VelE_{PBC4}(VP\_2 \cdot C_{Ecorr}))^2}{1 - k_1^2 \cdot k_2^2}\right]^{\frac{1}{2}} \cdot \frac{\rho_{ma}}{\rho_e}\right]$$

Derivative with respect to Calibration Velocity from wire 1

$$u1\_dVel_{BFC1} := \frac{\partial}{\partial Vel_{BFC1}}\left[\left[\left[\frac{Vel_{BFC1}{}^2 - (k_1 \cdot Vel_{BFC2})^2}{1 - k_1^2 \cdot k_2^2}\right]^{\frac{1}{2}} \cdot \frac{\rho_{ma}}{\rho_e}\right] \cdot \frac{s}{m}\right]$$

Derivative with respect to Calibration Velocity from wire 2

$$u1\_dVel_{BFC2} := \frac{\partial}{\partial Vel_{BFC2}}\left[\left[\frac{Vel_{BFC1}{}^2 - (k_1 \cdot Vel_{BFC2})^2}{1 - k_1^2 \cdot k_2^2}\right]^{\frac{1}{2}} \cdot \frac{\rho_{ma}}{\rho_e}\right] \cdot \frac{s}{m}$$

Uncertainty for Normal Direction Velocity

$$B\_u_1 := \left[\left(u1\_dC_{Ecorr} \cdot B\_C_{Ecorr}\right)^2 + \left(u1\_d\rho_{ma} \cdot B\_\rho_{ma}\right)^2 + \left(u1\_d\rho_e \cdot B\_\rho_{ma}\right)^2 \ldots \atop + \left(u1\_dVel_{BFC1} \cdot B\_Vel_{BFC1}\right)^2 + \left(u1\_dVel_{BFC2} \cdot B\_Vel_{BFC2}\right)^2\right]^{\frac{1}{2}} = 0.064$$

$$t\_S\_u_1 := \left[\left(u1\_dC_{Ecorr} \cdot t\_S\_C_{Ecorr}\right)^2 + \left(u1\_d\rho_{ma} \cdot B\_\rho_{ma}\right)^2 + \left(u1\_d\rho_e \cdot B\_\rho_{ma}\right)^2 \ldots \atop + \left(u1\_dVel_{BFC1} \cdot t\_S\_Vel_{BFC1}\right)^2 + \left(u1\_dVel_{BFC2} \cdot t\_S\_Vel_{BFC2}\right)^2\right]^{\frac{1}{2}} = 0.049$$

$$U\_u_1 := \left(B\_u_1{}^2 + t\_S\_u_1{}^2\right)^{\frac{1}{2}} \cdot \frac{m}{s} = 0.081\frac{m}{s}$$

$$\frac{U\_u_1}{u_1} = 1.262\cdot\%$$

The same is repeated for the "Tangential Direction Velocity" ($Ueff_2$) and is executed below

$$u_{d2} := \left[\frac{Vel_{BFC2}{}^2 - \left(k_2 \cdot Vel_{BFC1}\right)^2}{1 - k_1{}^2 \cdot k_2{}^2}\right]^{\frac{1}{2}} \cdot \frac{m}{s} = 7.839\frac{m}{s}$$

Tangential Directional Velocity without Pressure Variation

$$u_2 = u_{d2} \cdot \left(\frac{\rho_{ma}}{\rho_e}\right)$$

Tangential Directional Velocity with Pressure Variation

$$u_2 := \left[\frac{VelE_{PBC4}\left(VP\_2 \cdot C_{Ecorr}\right)^2 - \left(k_2 \cdot VelE_{PBC3}\left(VP\_1 \cdot C_{Ecorr}\right)\right)^2}{1 - k_1{}^2 \cdot k_2{}^2}\right]^{\frac{1}{2}} \cdot \frac{\rho_{ma}}{\rho_e} \cdot \frac{m}{s} = 7.84\frac{m}{s}$$

Derivative with respect to Temperature Correction (Overheat)

$$u2\_dC_{Ecorr1} := \frac{\partial}{\partial C_{Ecorr}}\left[\left[\frac{VelE_{PBC4}\left(VP\_2 \cdot C_{Ecorr}\right)^2 - \left(k_2 \cdot VelE_{PBC3}\left(VP\_1 \cdot C_{Ecorr}\right)\right)^2}{1 - k_1{}^2 \cdot k_2{}^2}\right]^{\frac{1}{2}} \cdot \frac{\rho_{ma}}{\rho_e}\right]$$

Derivative with respect to average density

$$u2\_d\rho_{ma1} := \frac{\partial}{\partial \rho_{ma}}\left[\left[\frac{VelE_{PBC4}(VP\_2 \cdot C_{Ecorr})^2 - \left(k_2 \cdot VelE_{PBC3}(VP\_1 \cdot C_{Ecorr})\right)^2}{1 - k_1{}^2 \cdot k_2{}^2}\right]^{\frac{1}{2}} \cdot \frac{\rho_{ma}}{\rho_e}\right]$$

Derivative with respect to one sample density

$$u2\_d\rho_{e1} := \frac{\partial}{\partial \rho_{e}}\left[\left[\frac{VelE_{PBC4}(VP\_2 \cdot C_{Ecorr})^2 - \left(k_2 \cdot VelE_{PBC3}(VP\_1 \cdot C_{Ecorr})\right)^2}{1 - k_1{}^2 \cdot k_2{}^2}\right]^{\frac{1}{2}} \cdot \frac{\rho_{ma}}{\rho_e}\right]$$

$$u2\_dVel_{BFC1} := \frac{\partial}{\partial Vel_{BFC1}}\left[\left[\left[\frac{Vel_{BFC2}{}^2 - \left(k_2 \cdot Vel_{BFC1}\right)^2}{1 - k_1{}^2 \cdot k_2{}^2}\right]^{\frac{1}{2}} \cdot \frac{\rho_{ma}}{\rho_e}\right] \cdot \frac{s}{m}\right]$$

Derivative with respect to Calibration Velocity from wire 2

$$u2\_dVel_{BFC2} := \frac{\partial}{\partial Vel_{BFC2}}\left[\left[\frac{Vel_{BFC2}{}^2 - \left(k_2 \cdot Vel_{BFC1}\right)^2}{1 - k_1{}^2 \cdot k_2{}^2}\right]^{\frac{1}{2}} \cdot \frac{\rho_{ma}}{\rho_e}\right] \cdot \frac{s}{m}$$

Uncertainty for Tangential Direction Velocity

$$B\_u_2 := \left[\left(u2\_dC_{Ecorr1} \cdot B\_C_{Ecorr}\right)^2 + \left(u2\_d\rho_{ma1} \cdot B\_\rho_{ma}\right)^2 + \left(u2\_d\rho_{e1} \cdot B\_\rho_{ma}\right)^2 \ldots + \left(u2\_dVel_{BFC1} \cdot B\_Vel_{BFC1}\right)^2 + \left(u2\_dVel_{BFC2} \cdot B\_Vel_{BFC2}\right)^2\right]^{\frac{1}{2}} = 0.188$$

$$t\_S\_u_2 := \left[\left(u2\_dC_{Ecorr1} \cdot t\_S\_C_{Ecorr}\right)^2 + \left(u2\_d\rho_{ma1} \cdot B\_\rho_{ma}\right)^2 + \left(u2\_d\rho_{e1} \cdot B\_\rho_{ma}\right)^2 \ldots + \left(u2\_dVel_{BFC2} \cdot t\_S\_Vel_{BFC2}\right)^2 + \left(u2\_dVel_{BFC2} \cdot t\_S\_Vel_{BFC2}\right)^2\right]^{\frac{1}{2}} = 0.063$$

$$U\_u_2 := \left(B\_u_2{}^2 + t\_S\_u_2{}^2\right)^{\frac{1}{2}} \cdot \frac{m}{s} = 0.199\frac{m}{s}$$

$$\frac{U\_u_2}{u_2} = 2.533\%$$

Furthermore, as predicted from the DANTEC guide the majority of the uncertainty comes from the contribution of the calibration and linearization.

$\frac{U\_lin\_cal\_1}{U\_u_1} = 60.814\%$ Wire 1

$\frac{U\_lin\_cal\_2}{U\_u_2} = 90.132\%$ Wire 2

Data Reduction

With the uncertainties of both wires from the probe known, the flow quantities are determined.

$V_{vec} := \sqrt{u_1^{\,2} + u_2^{\,2}} = 10.107\frac{m}{s}$ where V_{vec} is the velocity vector

and the uncertainty is given by

$$U\_V_{vec} := \left[\left[\frac{\partial}{\partial u_1}\left(\sqrt{u_1^{\,2} + u_2^{\,2}}\right)\right]^2 \cdot U\_u_1^{\,2} + \left[\frac{\partial}{\partial u_2}\left(\sqrt{u_1^{\,2} + u_2^{\,2}}\right)\right]^2 \cdot U\_u_2^{\,2}\right]^{\frac{1}{2}} = 0.162\frac{m}{s}$$

$\frac{U\_V_{vec}}{V_{vec}} = 1.605\%$ Then the velocities measured have a percentage uncertainty of 1.605%

Below are the intermediate u and w velocities that still need angle correction to account for the difference in orientation from the calibration to the experiment set-up.

$u_{int} := \frac{u_1 + u_2}{\sqrt{2}} = 10.054\frac{m}{s}$ $w_{int} := \frac{u_1 - u_2}{\sqrt{2}} = -1.033\frac{m}{s}$

$$\beta_{exp} := \operatorname{asin}\left(\frac{w_{int}}{\sqrt{u_{int}^{\,2} + w_{int}^{\,2}}}\right) = -5.865\,deg$$

The angle correction is executed by finding a value for the "true" w velocity that is close to zero

$\beta_{cor} := \beta_{exp} + 5.9deg = 0.035\,deg$

$w := V_{vec}\cdot\sin(\beta_{cor}) = 6.196\times 10^{-3}\frac{m}{s}$ $u := V_{vec}\cdot\cos(\beta_{cor}) = 10.107\frac{m}{s}$

$$U\_w := \frac{d}{dV_{vec}}\left[\left(V_{vec}\cdot\sin\left(\beta_{cor}\right)\right)\cdot U\_V_{vec}\right] = 9.945\times 10^{-5}\,\frac{m}{s}$$

$$\frac{U\_w}{w} = 1.605\cdot\%$$

$$U\_u := \frac{d}{dV_{vec}}\left[\left(V_{vec}\cdot\cos\left(\beta_{cor}\right)\right)\cdot U\_V_{vec}\right] = 0.162\frac{m}{s}$$

$$\frac{U\_u}{u} = 1.605\cdot\%$$

The uncertainty for the angle correction from calibration to experiment is given below.

$$U\_\beta_{exp} := \left[\left[\frac{d}{du_{int}}\left(\operatorname{asin}\left(\frac{w_{int}}{\sqrt{u_{int}^{2}+w_{int}^{2}}}\right)\right)\right]^{2}\cdot U\_V_{vec}^{2}\ \ldots\right.$$
$$\left.+\left[\frac{d}{dw_{int}}\left(\operatorname{asin}\left(\frac{w_{int}}{\sqrt{u_{int}^{2}+w_{int}^{2}}}\right)\right)\right]^{2}\cdot U\_V_{vec}^{2}\right]^{\frac{1}{2}} = 0.92\cdot deg$$

The result falls within the predicted value of $\underline{+}1°$ from provided by the DANTEC guide, although it is noted that it has almost negligible bearing on the total uncertainty of the velocity measurements.

REFERENCES

[1] Zhang, H.J., Zhou, Y., and Cheng, L., 2006, "Control of Flow Separation from an Airfoil Using Piezo-Ceramic Actuators," *3rd AIAA Flow Control Conference*, AIAA 2006-3689, pp. 1-7.

[2] Gilarranz, J.L., Traub, L.W., and Rendiniotis, O.K., 2005, "A New Class of Synthetic Jet Actuators – Part II: Application to Flow Separation Control," ASME Journal of Fluids Engineering, **127**, pp. 377-387.

[3] Long, J., and ZeLiang, Y., 2006, "Experimental Study on Heat Transfer Enhancement on Natural Convection in a Vertical Plate by Using Longitudinal Vortex Generators Arranged in Rows," Heat Transfer – Asian Research, **35** (5), pp.351-358.

[4] Tanaka, T., Itoh, M., Hatada, T., and Matsushima, H., 2003, "Influence of Inclination Angle, Attack Angle, and Arrangement of Rectangular Vortex Generators on Heat Transfer Performance," Heat Transfer – Asian Research, **32** (3), pp. 253-267.

[5] Satta, F., Simoni, D., Ubaldi, M., Zunino, P., Bertini, F., and Spano, E., 2007, "Velocity and Turbulence Measurements in a Separating Boundary Layer With and Without Passive Flow Control," Journal of Power and Energy: Proceedings from IMechE, **221**, pp. 815-823.

[6] Angele, K.P., and Grewe, F., 2007, "Instantaneous Behavior of Streamwise Vortices for Turbulent Boundary Layer Separation Control," ASME: Journal of Fluids Engineering, **129**, pp. 226-235.

[7] Brandt, S.A., Stiles, R.J., Bertin, J.J., and Whitford, R., 2004, *Introduction to Aeronautics: A Design Perspective*, 2nd ed., American Institute of Aeronautics and Astronautics, Inc., Reston, VA.

[8] Aviation Partners Boeing, 2006, "http://www.aviationpartnersboeing.com" November 10, 2009.

[9] Lofdahl, L., and Gad-el-Hak, M., 1999, "MEMS application in turbulence and flow control," Progress in Aerospace Sciences, **35**, pg 101-203.

[10] Saric, W.S., 2001, "Control of Transition in Swept-Wing Boundary Layers using MEMS Devices as Distributed Roughness," XAA0034F, Arizona State University, Tempe, AZ.

[11] Velte, C.M., 2007, "Experimental and Numerical Investigation of the Performance of Vortex Generators on Separation Control, Journal of Physics: Conference Series, **75** , pp.1-11.

[12] Qiao, W., Yi, J., Zhang, M., Luo, H., and Xu, K., 2006, "Secondary Flow Control on Blades of Turbine Using Fluid Injection," *42nd AIAA/ASME/SAE/ASEE Joint Conference & Exhibit,* AIAA 2006-4452, pp. 1-9.

[13] Santhanakrishnan A., and Jacob, J.D., 2007, "Flow Control with Plasma Synthetic Jet Actuators," Journal of Physics D: Applied Physics, **40**, pp. 637-651.

[14] Tarsitano, S. F., Russell, A. P., Horne, F., Plummer, C., and Millerchip, K., 2000, "On the Evolution of Feathers from and Aerodynamic and Constructional View Point. American Zoology, **40**:676-686.

[15] Ho, S., Nassef, H., Pornsinsirirak, N., Tai, Y., and Ho, C., 2003, "Unsteady Aerodynamics and Flow Control for Flapping Wing Flyers," Progress in Aerospace Sciences, 39, pp. 635-681.

[16] Carruthers, A.C., Thomas, A.L.R., and Taylor, G.K., 2007, "Automatic aeroelastic devices in the wings of a steppe eagle *Aquila nipalensis*," The Journal of Experimental Biology, **210**, pp. 4136-4149.

[17] Çengel, Y.A., and Cimbala, J.M., *Fluid Mechanics: Fundamentals and Applications*, 1st ed., McGraw-Hill, New York, NY.,

[18] Roskam, J., and Lan, C.E., 1997, *Airplane Aerodynamics and Performance, Design, Analysis and Research Corporation,* Lawrence, KS.

[19] Whitford, R., 1989, *Design for Air Combat*, Jane's Information Group Limited, Surrey, JK

[20] Bertin, J.J., and Cummings, R.M., 2009, *Aerodynamics for Engineers,* 5th ed. Pearson Prentice Hall, Upper Saddle River, NJ.

[21] Wallis, R., 1952, "The use of air jets for boundary layer control," Aero Note 110, Aerodynamics Research Laboratories, Australia.

[22] Stanewsky, E., 2001, "Adaptive wing and flow control technology," Progress in Aerospace Sciences, **37**, pp. 583-667.

[23] Carpenter, A., William, S.S., and Reed, H.L., 2008, "Laminar Flow Control on a Swept Wing with Distributed Roughness," *26th AIAA Applied Aerodynamics Conference*, pp. 1-9.

[24] Lin, J.C., Howard, F.G., and Selby, G.V., 1990, “Small Submerged Vortex Generators for Turbulent Flow Separation Control,” AIAA Journal of Spacecraft, **27,** pp. 503-507.

[25] Selby, G.V., Lin, J.C., and Howard, F.G., 1990, “Jet Vortex Generators for Turbulent Flow Separation Control,” *12th Symposium on Turbulence*

[26] Margalit, S., Greenblatt, D., Seifert, A., and Wygnanski, I., 2005, “Delta Wing Stall and Roll Control Using Segmented Piezoelectric Fluidic Actuators,” Journal of Aircraft, **42**, pp. 698-709.

[27] Gregory, J. W., Sullivan, J. P., Raman, G., and Raghu, S., 2007, “Characterization of the Microfluidic Oscillator,” *AIAA Journal*, **45**, pp. 568-576.

[28] Lee, G.-B., Shih, C. Tai, Y.-C., Tsao, T., Liu, C., Huang, A., and Ho, C.-M. 2000, “Robust Vortex Control of a Delta Wing by Distributed Microelectromechanical-System Actuators,” *Journal of Aircraft*, **37**, pp. 697-706.

[29] Lockerby, D. A. and Carpenter, P. W., 2004, “Modeling and Design of Microjet Actuators,” *AIAA Journal*, **42** (2), pp. 220-227.

[30] Renac, F., Barberis, D., and Molton, P., 2005, “Control of Vortical Flow over a Rounded Leading-Edge Delta Wing,” *AIAA Journal*, **43**, pp. 1409-1418.

[31] Lockerby, D. A., Carpenter, P. W., and Davies, C., 2005, “Control of Sublayer Streaks using Microjet Actuators,” *AIAA Journal*, **43**, pp. 1878-1886.

[32] Fukuta, Y., Chapuis, Y.A., Mita, Y., and Fujita, H., 2006, “Design, Fabrication, and Control of MEMS-Based Actuator Arrays for Air-Flow Distributed Micromanipulation.” *Journal of Microelectromechanical Systems*, **15** (4), pp 912-926.

[33] Tung, S., Maines, B. Jiang, F., and Tsao, T., 2004, “Development of a MEMS-Based Control System for Compressible Flow Separation,” IEEE Journal of Microelectromechanical Systems, **13**, pp. 91-99.

[34] Jørgensen, F.E., 2002, “How to Measure Turbulence with Hot-Wire Anemometers,” No. 9040U6151, Dantec Dynamics A/S, Skovlunde, Denmark.

[35] Homan, J.P., 2001, *Experimental Methods for Engineers,* 7th ed., McGraw-Hill, New York, NY.

[36] Moffat, R.J., 1988, “Describing the Uncertainties in Experimental Results,” Experimental Thermal and Fluid Science, **1**, pp. 3-17.

[37] ANSYS FLUENT 12.0 Documentation.